# Experimental studies on the deep geochemistry of carbon and nitrogen

**Dissertation**

zur Erlangung der Würde eines
Doktors der Naturwissenschaften
- Dr. rer. nat. -

der Bayreuther Graduiertenschule für Mathematik und Naturwissenschaften

vorgelegt von

**Takahiro Yoshioka**

aus Niigata, Japan

Bayreuth, 2018

This doctoral thesis was prepared at Bayerisches Geoinstitut at the University of Bayreuth from April 2018 until August 2018 and was supervised by Prof. Dr. Hans Keppler.

This is a full reprint of the dissertation submitted to obtain the academic degree of Doctor of Natural Sciences (Dr. rer. nat.) and approved by the Bayreuth Graduate School of Mathematical and Natural Sciences (BayNAT) of the University of Bayreuth.

Date of submission: 16.08.2018
Date of defence: 07.11.2018

Acting director: Prof. Dr. Dirk Schüler

Doctoral committee:
Prof. Dr. Hans Keppler (reviewer)
PD. Dr. Catherine McCammon (reviewer)
Prof. Dr. Daniel J. Frost (chairman)
Prof. Dr. Tomoo Katsura

## *Table of contents*

# Abstract

Volatiles play an important role in Earth´s interior, as they affect the physical properties of the mantle, melting, and volcanic activity. They also control Earth's surface environment, which is essential for the evolution of live. Among the major volatile elements, carbon and nitrogen are less studied as compared to hydrogen or water. For carbon, the behavior under reducing conditions is much less studied than that at high oxygen fugacity, where $CO_2$ or carbonates are stable. In particular, the carbon solubility in silicate melts under reducing and vapor-saturated conditions has not yet been investigated. For nitrogen, the bulk nitrogen abundance and the size of various reservoirs in the deep Earth are still controversial. The nitrogen storage capacity of the transition zone and of the lower mantle is completely unknown. Accordingly, the purpose of this thesis is to fill some major gaps in the understanding of the deep geochemistry of carbon and nitrogen.

In order to investigate the speciation of reduced carbon in silicate melts, a series of high-pressure and high-temperature experiments was carried out at 1 GPa and 1450-1530 °C under graphite-saturated conditions with MORB glasses as starting materials. Raman and infrared spectra of quenched glass samples showed bands at 2100-2200 $cm^{-1}$ region, which had been assigned to iron pentacarbonyl $Fe(CO)_5$ in some previous studies. However, in the present study, these bands were observed in both Fe-bearing and Fe-free samples. Together with results from Mössbauer spectroscopy, these observations rule out any assignment of the bands to Fe-bearing species. Extensive studies in the chemical literature on the absorption of CO on surfaces also demonstrate that the vibrational frequency and the infrared extinction coefficients of the CO molecule shift due to interaction with the matrix. Therefore, the bands in the 2100-2200 $cm^{-1}$ region of the Raman and infrared spectra of glasses are likely due to CO molecules weakly interacting with the glass matrix. Quantification of CO by infrared spectroscopy may require extinction coefficients specific to the composition of glasses.

In order to better understand the behavior of reduced carbon in a magma ocean or during volcanic activity on the Moon, the solubility of carbon in silicate melts coexisting with both graphite and a CO-$CO_2$ gas phase was investigated. A series of high-pressure and

high-temperature experiments was conducted at 1200-1600 °C with an internally heated pressure vessel (0.2 – 0.5 GPa) and a piston-cylinder apparatus (1 – 3 GPa). $CO_2$ (as $Ag_2C_2O_4$) + graphite or CO gas were loaded into sample capsules together with Fe-free MORB, andesite and rhyolite starting glasses. During the experiments, the composition of the gas was controlled by the equilibrium 2 CO = $CO_2$ + C (CCO-buffer). The bulk carbon solubility in the quenched glasses quantified by secondary ion mass spectrometry (SIMS) increases with pressure for all melt compositions, approximately following Henry's law. The effect of temperature is rather minor compared to the effect of pressure. The Henry's coefficients obtained are 2.15 ppm C/MPa for MORB, 1.57 C/MPa for andesite and 2.14 C/MPa for rhyolite, comparable to pure $CO_2$ solubility. Almost all the samples contain more bulk carbon than oxidized carbon ($CO_2$ and carbonate) as quantified from the infrared spectra. The difference is interpreted to be due to dissolved CO, which was also observed in the infrared and Raman spectra of some samples as bands in the 2100–2200 $cm^{-1}$ region. The fraction of CO dissolved in the glasses is about 10-20 % of total C in MORB and rhyolite and 5 % in andesite. CO solubility can be expressed by the equations $\log c_{CO}^{MORB} = -5.83 + 0.98 \log f_{CO}$ ($R^2 = 0.84$) for MORB and $\log c_{CO}^{Rhyolite} = -4.52 + 0.65 \log f_{CO}$ ($R^2 = 0.74$) for rhyolite, where $c_{CO}$ is solubility of carbon dissolved as CO in wt. % and $f_{CO}$ is CO fugacity. The solubility of carbon is strongly depend on whether or not the gas phase is in equilibrium with graphite – when the equilibrium 2 CO = $CO_2$ + C is not attained and CO is a dominant carbon species, the solubility of carbon is very low. CO could also be a main component of the gas phase at low pressure (< a few 100 MPa) under graphite saturation. According to the equation of CO solubility in MORB melts shown above and the estimated carbon concentration in magmas of lunar fire-fountain eruptions, CO may have reached vapor saturation at 31 MPa, which is equivalent to 7.4 km depth in the Moon.. Moreover, at the magma ocean stage of the early Earth, it is likely that the oxygen fugacity was initially much lower than the IW-buffer. In such a situation, CO would have been a dominant carbon component in the atmosphere and may have produced a carbon-poor magma ocean. This could be a plausible mechanism for limiting carbon partitioning into the core and retaining a significant fraction of carbon near the Earth's surface. Another interesting observation is that the CO-related bands appear to have a very low infrared extinction coefficient (966 $cm^{-1}$ in rhyolite). This fact suggests that traces of CO may be easily overlooked in by spectroscopic methods.

To provide constraints on nitrogen partitioning into the deep mantle, the nitrogen solubility in transition zone and lower mantle minerals (ringwoodite, wadsleyite, bridgmanite and Ca-silicate perovskite) was studied. Experiments were conducted with a multi-anvil apparatus at 14-24 GPa and 1100-1800 °C. Minerals were synthesized coexisting with a $^{15}$N-doped nitrogen-rich fluid at Fe-FeO buffer conditions. Nitrogen concentrations were quantified by SIMS and microprobe analysis (for metal only). The observed nitrogen ($^{15}$N) solubility in wadsleyite and ringwoodite was typically in the range of 10-250 ppm by weight. High temperature strongly enhances nitrogen solubility, while pressure has a moderate effect. Nitrogen solubility in bridgmanite and Ca-silicate perovskite was about 20 and 30 ppm, respectively, which is lower than the nitrogen solubility in transition zone minerals. Nitrogen solubility in metal coexisting with the minerals increases with pressure and decreases with temperature, with a maximum solubility of almost 1 wt. %. These results, together with data for upper mantle minerals from a previous study show that the nitrogen ($^{14}$N) storage capacity of the upper mantle, transition zone and lower mantle is 20, 8.0, and 25 times the mass of present atmospheric nitrogen (PAN), respectively.

Together with data on nitrogen solubility in silicate melts from the literature, nitrogen partitioning between the mantle and the atmosphere during magma ocean crystallization was modeled. Upon modeling, it was assumed that the mantle convects and reaches equilibrium with the atmosphere until 50% of the mantle crystalizes. After this point, the mantle does not convect anymore and retains dissolved nitrogen until it reaches saturation in the mantle minerals. The initial nitrogen partial pressure of the atmosphere was estimated by assuming that Earth's main nitrogen source are enstatite-chondrites and that nitrogen was depleted by impact degasing to a similar extend as the other volatiles during accretion of the Earth, yielding a nitrogen partial pressure of 1.0-3.5 MPa. The model suggests that this partial pressure leads to 3.1–10.9 PAN being stored in the mantle after magma ocean solidification. This result implies that most of the nitrogen on Earth still resides in a deep reservoir. The high $N_2/^{40}$Ar mantle sources observed in some OIB samples and xenoliths may represent such a deep nitrogen reservoir. Therefore, dynamic exchange of nitrogen between the deep nitrogen reservoir and surface may have caused changes in bulk atmospheric pressure over geologic time.

# Zusammenfassung

Flüchtige Bestandteile spielen im Erdinneren eine wichtige Rolle, da sie die physikalischen Eigenschaften des Mantels, Schmelzbildung und vulkanischer Aktivität beeinflussen. Darüber hinaus kontrollieren sie die Bedingungen auf der Erdoberfläche, die essentiell sind für die Entwicklung des Lebens. Unter den am häufigsten vorkommenden flüchtigen Bestandteilen wurden Kohlenstoff und Stickstoff weniger untersucht als Wasserstoff oder Wasser. Das Verhalten von Kohlenstoff im Erdinnern ist unter reduzierten Bedingungen sehr viel weniger gut bekannt als bei hohen Sauerstofffugazitäten, im Stabilitätsbereich von $CO_2$ oder Karbonat. Insbesondere die Löslichkeit von Kohlenstoff in silikatischen Schmelzen unter reduzierten Bedingungen im Gleichgewicht mit einer Gasphase wurde bislang nicht untersucht. Die Menge an Stickstoff, die im Erdinnern gespeichert ist, sowie die mögliche Speicherkapazität von Reservoiren in der tiefen Erde sind noch immer umstritten. Die Speicherkapazität von Stickstoff in der Übergangszone und im tieferen Mantel sind gänzlich unbekannt. Es ist daher das Ziel dieser Arbeit, die genannten Lücken im Verständnis der tiefen Geochemie von Kohlenstoff und Stickstoff zu schließen.

Für die Untersuchung der Speziation von reduziertem Kohlenstoff in silikatischen Schmelzen wurde eine Reihe von Hochdruck- und Hochtemperaturexperimenten bei 1 GPa und 1450 - 1530 °C unter Graphit-gesättigten Bedingungen durchgeführt. Ausgangsmaterial war ein MORB-Glas. Raman- und Infrarotspektren von abgeschreckten Glasproben zeigen Banden bei 2100 - 2200 $cm^{-1}$, welche in früheren Studien Eisenpentacarbonyl $Fe(CO)_5$ zugeordnet wurden. Diese Banden konnten aber sowohl in eisenhaltigen als auch in eisenfreien Proben beobachtet werden. Zusammen mit Ergebnissen aus der Mössbauer-Spektroskopie kann die Zuordnung dieser Banden zu einer eisenhaltigen Spezies daher ausgeschlossen werden. Literaturdaten über die Absorption von CO an Oberflächen zeigen, dass die Schwingungsfrequenz und die Infrarot-Extinktionskoeffizienten von CO-Molekülen durch die Wechselwirkung mit der Matrix verändert werden. Daher sind die Banden in der 2100-2200 $cm^{-1}$-Region des Raman- und Infrarotspektrums der Glasproben wahrscheinlich auf CO-Moleküle zurückzuführen, die schwache chemische Wechselwirkungen mit der Glasmatrix

aufweisen. Die Quantifizierung von CO mithilfe von Infrarotspektroskopie ist wahrscheinlich nur mit Matrix-spezifische Extinktionskoeffizienten möglich.

Um das Verhalten von reduziertem Kohlenstoff in einem Magmaozean oder während der vulkanischen Aktivität auf dem Mond besser zu verstehen, wurde die Löslichkeit von Kohlenstoff in Silikatschmelzen im Gleichgewicht mit Graphit und einer CO-$CO_2$ Gasphase untersucht. Eine Reihe von Hochdruck- und Hochtemperaturexperimenten wurden zwischen 1200 - 1600°C mit einem innenbeheizten Autoklaven (0.2 - 0.5 GPa) und einer Kolbenzylinderpresse (1 - 3 GPa) durchgeführt. Ausgangsmaterial für die Experimente waren synthetische, Fe-freie Gläser (MORB, Andesit oder Rhyolith). Die Probenkapseln wurden mit $CO_2$ (als $Ag_2C_2O_4$) und Graphit oder mit CO-Gas gefüllt. Während des Experiments wurde die Zusammensetzung des Gases durch das Gleichgewicht 2 CO = $CO_2$ + C (CCO-Puffer) kontrolliert. Die Kohlenstofflöslichkeit in den Schmelzen, welche mit Hilfe der Sekundärionen-Massenspektrometrie (SIMS) untersucht wurde, folgt dem Henry´schen Gesetz, d.h. die Löslichkeit ist in guter Näherung proportional zum Druck.. Der Einfluss der Temperatur ist im Vergleich zum Druck gering. Die gemessenen Henry-Koeffizienten sind 2.15 ppm C/MPa für MORB, 1.57 C/MPa für Andesit und 2.14 C/MPa für Rhyolith. Nahezu alle Proben enthalten mehr Kohlenstoff als gemäß den Infrarotspektren in oxidierter Form (als $CO_2$ und Karbonat) vorliegt. Die Differenz wird als gelöstes CO interpretiert, welches auch in den Infrarot- und Ramanspektren einiger Proben als Banden in der 2100-2200 $cm^{-1}$-Region beobachtet wurde. Der Anteil von gelöstem CO in den Gläsern ist etwa 10-20 % des gesamten Kohlenstoffs in MORB und Rhyolit, sowie 5% in Andesit. Die CO-Löslichkeit kann durch die Gleichung log $c_{CO}^{MORB}$ = - 5.83 + 0.98 log $f_{CO}$ ($R^2$ = 0.84) für MORB und log $c_{CO}^{Rhyolith}$ = - 4.52 + 0.65 log $f_{CO}$ ($R^2$ = 0.74) für Rhyolith beschrieben werden, wobei $c_{CO}$ die Löslichkeit von CO als Gew. % Kohlenstoff und $f_{CO}$ die CO-Fugazität ist. Die Löslichkeit von Kohlenstoff ist stark abhängig davon, ob die Gasphase mit Graphit im Gleichgewicht ist - wenn das Gleichgewicht 2 CO = $CO_2$ + C nicht erreicht wurde und CO die dominante Gas-Spezies ist, ist die Löslichkeit von Kohlenstoff sehr gering. CO ist auch bei Graphitsättigung die Hauptkomponente der Gasphase, sofern der Druck sehr gering ist (< einige wenige 100 MPa). Gemäß der Gleichung für CO-Löslichkeit in MORB-Schmelzen (siehe oben) und den geschätzten Kohlenstoffkonzentrationen in Magmen der Feuer-Fontänen-Eruptionen auf dem Mond, könnte Kohlenstoff bei 31 MPa Gassättigung erreicht haben. Dies entspricht einer Tiefe

von 7.4 km unterhalb der Mondoberfläche. Während der Magmaozean-Phase der frühen Erde war die Sauerstofffugazität wahrscheinlich weit unterhalb des IW-Puffers. In diesem Fall wäre CO die dominante Kohlenstoffkomponente in der Atmosphäre und würde einen kohlenstoffarmen Magmaozean produzieren. Dies könnte ein plausibler Mechanismus für eine begrenzte Aufnahme von Kohlenstoff im Kern sein und einen signifikanten Anteil von Kohlenstoff an der Erdoberfläche halten. Eine weitere interessante Beobachtung ist, dass die CO-Banden im Infrarotspektrum von Gläsern einen sehr niedrigen Extinktionskoeffizienten (966 $cm^{-1}$ in Rhyolith) besitzen. Diese bedeutet, dass Spuren von CO in Infrarotspektren leicht übersehen werden könnten.

Um die Stickstoffverteilung im tiefen Mantel besser zu verstehen, wurde die Stickstofflöslichkeit in Mineralen der Übergangszone und des unteren Mantels (Ringwoodit, Wadsleyit, Bridgmanit und Ca-Silikat-Perovskit) untersucht. Die Experimente wurden mit einer Multianvil-Presse zwischen 14 - 24 GPa und 1100 - 1800 °C durchgeführt. Die Minerale wurden in Anwesenheit einer $^{15}N$-dotierten stickstoffreichen Fluidphase und unter der Sauerstofffugazität des Fe-FeO Puffers synthetisiert. Stickstoffkonzentrationen wurden mit Hilfe von SIMS und Mikrosondenanalysen (nur für Metalle) bestimmt. Die beobachtete Stickstofflöslichkeit ($^{15}N$) in Wadsleyit und Ringwoodit lag zwischen 10-250 ppm. Hohe Temperaturen erhöhen die Stickstofflöslichkeit stark, während Druck einen eher moderaten Effekt hat. Die Stickstofflöslichkeit in Bridgmanit und Ca-Silikat-Perovskit liegt bei 20 und 30 ppm, erheblich weniger als für die Minerale der Übergangszone. Die Löslichkeit von Stickstoff in Fe-Metall im Gleichgewicht mit den oben genannten Mineralen steigt durch Druck an, bis zu einer maximalen Löslichkeit von 1 Gew. %, und sinkt mit der Temperatur. Diese Ergebnisse zeigen (zusammen mit Daten für die Minerale des oberen Mantels aus einer früheren Studie), dass die Stickstoff-Speicherkapazität ($^{14}N$) des oberen Mantels, der Übergangszone und des unteren Mantels das 20 fache, 8-fache, bzw. 25-fache der heutigen Menge von Stickstoff in der Atmosphäre (PAN) ist.
Mit Hilfe von Literaturdaten über die Stickstofflöslichkeit in silikatischen Schmelzen wurde die Verteilung von Stickstoff zwischen dem Mantel und der Atmosphäre während der Kristallisationsphase des Magmenozeans modelliert. Im Modell wird angenommen, dass der Mantel konvektiert und im Gleichgewicht mit der Atmosphäre ist, bis 50% des Mantels kristallisiert sind. Ab diesem Zeitpunkt konvektiert der Mantel nicht mehr und

hält gelösten Stickstoff zurück, bis die Mantelminerale gesättigt sind. Der initiale Stickstoffpartialdruck der Atmosphäre wurde auf einen Wert von 1.0-3.5 MPa geschätzt, mit der Annahme, dass Enstatit-Chondrite die Hauptquelle von Stickstoff sind und dass Stickstoff durch Impakt-Entgasung zu einem ähnlichen Grad wie andere flüchtige Komponenten verloren ging,. Das Modell zeigt, dass bei diesem Partialdruck nach der Erstarrung des Magmaozeans 3.1 bis 10.9 PAN im Mantel gespeichert wurden. Diese Ergebnisse bedeuten, dass der größte Anteil des Stickstoffs auf der Erde noch immer in einem tiefen Reservoir vorliegt. Die Regionen des Mantels mit hohem $N_2/^{40}Ar$, aus denen einigen OIB-Proben und Xenolithen stammen, sind wahrscheinlich dieses tiefe Stickstoffreservoir. Ein dynamischer Austausch von Stickstoff zwischen dem tiefen Stickstoffreservoir und der Oberfläche hat möglicherweise Änderungen im Atmosphärendruck über geologische Zeiträume verursacht.

# 1. Introduction

## 1.1 Carbon and nitrogen in the deep Earth

Volatiles are chemical elements or compounds with low boiling points. The major volatile elements in the Earth are H, C, N, S, and Cl (major volatiles) together with minor amounts of the noble gases He, Ne, Ar, Kr and Xe (Rollinson, 2007). Together with oxygen, volatile elements form the atmosphere and oceans. Volatiles play important roles in the Earth system. They may significantly affect the physical properties of the mantle and play an important role in the generation of magmas. Some experimental studies suggested that water greatly reduces the viscosity of olivine and thereby affects mantle convection (e.g. Karato et al., 1986, Mei and Kohlstedt, 2000), while more recent investigations suggest that this effect is rather minor (Fei at al., 2013). In magmatic systems, water and $CO_2$ may lower solidus temperatures by several 100 °C (Yoder, 1976); the degassing of these volatiles drives explosive eruptions of volcanoes. The degassing of volatiles from Earth´s interior was also essential for the evolution of life on Earth. The abiotic synthesis of amino acids is possible in a highly reducing atmosphere (Miller and Urey, 1959) that may have been stabilized by the degassing of reduced volatiles.

The Earth was formed by accretion of smaller bodies (planetesimals) within a circumstellar disk (e.g. Rubie et al., 2015). The planetesimals which formed the Earth were likely of chondritic composition, representing primitive material of the solar nebula. Chondrites are the most abundant meteorites (87% of all meteorites), which are ultramafic in composition and contain olivine, pyroxene and metallic iron. They are classified into carbonaceous, ordinary and enstatite types (Rollinson, 2007). Carbonaceous chondrites are rich in carbon and other volatiles. Therefore, they are considered to be the most primitive material, as they have never experienced any heating event that would have led to volatile loss. They are also subdivided into several types (CI, CM, CV, etc.). Ordinary chondrites are the most abundant chondrite type. Enstatite chondrites are highly reduced and contain more enstatite than olivine. The isotopic composition of H and N in chondrites is similar to the bulk Earth, suggesting that they are the main source of volatiles, while comets may have made at most a minor contribution

to Earth´s volatile budget (Fig. 1.1). This implies that most volatiles on the surface of the Earth must have degassed from Earth´s interior at some time.

Among the major volatiles, hydrogen (mainly in the form of water or OH in minerals) is relatively well studied (e.g. reviews by Bell and Rossman, 1992, Thompson, 1992). There is also direct evidence for water in the transition zone of the mantle from a sample of hydrous ringwoodite found as inclusion in a diamond (Pearson et al., 2014). Seismic observations have also been used to infer mantle water contents (e.g. Meijde et al., 2003, Kawakatsu and Watada, 2007). Compared with hydrogen or water, the behavior of carbon and in particular, of nitrogen is less studied. Therefore, this thesis focuses on these two elements to provide experimental constraints on their behavior during the evolution of the Earth.

Carbon and nitrogen in the universe are formed by nucleosynthesis in stars (McSween and Huss, 2010). Carbon ($^{12}C$) is produced from three $^{4}He$ nuclei ( $\alpha$ particles), through a process known as triple alpha reaction. After $^{12}C$ is formed, $^{16}O$ can be also produced by

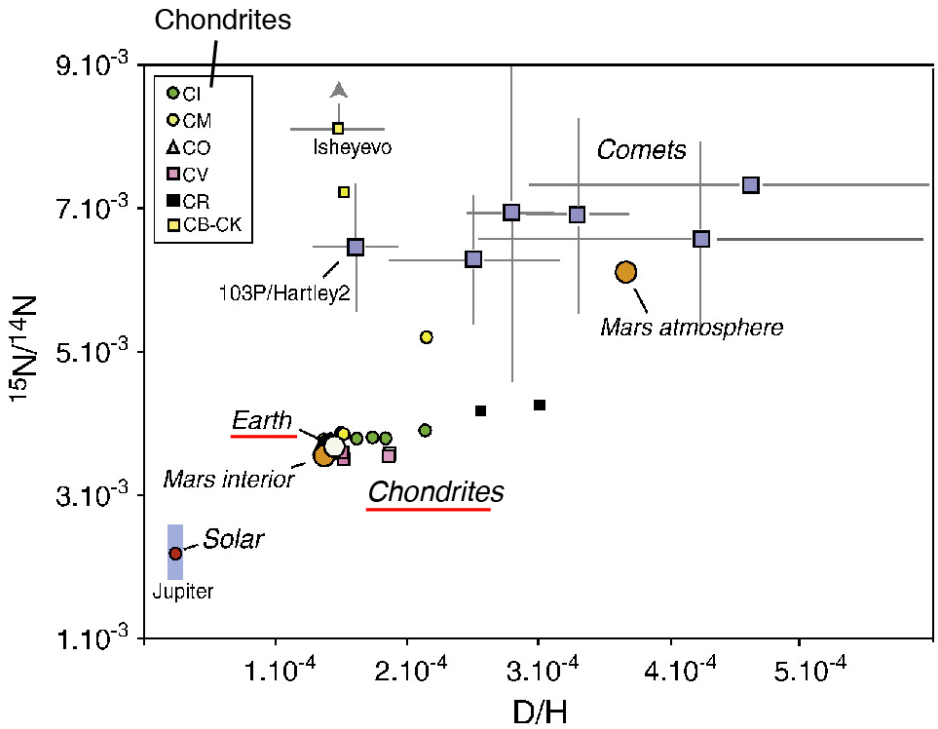


*Fig. 1.1. Variations of D/H ($^{2}H/^{1}H$) and $^{15}N/^{14}N$ ratios among solar system reservoirs, chondrites and comets. (Modified from Marty, 2012). Earth and chondrites have similar isotopic compositions.*

adding one $^{4}He$. However, the reaction forming $^{16}O$ is much slower than the triple-alpha process, resulting in a star core richer in $^{12}C$.

The key process for producing nitrogen is the so-called CNO cycle (McSween and Huss, 2010). The CNO cycle is a process of producing $^{4}He$ from four $^{1}H$ involving carbon as a nuclear catalyst at high temperature. The cycle includes several different loops of reactions. The most important pathway follows these reactions:

$$^{12}C + {}^{1}H \rightarrow {}^{13}N + \gamma$$

$$^{13}N \rightarrow {}^{13}C + \beta^{+} + \nu$$

$$^{13}C + {}^{1}H \rightarrow {}^{14}N + \gamma$$

$$^{14}N + {}^{1}H \rightarrow {}^{15}O + \nu$$

$$^{15}O \rightarrow {}^{15}N + \beta^{+} + \nu$$

$$^{15}N + {}^{1}H \rightarrow {}^{12}C + {}^{4}He$$

$\beta^{+}$ is a positron, a particle which has a positive electric charge of 1e and same mass as an electron, $\nu$ is a neutrino. As the reaction of $^{14}N$ with $^{1}H$ is the slowest in the process by a factor of more than ten, much of the $^{15}N$, $^{12}C$ and $^{13}C$ is converted into $^{14}N$.

As noted above, Earth was likely formed by accretion of chondritic material. The bulk refractory element composition of the Earth is, therefore, usually in good agreement with chondritic composition. On the other hand, the bulk volatile element composition of the Earth cannot be estimated directly from the chondritic composition because a significant amount of volatiles was lost during accretion (Rollinson, 2007). However, the initial abundance of such light elements provides important constraints on the processes involved in Earth's evolution.

According to data compiled by Johnson and Goldblatt (2015), the carbon abundance in carbonaceous chondrites (CC) and enstatite chondrites (EC) are $2.68 \pm 2.64 \times 10^{4}$ ppm and $4500 \pm 480$ ppm, respectively. Although the carbon contents in carbonaceous chondrites show considerable scatter, the carbon contents in the CI- and CM-types, which are the most primitive carbonaceous chondrites, are in a more narrow range of $2.40 \pm 0.24 \times 10^{4}$ ppm carbon. The carbon abundance in the bulk silicate Earth (BSE) was estimated by Marty (2012). The carbon content estimated from the $C/^{40}Ar$ ratio of mantle samples is $1164 \pm 544$ ppm. The abundance of $^{40}Ar$ was calculated from the $^{4}He/^{40}Ar$ ratio

because $^{40}Ar$ data are sometimes not available. From this estimation, the total mass of carbon in BSE is expected to be $4.9 \pm 2.3 \times 10^{21}$ kg. Marty (2012) also estimated the carbon abundance in BSE from C/N ratios, yielding carbon concentration of 580 ± 380 ppm. However, the nitrogen abundance in BSE is largely uncertain depending on the method of calculation.

The nitrogen content compiled by Johnson and Goldblatt (2015) in CC and EC is 1235 ± 440 ppm and 605 ± 206 ppm, respectively. The nitrogen abundance in BSE is largely uncertain and therefore calculated using average abundance ratios of other volatile elements in BSE as compared to CC and EC. This calculation assumes that all volatiles are depleted in Earth relative to their abundance in chondrites by the same factor. The average ratios of volatile abundance in BSE relative to CC and EC are 2.75 ± 0.2 % and 9.2 ± 0.1 %, yielding a nitrogen abundance in BSE of 4.1 ± 3.1 ppm (from CC) and 7.3 ± 5.6 ppm (from EC). These values are equivalent to $1.7 \pm 1.3 \times 10^{19}$ kg and $3.1 \pm 2.4 \times 10^{19}$ kg in BSE, respectively. However, these nitrogen abundances in BSE may have been underestimated because the calculations consider that a significant fraction of nitrogen

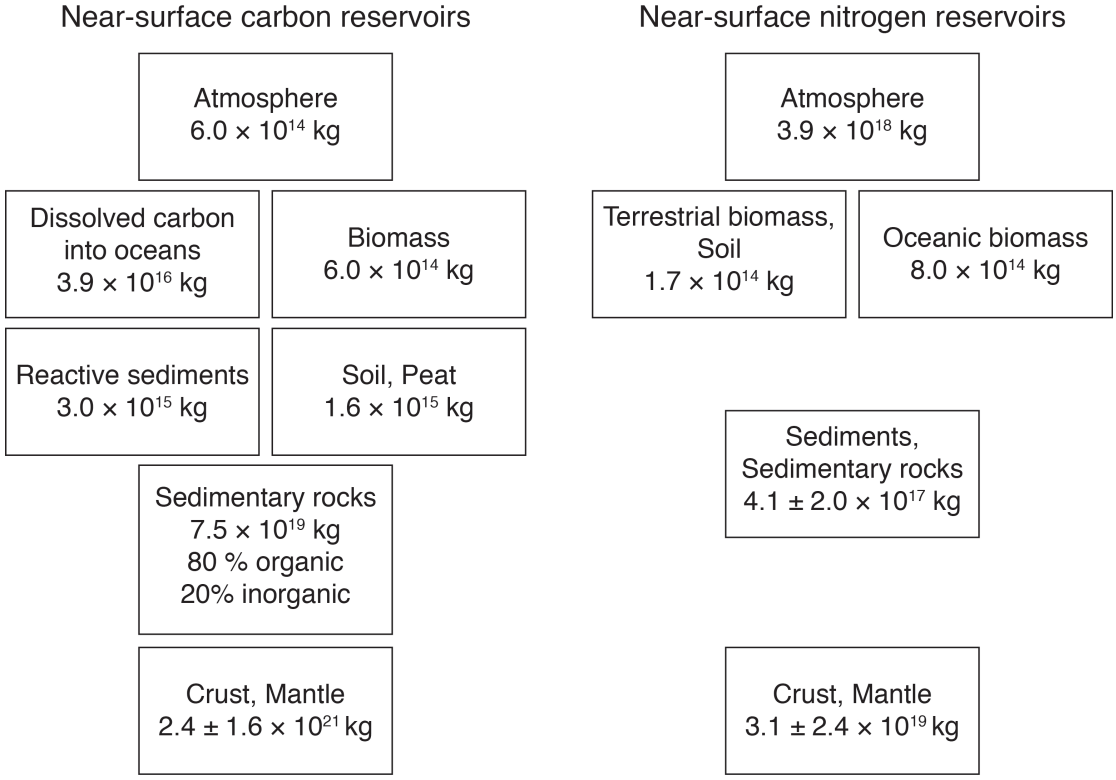


*Fig. 1.2. Schematic diagram showing the estimated budget of near-surface carbon and nitrogen reservoirs. Data are from Killops and Killops (2005), Ozima and Podosek (2002) and Johnson and Goldblatt (2015)*

partitioned into the core, while the actual degree of partitioning into the core could be much lower (see the discussion below). As the comparison of volatile abundances in the Earth and in chondrites shows, the present volatile abundance is one or two order of magnitude below that in primitive materials. This fact implies that most of the volatiles must have been lost, either during impact or during the accretion of planetesimals or in the magma ocean stage of the Earth.

The carbon and nitrogen reservoirs close to the Earth's surface are relatively well known. The largest carbon reservoir near Earth's surface (Killops and Killops, 2005) is in sedimentary rocks with $7.5 \times 10^{19}$ kg carbon, most of which is contained in carbonates (ca. 20 % of the carbon is organic). At the very shallow part of the sediment column, reactive sediments (carbonate which may be leached out from the upper layer of sediments) and soil/peat account for $3.0 \times 10^{15}$ and $1.6 \times 10^{15}$ kg carbon, respectively. The second largest reservoir are the oceans, which account for $3.9 \times 10^{16}$ kg carbon. The carbon contained in biomass is much less than these reservoirs and nearly $6.0 \times 10^{14}$ kg. Finally, the carbon present in the atmosphere mostly as carbon dioxide, amounts to $6.0 \times 10^{14}$ kg. Carbon from these surface reservoirs, mainly sedimentary carbonates, is transported into Earth's interior by subduction of oceanic crust. Studies on carbonate stability in subduction conditions showed that carbonate in altered oceanic crust survives and is transported into the deep mantle at most of the subduction zones, except for the hot and slow subduction of young lithosphere (Molina and Poli, 2000, Kerrick and Connolly, 2001).

Most of nitrogen in near-surface of the Earth is stored in the atmosphere, as it account for 78 vol.% of the air, with a total mass of $3.9 \times 10^{18}$ kg (Ozima and Podosek, 2002). The other nitrogen reservoirs were compiled and estimated by Johnson and Goldblatt (2015). Nitrogen in oceanic biomass (including living and dead organisms) is $8 \times 10^{14}$ kg. Soil and terrestrial biomass hold $1.73 \times 10^{14}$ kg nitrogen in total. Although the biomass-related nitrogen is small as compared to the atmosphere, it is still important because biologically fixed nitrogen is responsible for transferring nitrogen into the other reservoirs. Nitrogen abundance in sediments was estimated from the proportion of sediment types covering the oceanic seafloor, yielding $4.1 \pm 2.0 \times 10^{17}$ kg nitrogen.

Carbon contents in the upper mantle are relatively well known. Direct measurement of carbon contents in undegassed MORB glasses showed that the depleted mantle contains 20-74 ppm carbon (72-270 ppm $CO_2$; Saal et al. 2002). Considering that the bulk silicate Earth likely contains on the order of several hundred to thousand ppm of carbon, the carbon abundance in the undepleted mantle should be higher. Analyses of ocean-island basalts (OIB) yield carbon contents in the source mantle in a range of about 60-600 ppm carbon (Dixon et al., 1997, Bureau et al., 1998, Aubaud et al., 2006). However, experimental studies showed that silicate minerals from the upper mantle to the lower mantle may dissolve only a few ppm of carbon (Keppler et al., 2003, Shcheka et al., 2006). These observations imply that the majority of carbon in the mantle does not exist in such major silicate phases, but in accessory phases such as carbonate, graphite, and diamond. Carbonates are important because most of sedimentary carbon is transported into the mantle by subduction as carbonates. Some studies showed that some carbonates are stable under mantle conditions, meaning that carbon can be preserved in carbonate phases (e.g. Beillmann et al., 1993, Issiki et al., 2004, Dasgupta and Hirschmann, 2010 and references therein). Iron-carbide ($Fe_3C$) is also a possible carbon reservoir, which is stable at lower mantle conditions (Rouquette et al., 2008).

The nitrogen content in the mantle is poorly known, since nitrogen is always degassed from mantle samples. Therefore, nitrogen abundances in the mantle are often estimated from $N/^{40}Ar$ ratios, since there is a good correlation of nitrogen contents in mantle samples with $^{40}Ar$, which is a decay product of $^{40}K$. Since the $^{40}K$ abundance in the mantle is well known, one can estimate the mass of $^{40}Ar$ that should be in the mantle. The $N/^{40}Ar$ ratio near 100, where most of the data cluster in in Fig. 1.3, gives about 1 ppm nitrogen in the mantle. But it should be noted that some $N/^{40}Ar$ ratios of OIB and xenolith samples in Fig. 1.3 are much higher – if they represent a deep, undegassed reservoir, there could be up to one order of magnitude more nitrogen in the mantle.

Nitrogen solubility in mantle has been studied by Li et al. (2013). They provided first experimental constraint on nitrogen solubility in upper mantle minerals. Their data showed that up to 100 ppm nitrogen is soluble in aluminous enstatite and diopside at 3.5 GPa under reducing conditions, implying a high storage capacity for nitrogen in the

mantle. However, data for minerals in deeper domain of the mantle, i.e. the transition zone and lower mantle are still missing.

The equilibrium between magmatic degassing and carbon subduction has controlled atmospheric $CO_2$ (and therefore climate) in the past. Whether there is a similar cycle for nitrogen or not is less clear. The history of atmospheric pressure (which is mostly the nitrogen partial pressure) is important for paleoclimate, which is closely related to the evolution of life, because a dense atmosphere could have enhanced the greenhouse effect (Goldblatt at al., 2009). Busigny et al. (2011) suggested that presently much more nitrogen is subducted into the mantle ($13.2 \times 10^8$ kg/yr) than is replenished by degassing ($2.8 \times 10^8$ kg/yr). This implies that surface nitrogen is progressively transferred into mantle. Mitchell et al. (2010) found that in a cold subduction zone (the Izu-Bonin-Mariana arc), the mass of subducted nitrogen is significantly larger than that of degassed nitrogen, suggesting that the devolatilization of nitrogen in the subducted oceanic crust is not complete and a significant fraction of nitrogen is delivered into the deep mantle. These lines of evidence lead to the hypothesis that the atmospheric pressure may have changed over geologic time. However, it is still controversial whether the ancient atmospheric

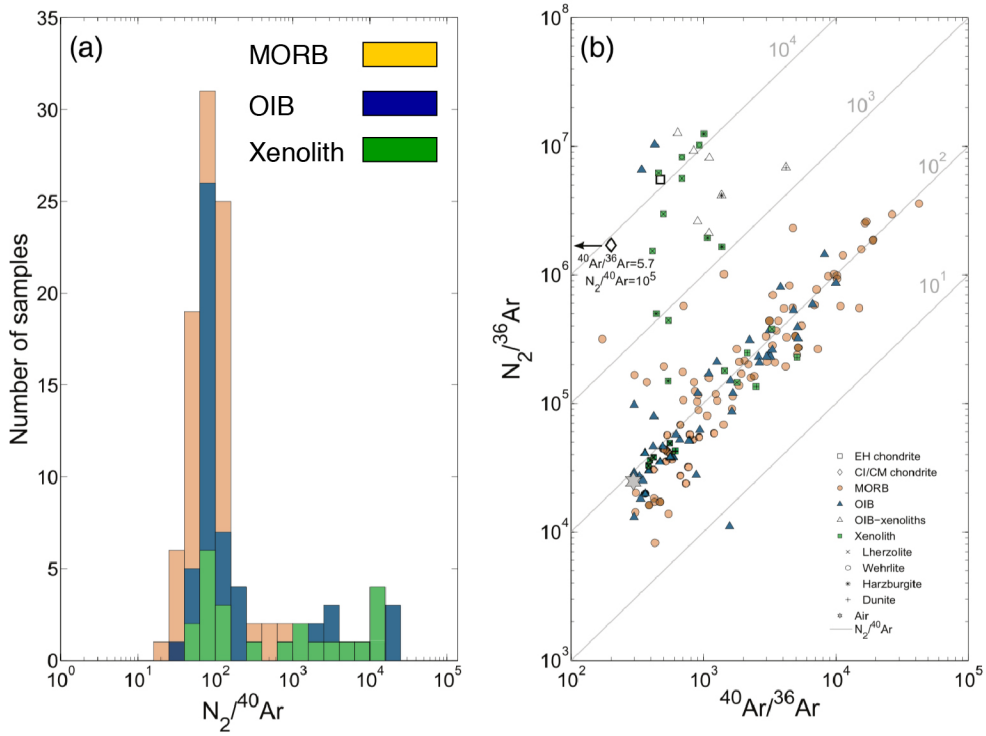


*Fig. 1.3. $N_2/^{40}Ar$ and $^{40}Ar/^{36}Ar$ data for mantle samples. MORB = Mid-Ocean-Ridge Basalt, OIB = Ocean-Island Basalt. (Modified from Johnson and Goldblatt, 2015)*

pressure was similar to that today (Marty et al., 2013) or much higher (Kavanagh and Goldblatt, 2015).

Some carbon and nitrogen in the Earth could have partitioned into the core. Experiments on metal/silicate partitioning suggest that carbon is much more siderophile than nitrogen (Dalou et al., 2017), meaning that during core formation more carbon should have incorporated into the core than nitrogen if metal and silicate were in equilibrium. Partitioning into the core can therefore not be responsible for the low amount of N in near-surface reservoirs (as compared to other volatiles). Overall, what happened in early Earth's history depends very much on processes in the magma ocean stage. But there, essential data are missing: While the solubility of carbon in silicate melts under oxidizing conditions is well known, carbon solubility in silicate melts under reducing conditions relevant for the early Earth is poorly constrained. A few studies (Wetzel et al., 2013, Stanley et al., 2014, Armstrong et al., 2015) looked at carbon solubility in silicate melts in equilibrium with graphite, but under vapor-absent conditions. Therefore, these data are not directly usable for modeling the ingassing or degassing of carbon in early Earth history. Moreover, the speciation of reduced carbon in silicate melts is controversial, with some studies postulating the stability of carbonyl complexes in the melt (Stanley et al., 2014, Wetzel et al., 2015).

## 1.2 Purpose of this thesis

The purpose of this study is to fill some essential gaps in the understanding of the deep geochemistry of nitrogen and carbon. These gaps are related to the storage of these elements in the deep Earth and their behavior during magma ocean crystallization.

- For nitrogen, the storage capacity of the deep mantle is completely unknown. Therefore, the solubility of nitrogen in the minerals of the transition zone and lower mantle was studied. These data have two important implications: (1) They give a robust upper limit of the amount of N that may reside in the deep mantle, and (2) they allow modeling of nitrogen sequestration into the mantle during magma ocean crystallization

- For carbon, the solubility in mantle minerals is well constrained. However, the partitioning of carbon between the surface, the mantle, and the core in early Earth history depends crucially on the solubility of reduced carbon in a magma ocean. This solubility is essentially unknown. Therefore, the solubility of carbon in silicate melts in equilibrium with graphite and a CO-$CO_2$ gas phase was investigated. In addition to constraining the behavior of carbon in a magma ocean, these data also have implications for understanding volcanic activity on the Moon and on other planets, where the mantle remained in a highly reducing state.

# 2. Experimental and analytical methods

## 2.1. Starting materials

Starting materials for high-pressure experiments were either oxide mixtures or glasses, with some source of N or C. Glasses were prepared by mixing the following analytical grade chemicals: $SiO_2$, $TiO_2$, $Al(OH)_3$, $Fe_2O_3$, $Mg(OH)_2$, $CaCO_3$, $Na_2CO_3$ and $K_2CO_3$. Before weighing the powders, each chemical was dried in an oven at 140 °C over night to remove absorbed water. The weighed chemicals were mixed and homogenized with a mortar under ethanol for 1 hour and dried under an IR lamp. The mixture was then transferred into a platinum crucible and gradually heated in a furnace to 1100 °C for 12 hours and kept at this temperature for 6 hours in order to decarbonate the mixture. After this, it was transferred into a high-temperature furnace and melted at 1600 or 1700 °C for 1 hour. The melt was quenched by dropping it into deionized water to obtain a clear homogeneous glass. The glass was crushed into a fine powder for use as starting material.

In the carbon speciation study, a gas-mixing furnace was used to control the oxidation state of a Fe-bearing starting glass. The gas-mixing furnace is a vertical tube furnace using a CO-$CO_2$ gas flow to control oxygen fugacity. The Fe-bearing starting glass was placed into a crucible made of Fe foil. The crucible was suspended inside the furnace with a platinum wire and heated at 1300 °C for 3 hours at an oxygen fugacity one log unit below the iron-wüstite buffer. After 3 hours, the platinum wire was fused by a voltage pulse and the crucible dropped into the bottom of the furnace where it quenched to room temperature.

## 2.2. Internally heated pressure vessel (IHPV)

This apparatus was used to explore carbon solubility in silicate melts at moderate pressure (0.2-0.5 GPa; 2-5 kbar). The IHPV is a high pressure apparatus used for experiments up to 1 GPa and at high temperatures (typically up to 1500 ˚C; e.g. Holloway

1971). This instrument uses an inert gas as a pressure medium and has a relatively large sample chamber, which allows experiments with cm-sized samples.

Starting glasses (Fe-free MORB, andesite and rhyolite) and carbon monoxide gas were loaded into a Pt capsule. The capsule was made of a 3.5 mm outer diameter platinum tube

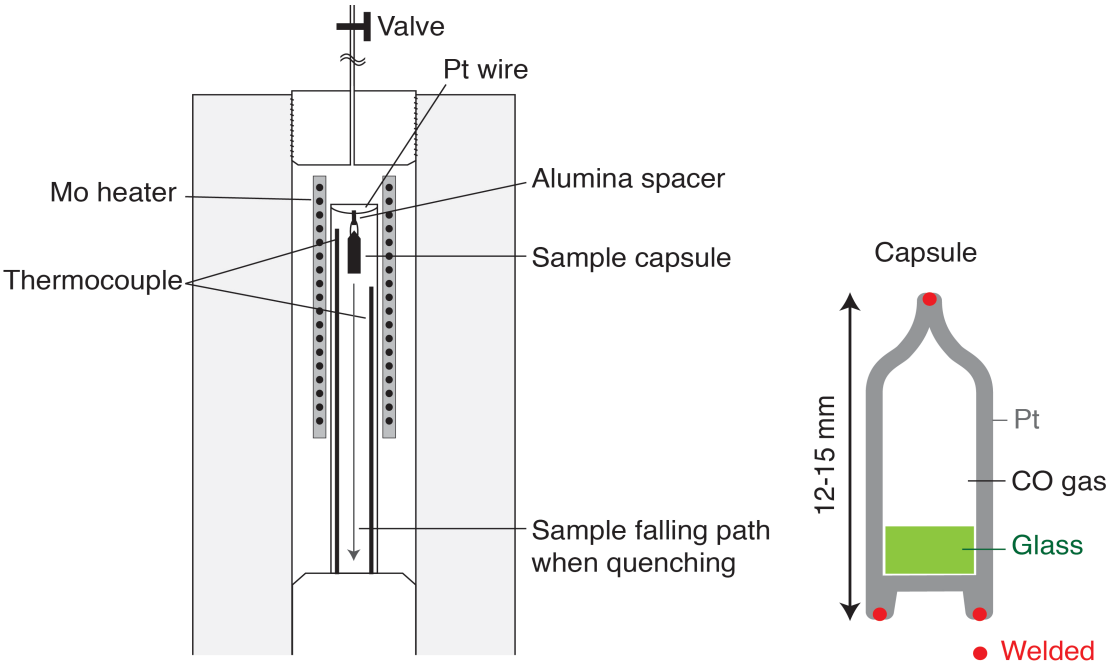


*Fig. 2.1. Schematic diagram of an internally-heated pressure vessel with rapid-quench device (left) and of a sample capsule as used for measuring carbon solubility in silicate melts in equilibrium with graphite and a CO-$CO_2$ gas phase (right).*

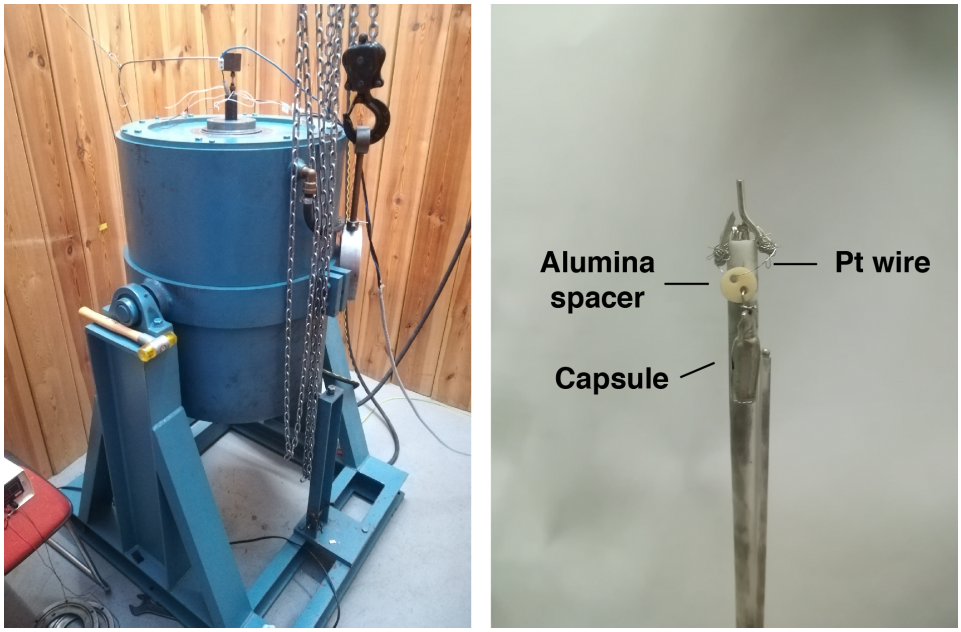


*Fig. 2.2. A rapid-quench IHPV with device at BGI (left) and a sample capsule (right).*

with a wall thickness of 0.2 mm. After a glass was loaded, the capsule was evacuated and then CO gas at ~80 bar was directly loaded into the capsule with a gas-loading device (Boettcher et al., 1989). The capsule was mechanically closed by a vise and welded. After it was released from a vise, it expanded due to the high CO gas pressure in the capsule. During the experiment, the equilibrium 2 CO = $CO_2$ + C (graphite) was expected to be reached.

A series of experiments on carbon solubility was carried out at 0.2-0.5 GPa and 1200-1400 °C with a 150 000 psi Harwood autoclave. 1-3 samples were suspended in the sample chamber using a 0.1 mm diameter platinum wire and an alumina spacer (sliced 2 hole tube). Argon gas was used as pressure medium. Before compression, air was flushed out of the vessel by injecting and releasing >100 bar Ar gas for two times in order to avoid oxidation of the heaters. After the Ar gas was compressed to the target pressure using a Nova Swiss MK 3000 gas compressor, samples were gradually heated by a two-zone molybdenum heater. Two thermocouples were located above and below the samples, 15 mm apart from each other. As the internal pressure increases upon heating, it was adjusted by releasing Ar gas. After the end of an experiment, samples were rapidly quenched by dropping them into the cold part of the autoclave by fusing the platinum wire with a voltage pulse. The recovered capsules were weighed and punctured to check for leakage during the experiment. Upon opening, a sound of gas flow and significant weight loss was observed, indicating there was still pressure inside the capsules and no leakage occurred during experiment. All samples had graphite inside the capsule wall or glass after the experiment.

## 2.3. Piston cylinder apparatus

This apparatus was used to investigate CO speciation in silicate melts and to extend the carbon solubility measurements to higher pressure. The piston cylinder apparatus (Boyd and England, 1960) is a widely used instrument for upper mantle pressures (typically 1-5 GPa), which uses a solid pressure medium and allows obtaining large volume samples. The end-loaded type has two hydraulic rams. The lower one compresses the sample assembly by a piston, while the second one vertically compresses and strengthens a

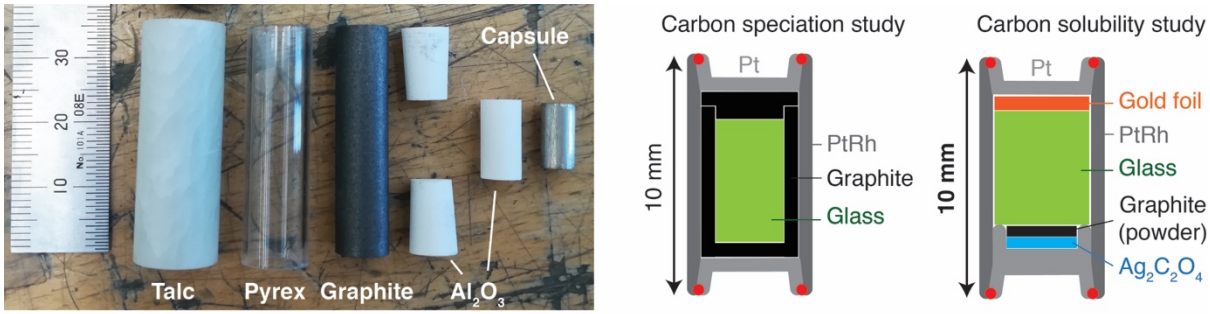


*Fig. 2.3. Sample assembly parts of piston-cylinder experiments (left) and schematic diagrams of sample capsules used for studying carbon speciation and carbon solubility in silicate melts (right).*

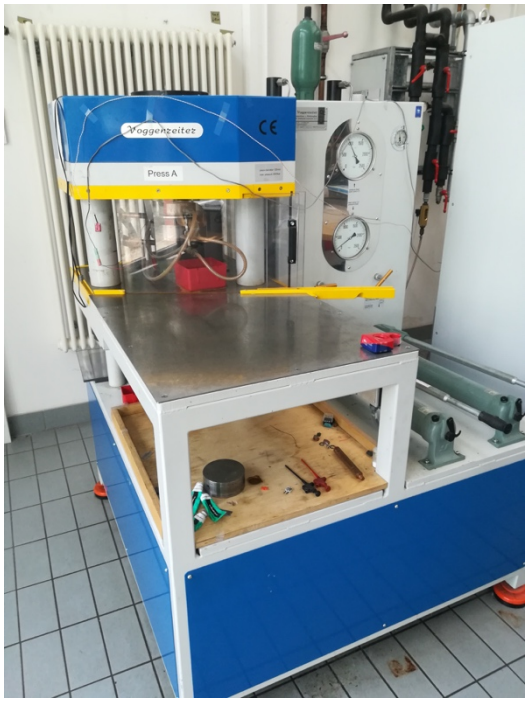


*Fig. 2.4. A end-loaded piston-cylinder apparatus at BGI*

pressure vessel. The pressure vessel consists of a steel bomb and a tungsten carbide core with a cylindrical cavity containing the sample assembly.

To study CO speciation in silicate melts, an outer PtRh-Pt capsule (5 mm diameter, 10 mm height and 0.3 mm wall thickness) containing an inner graphite capsule was used. The graphite capsule was also the source of dissolved carbon. Three series of experiments were carried out using different starting glasses. The first one was a Fe-bearing MORB composition and second one was a Fe-free MORB, where all Fe was replaced by an equimolar mixture of Ca and Mg. The third starting material was a Fe-free MORB doped with 0.5 wt% $^{57}Fe_2O_3$ for Mössbauer spectroscopic measurements. With the Fe-bearing MORB starting material, some pieces of iron metal were added to maintain reducing

conditions. Even in this nominally anhydrous system, some water was always detected in the run products due to a absorbed water in starting materials.

In the carbon solubility study, Fe-free MORB, andesite and rhyolite glasses were used as a starting materials. Their compositions correspond to representative natural rocks, with the exception that all Fe was replaced by an equimolar mixture of Ca and Mg. To produce a CO-$CO_2$ gas phase, $Ag_2C_2O_4$ and graphite powder were also loaded into the capsule. $Ag_2C_2O_4$ decomposes to silver metal and $CO_2$ upon heating, which then equilibrates at high temperature with graphite to form CO according to $CO_2$ + C (graphite) = 2 CO. Gold foil was also loaded to remove silver particles from the melt by alloying because clear transparent glass is necessary for FTIR measurements. As a standard samples for SIMS measurements, glasses containing only oxidized carbon were also synthesized. In these experiments, $Ag_2O$ was added instead of graphite powder, in order to oxidize all carbon to $CO_2$ or carbonate.

The experiments were carried out with an end-loaded piston cylinder apparatus at 1-3 GPa and 1400-1600 °C. The sample assembly consisted of, from outside to inside, a talc tube, a pyrex (borosilicate glass) tube, a graphite heater, an $Al_2O_3$ sleeve and a capsule. Beneath and above the capsule, $Al_2O_3$ spacers (disk, powder and block) were placed. The outer diameter of the assembly was 1/2 or 3/4 inches. To monitor the temperature of the capsule, a D-type thermocouple ($W_{97}Re_3$-$W_{75}Re_{25}$) was inserted above the capsule with a four-hole $Al_2O_3$ sleeve. In the experiments, the assembly was gradually pressurized to an target pressure for 30 minutes. After the target pressure was reached, the assembly was heated at a rate of 100 °C/min. During heating, the pressure vessel was water-cooled. The assembly was rapidly quenched to a room temperature by shutting off the current. The sample was recovered after gradual decompression for 30 minutes.

## 2.4. Multi-anvil apparatus

A multi-anvil apparatus was used to measure nitrogen solubility in minerals. This type of solid-media high-pressure device can be used for the pressure range covering the entire upper mantle to the uppermost lower mantle (25 GPa). A Kawai-type multi-anvil

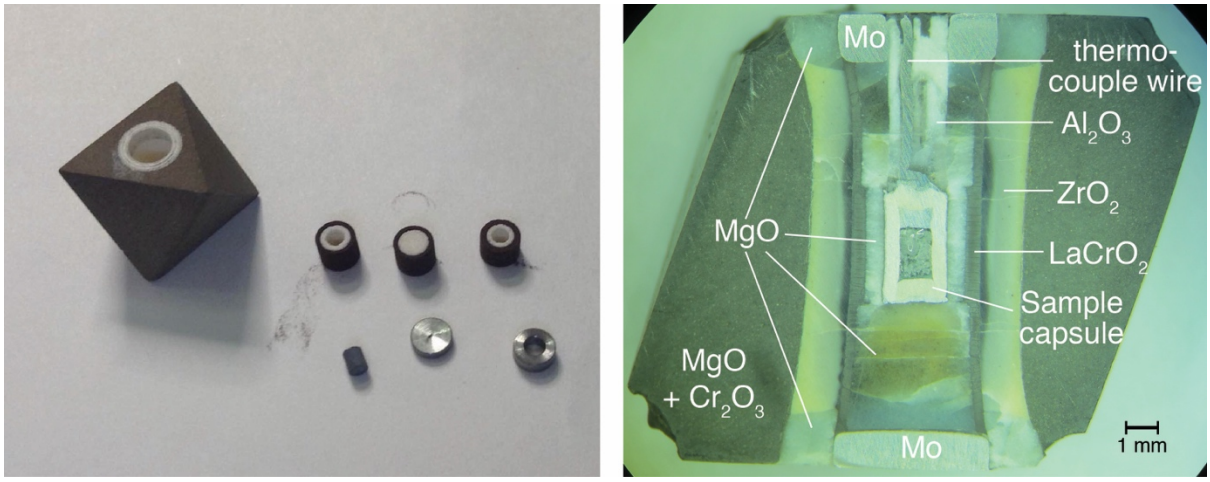


*Fig. 2.5. Sample assembly parts of multi-anvil experiments (left) and a cross section of a sample assembly (right).*

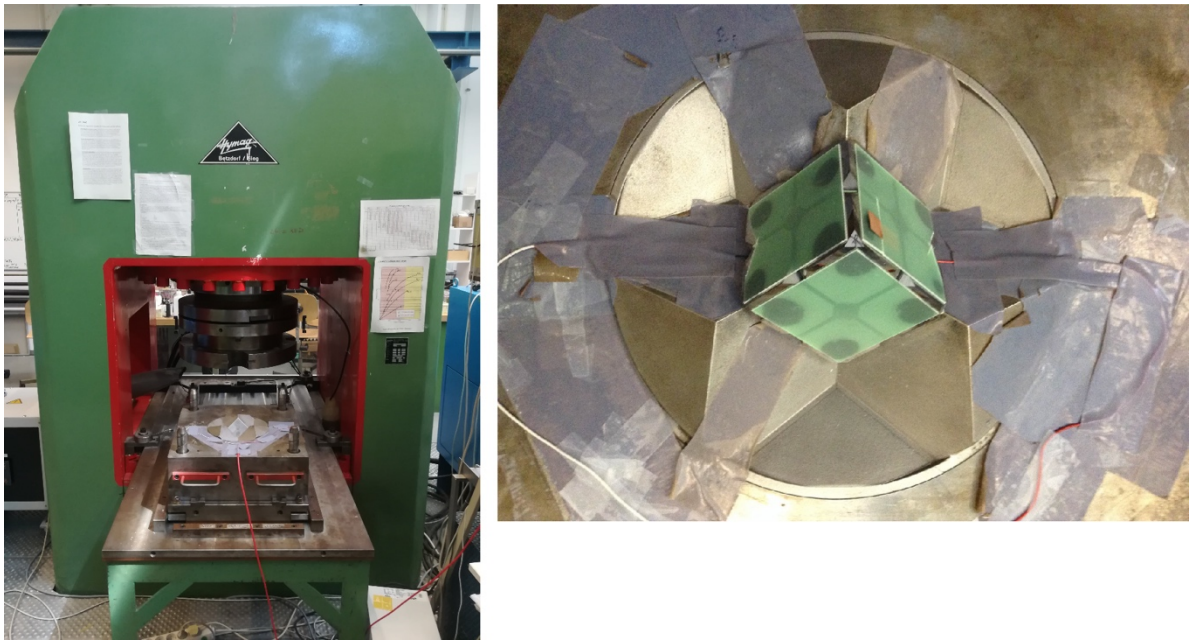

*Fig. 2.6. A 1000-ton multi-anvil press at BGI (left); secondary anvils with a sample assembly placed on the guide blocks (right).*

apparatus (Kawai and Endo, 1970) uses eight tungsten carbide anvils (secondary anvils) and two outer guide blocks (first-stage anvils). The secondary anvils have truncation edges, which directly compress the sample assembly. The sample assembly typically consists of an outer $MgO+Cr_2O_3$ octahedral ceramic pressure medium, a $ZrO_2$ thermal insulator, a $LaCrO_3$ heater, a MgO or $Al_2O_3$ spacer and a capsule. A molybdenum ring and disk were also used to improve electrical contact (Fig. 2.5).

Stoichiometric mixtures of oxides with compositions equivalent to the target minerals (wadsleyite, ringwoodite, bridgmanite) were prepared as starting materials. To enhance

crystal growth, 20 wt.% of $Na_2CO_3$ was added as a flux agent. Only for Ca-silicate perovskite, a glass with stoichiometric composition was prepared because it was impossible to obtain large crystals from an oxide mixture. Capsule were made of a PtRh tube and two Pt disks with a size of 1.6 × 1.1 × 3.0 mm (outer diameter × inner diameter × height) or 1.2 × 1.0 × 2.4 mm. The starting silicate component, Fe metal powder and $^{15}NH_4{}^{15}NO_3$ were loaded and sealed by welding. Fe metal was used to keep the oxygen fugacity close to the iron-wüstite buffer, which is considered to be similar to the transition zone and lower mantle conditions (Frost and McCammon, 2008). A $^{15}N$-labeled nitrogen source was used to distinguish atmospheric nitrogen interference from nitrogen dissolved in a mineral during SIMS measurement.

A series of experiments was carried out at 14-24 GPa and 1100-1800 °C with a 1000/1200-ton or 5000-ton press. The pressure calibration curves were according to Keppler and Frost (2005). A 1000/1200-ton press with 14/8, 10/5 and 10/4 assemblies (octahedral edge length/truncation edge length in mm) was used for experiments at 14-15 GPa, 17-19 GPa and 21-24 GPa, respectively. Only a few runs were carried out in a 5000-ton press with a 18/11 assembly. The octahedral pressure medium with the $ZrO_2$ sleeve, the MgO and $Al_2O_3$ parts were initially heated to 1000 °C for 45 minutes under atmospheric pressure to remove absorbed water. A $W_{95}Re_5$-$W_{74}Re_{26}$ thermocouple with four-hole $Al_2O_3$ tube was inserted above the capsule. Pieces of 1-hole $Al_2O_3$ tube and Cu coil were additionally used to protect the thermocouple wire from compression. After the secondary anvils and the assembly were constructed, epoxy sheets were attached to the anvils in order to hold them together. Electrical contact between the first stage anvils and the assembly was maintained by placing Cu foil across the epoxy sheets on two secondary anvils, which are in contact with the Mo parts of the assembly. Upon experiments, the assembly was compressed to a target pressure over about 4 hours. After the target pressure was reached, the sample area was heated gradually heated at a rate of 100 °C/min to a target temperature. The assembly was rapidly quenched to a room temperature by shutting off the current. The sample was decompressed to an ambient conditions over about 9 hours.

## 2.5. Secondary ion mass spectrometry (SIMS)

This analytical method was used to quantify carbon solubility in silicate glasses and nitrogen solubility in minerals. SIMS is a mass spectrometry technique for quantifying concentrations of trace elements and isotopes with high spatial resolution. The ion probe employs a focused ion beam (primary ions), which sputters the sample surface in order to extract ions from the sample (secondary ions). The extracted secondary ions are passed through a mass spectrometer for mass separation. $^{16}O^-$ and $^{133}Cs^+$ are commonly used as primary ions, which extract positive and negative secondary ions, respectively. Secondary ions separated by the mass spectrometer are detected by electron multipliers or Faraday cups. During analysis, two secondary ions of both sample and of a reference material are measured. A reference material for a sample must have similar major element composition and structure, because these factors affect the ionizing efficiency of secondary ions. For measuring nitrogen, $^{15}N^+$ and $^{28}Si^{++}$ were measured from secondary ions. $^{15}N$ in a sample was then calculated from the equation

$$\left[\frac{\left(\frac{^{15}N^+_{cps}}{^{28}Si^{++}_{cps}}\right)}{\left(\frac{^{15}N_{ppm}}{^{28}Si_{atom\%}}\right)}\right]_{Reference} = \left[\frac{\left(\frac{^{15}N^+_{cps}}{^{28}Si^{++}_{cps}}\right)}{\left(\frac{^{15}N_{ppm}}{^{28}Si_{atom\%}}\right)}\right]_{Sample}$$

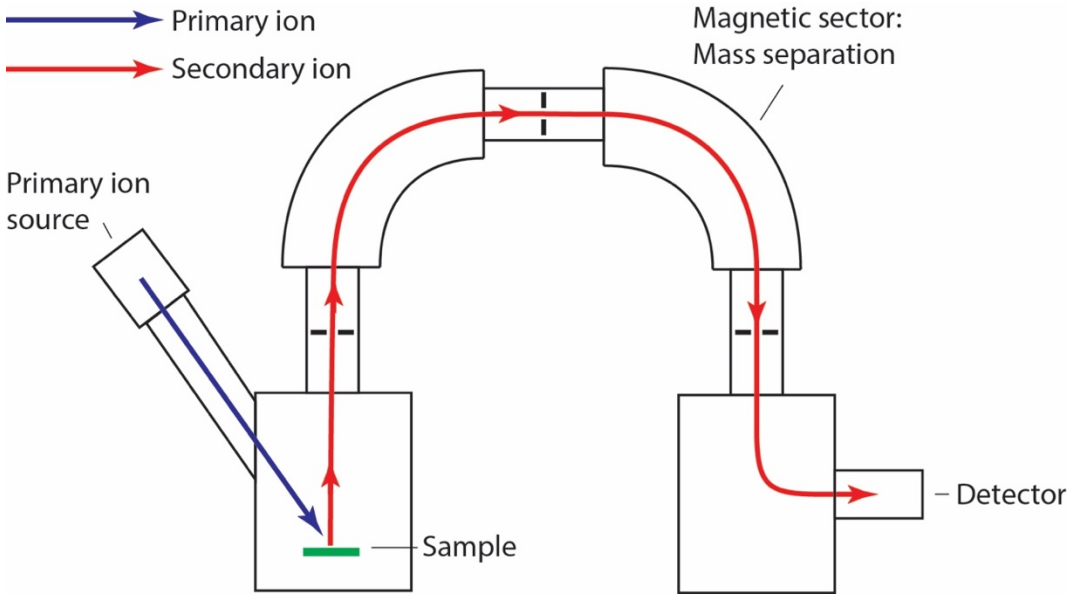


*Fig. 2.7. A simplified schematic diagram showing the principle of SIMS. Secondary ions are extracted from a sample by a primary ion beam. Secondary ions are separated according to their mass and transferred to a detector section.*

where $^{15}N^{+}_{cps}$ is measured secondary ion $^{15}N^{+}$ in cps (count per seconds), $^{15}N_{ppm}$ is $^{15}N$ concentration in ppm.

In the study on nitrogen solubility in minerals, a series of measurements were carried out with a Cameca 1280-HR ion probe at the Helmholtz Zentrum Potsdam. Samples embedded in epoxy were cleaned with high-purity ethanol in an ultrasonic bath and coated with a 35 nm thick gold layer. A $^{16}O^{-}$ primary ion beam was focused to a ~10 μm diameter spot with a 13 kV accelerating voltage and 20-24 nA primary current. The mass resolution was set at ~2500. In one measurement cycle, signals of $^{28}Si^{++}$, $^{14}N^{-}$ and $^{15}N^{-}$ were collected. As reference materials, $^{15}N$-implanted enstatite was used for bridgmanite and Ca-silicate perovskite, and $^{15}N$-implanted forsterite for the other minerals. These references were chosen because they are compositionally similar to the samples and because they are stable under the ion beam and during ion implantation, while the high-pressure phases easily become amorphous. For preparing the standards, a maximum dose density equivalent to 51 μmol/mol $^{15}N$ in the forsterite and 501 μmol/mol in the enstatite was implanted 200 nm below the surface. During measurement, no pre-sputtering was used on the standards. Synthetic buddingtonite with natural isotopic composition was also measured under the same condition as used for the references in order to estimate nitrogen interference from the atmosphere in the samples. Analyses of the samples were carried out in spot-mode after pre-sputtering.

For measuring carbon solubility in glasses, a series of SIMS analyses was carried out with a Cameca IMS-7f Ion MicroAnalyzer at Tohoku University. Samples mounted on glass slides by a ceramic glue were cleaned with distilled water in an ultrasonic bath and coated with gold. A $Cs^{+}$ ion was used as a primary ion with 1-1.5 nA current and 10 kV acceleration voltage. The measured spot on the sample surface was a 17x12 μm area. The extraction voltage of secondary ions was 5 kV and an E-gun was used to compensate electric charge on the sample surface. The mass resolution was ~4000. In one measurement cycle, after pre-sputtering with a 25x25 μm raster, signals of $^{12}C^{-}$, $^{28}Si^{-}$ and at mass 28.5 e/m were measured. The calibration was done using $CO_2$-bearing standard glasses synthesized with the piston cylinder apparatus. Three glasses of MORB and andesite and two glasses of rhyolite with different carbon contents quantified by FTIR were used as reference material. According to the calibration curve obtained from the standards, the cps (counts per second) ratio of $^{12}C$ and $^{28}Si$ was converted into carbon

content. Before this, the cps of $^{28}Si$ and $^{12}C$ were background-corrected by subtracting the cps of mass 28.5 e/m and the cps of $^{12}C$ measured on C-free blank glasses, respectively.

## 2.6. Fourier transform infrared spectrometry (FTIR)

A Fourier transform infrared spectrometer (FTIR) was used to determine the speciation of dissolved carbon or nitrogen in glasses or minerals. It was also used to quantify dissolved $CO_2$ and carbonate in glasses. FTIR is typically used to determine the structure of a material by probing vibrational frequencies. It is also sometimes used for the quantification of some components such as water in a sample. A FTIR spectrometer principally consists of an IR light source, an interferometer with beam splitter, fixed and moving mirrors, and a detector. The purpose of the interferometer is to mark every frequency or wavelength in the radiation emitted from the source by a characteristic modulation. A sample is placed between the interferometer and the detector where the light intensity as a function of time (interferogram) is measured. The interferogram is converted to a spectrum using Fourier transformation. The absorption spectrum is calculated from a spectrum measured with sample and background spectrum measured

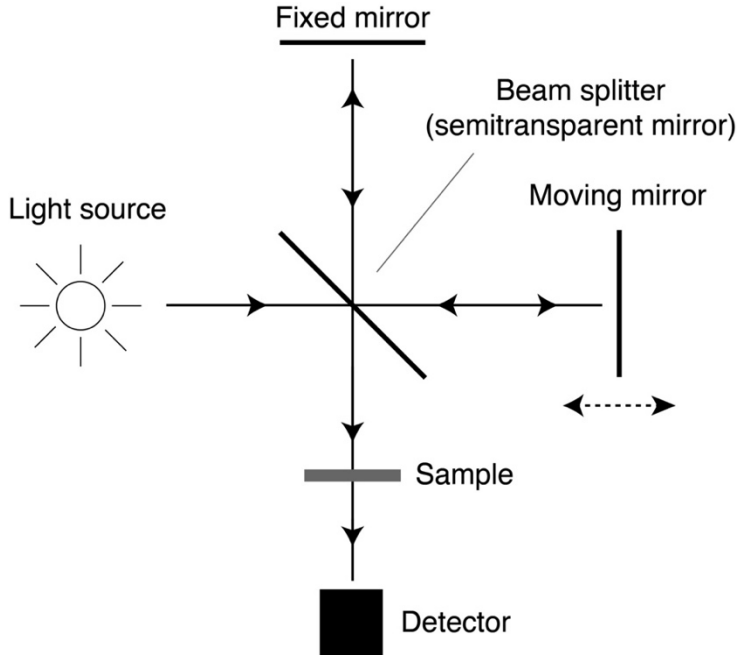


*Fig. 2.8. A schematic diagram of an FTIR instrument. After passing through the interferometer, the beam used for measurement is modulated. The modulation contains the information on the intensity distribution as a function of frequency.*

without a sample; it is usually given as absorbance versus a wave number. According to the Lambert Beer low, the concentration of an absorbing species *C* can be quantified using an equation

$$C = \frac{m \cdot A}{\varepsilon \cdot \rho \cdot d}$$

where m is the molar mass of absorbing species, **A** is absorbance (usually integrated area or peak height), **ε** is the extinction coefficient, ρ is the density of the material and d is the thickness of the sample.

Measurements were carried out with a Bruker IFS 120 HR spectrometer coupled to a Brucker A490 microscope with an all-reflecting 15x Cassegranian objective. A globar light source, a KBr beam splitter, and a narrow-band MCT detector were used. Samples were sliced to less than 250 μm thickness and doubly polished for measurements.

## 2.7. Raman spectroscopy

Raman spectroscopy was used to determine the speciation of dissolved carbon or nitrogen in glasses or minerals. It was also used for phase identification. Like FTIR, Raman spectroscopy probes vibrational frequencies in a sample. However, the selection rules for Raman and infrared activity are different, such that the two methods often give complementary information. Raman spectroscopy is based on light scattering. When light interacts with a material, light with different frequency may be emitted (Raman scattering). The frequency difference is called Raman shift, often expressed in a unit of $cm^{-1}$. The emission observed at lower and higher frequency relative to the incoming radiation is called Stokes scattering and anti-Stokes scattering, respectively. Although their absolute shifts in frequency are equal, Stokes scattering is normally used for analysis because of its higher intensity. As a Raman spectrum reflect the structure of a material, it is typically used for the identification of phases and for studies of structure and chemical bonding. In principle, a Raman spectrometer consists of a monochromatic light source, objective lens, grating and detector. The light source is usually a laser. The

laser is focused on the sample surface and scattered light is measured at the detector after passing through the objective lens and the grating.

Raman spectra were obtained with a confocal Horiba-Yvon Labram 800HR UV spectrometer equipped with a 514 nm Ar laser. Spectra were accumulated using a 50x objective lens, a 1800 $mm^{-1}$ grating and a Peltier-cooled CCD detector. Filters to reduce the intensity of the laser by up to one order of magnitude were sometimes used to avoid radiation damage.

## 2.8. Mössbauer spectroscopy

This method was used to determine the oxidation state of iron in some glasses. Mössbauer spectroscopy is based on γ-ray absorption which is caused by transitions within atomic nuclei. When γ-rays of appropriate energy interact with the sample, specific nuclei may be excited to a higher energy level, resulting in γ-ray absorption. The precise absorption energy depends on the chemical environment of the nucleus and the effect can therefore be used to infer oxidation states. As a γ-ray source, $^{57}Co$ is mostly used, which decays to an excited state of $^{57}Fe$. The γ-ray emitted by this excited state of $^{57}Fe$ upon transition to the ground state can then be used to probe the chemical environment of $^{57}Fe$ in a sample. By moving the γ-ray source relative to a sample, the energy of the γ-ray may be tuned by the by Doppler effect such that absorption is observed.

## 2.9. Other methods

A JEOL JXA-8200 electron microprobe was used to measure major element compositions of samples. This method was also used to quantify nitrogen solubility in Fe-Pt alloy. In this case, a blank sample (Fe metal) was measured in addition, because of the strongly curved background at the X-ray position of nitrogen. TiN was used as a standard. A relatively weak electron beam was defocused to a 5 μm spot in order to avoid evaporation of nitrogen.

X-ray diffraction probes the crystal structure of a sample according to the Bragg equation. X-ray diffraction measurements were carried out for phase identification of a few samples using a micro-focus X-ray diffractometer (MF-XRD) Bruker D8 DISCOVER.

# 3. Results and discussion

## 3.1. The speciation of carbon monoxide in silicate melts and glasses

The aim of this study was to reveal the speciation of carbon monoxide in silicate melts, in particular to test the hypothesis proposed by Wetzel et al. (2013) that CO dissolves in reduced basaltic melts as iron pentacarbonyl $Fe(CO)_5$ . To achieve this, I prepared both Fe-bearing and Fe-free MORB-composition glasses synthesized under graphite-saturated condition at 1 GPa and 1450-1530 °C.

### *3.1.1. Raman, infrared and Mössbauer spectra*

Fig. 3.1a shows Raman spectra of both Fe-bearing and Fe-free glasses. The Raman spectra of Fe-bearing glasses showed a peak at 2110 $cm^{-1}$, which is very similar to the peak assigned to $Fe(CO)_5$ by Wetzel et al. (2013). The peak, however, appears also in the spectra of Fe-free glasses. This observation rules out any assignment of this band to a Fe-bearing species. Moreover, a strong peak at 2014 $cm^{-1}$ observed in a Raman spectrum of pure $Fe(CO)_5$ was not seen in spectra of the glasses. Infrared spectra of both Fe-bearing and Fe-free glasses also show an absorption band at 2210 $cm^{-1}$ (Fig. 3.1b), which is similar to a band at 2205 $cm^{-1}$ observed and assigned to $Fe(CO)_5$ by Stanley et al. (2014). In this case, too, the band cannot be due to any Fe-bearing species because it appeared in spectra of both Fe-bearing and Fe-free glasses.

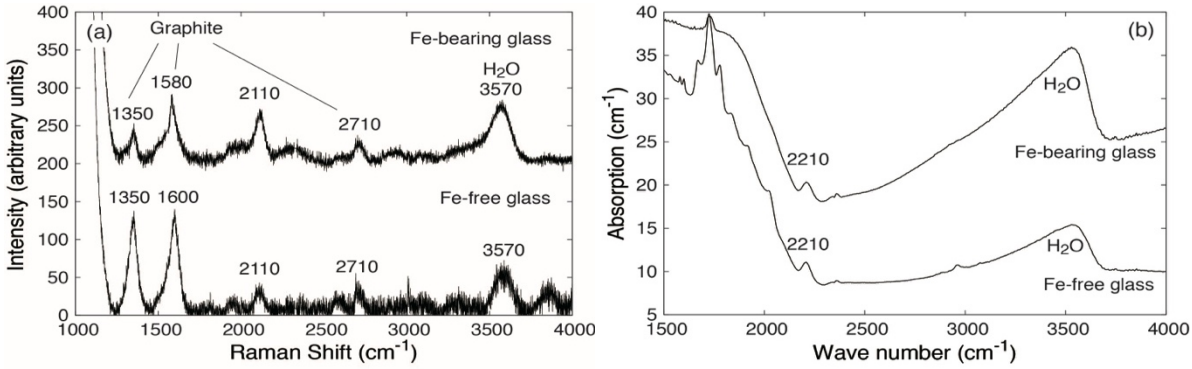


*Fig. 3.1. (a) Raman spectra and (b) infrared spectra of Fe-bearing and Fe-free glass.*

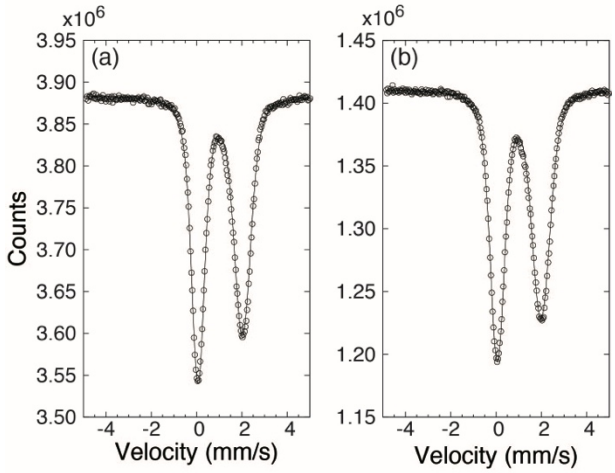


*Fig. 3.2. Mössbauer spectra of (a) Fe-bearing glass and (b) Fe-free glass + 0.5 wt.% $^{57}Fe_2O_3$.*

To identify the oxidation state of iron in the glasses, they were also studied by Mössbauer spectroscopy. Fig. 3.2 shows Mössbauer spectra of a Fe-bearing glass and a glass which was prepared by adding 0.5 wt.% $^{57}Fe_2O_3$ to the Fe-free glass. Only the normal doublet of $Fe^{2+}$ was seen in both spectra, whereas no absorption is observed near zero isomer shift, where $Fe^0$ would be expected. Considering that the oxidation state of Fe in $Fe(CO)_5$ is zero, it is not plausible that $Fe(CO)_5$ is a major species dissolved in these glasses.

### *3.1.2. Thermodynamic calculations*

The equilibrium constant for the reaction

$$Fe + 5\ CO = Fe(CO)_5$$

was calculated from the thermodynamic properties of $Fe(CO)_5$ from Behrens (1977) and the standard state thermodynamic data for carbon monoxide and iron metal from Robie and Hemingway (1995). These data yield

$$\ln K = -66.71 + 20363 / T$$

where K is the equilibrium constant and T is temperature in Kelvin. K is defined as

$$K = \frac{f_{Fe(CO)_5}}{a_{Fe} f_{CO}^5}$$

where f are fugacities and a is activity. From these equations, the fugacity of $Fe(CO)_5$ was calculated as a function of temperature and carbon monoxide fugacity. The activity of iron was considered to be 1 by assuming that the samples were in equilibrium with metallic iron. The results showed that at the pressure and temperature range of crust and uppermost upper mantle, the ratio of $Fe(CO)_5$ fugacity to carbon monoxide fugacity is negligibly small ($<\sim10^{-6}$). If the activity of iron is below 1, i.e. if the sample is not in equilibrium with metallic iron, the fugacity of $Fe(CO)_5$ will be even lower. These calculations suggest that $Fe(CO)_5$ is unlikely to be a stable species at magmatic temperatures.

### *3.1.3. Assignment of bands observed at 2100-2200 cm$^{-1}$ region*

The bands observed at 2100-2200 cm$^{-1}$ in Raman and FTIR spectra measured in previous studies are likely due to isolated CO molecules dissolved in a glass. The extensive literature on CO absorption on surfaces shows that Raman and infrared bands of CO absorbed on oxides or other surfaces shift due to interaction with the substrate. Therefore, the bands at 2100-2200 cm$^{-1}$ are likely caused by CO molecules weakly interacting with the glass matrix. In silicate melts at high temperature, such weak interactions are small compared to the thermal energy and CO solubility should depend on pressure, temperature and the bulk structure of the silicate melts, expressed by the degree of polymerization or ionic porosity. Theoretical studies of surface absorbed CO suggest that CO molecules in different environments may have different absorption coefficients (Neyman and Rösch, 1992), implying that matrix-specific calibrations may be required to quantify CO concentrations in glasses by infrared spectroscopy.

## 3.2. Carbon solubility in silicate melts in equilibrium with a CO-$CO_2$ gas phase and graphite

### *3.2.1. Run products*

Carbon solubility in silicate melts saturated with both graphite and a CO-$CO_2$ gas phase was studied at 0.2 – 0.5 GPa in an internally-heated pressure vessel (IHPV) and at 1 – 3 GPa in a piston cylinder apparatus. The run products of IHPV and piston cylinder experiments were clear glasses containing graphite and sometimes fluid inclusions. Raman spectra of the fluid inclusions showed sharp CO and $CO_2$ peaks in the gas phase without any clear evidence for other gas species. These observations suggest that during high pressure and temperature experiments, the melts were under conditions where CO-$CO_2$ gas phase and graphite were saturated.

### *3.2.2. Bulk carbon solubility*

Fig. 3.3 shows bulk carbon concentrations in the samples as quantified with SIMS. Fig. 3.3a indicates that carbon solubility increases with pressure for all melt compositions. The relationship for MORB is linear over the entire pressure range studied, whereas for andesite and rhyolite the trends follow a shallower slope at low pressure than at high pressure. These observations mean that the Henry coefficients for bulk carbon solubility for andesite and rhyolite melts increase with pressure (Table 3.1). Temperature has a

*Table 3.1. Henry coefficients of bulk carbon solubility (ppm/MPa) in silicate melts in equilibrium with graphite and a CO-$CO_2$ gas phase.*

| | Henry coefficient 1300 ˚C up to 0.5 GPa | Henry coefficient all data |
|---|---|---|
| MORB | 1.80 (14) | 2.15 (13)* |
| Andesite | 0.69 (4) | 1.57 (10) |
| Rhyolite | 1.26 (13) | 2.14 (8) |

*All Henry coefficients are given in ppm by weight of carbon per MPa. Numbers in parentheses give the standard error in the last digits of the Henry constant. For the calculation of the Henry coefficient of MORB, one point with anomalously low carbon solubility was discarded.*

subordinate effect on bulk carbon solubility as compared with pressure. There is a relatively minor effect of temperature at 0.3 GPa. Especially for rhyolite, temperature has slightly negative effect. On the other hand, at 2 GPa carbon solubility in MORB significantly increases while for andesite and rhyolite the trend is not clear. Such a change from a negative to a positive temperature dependence of solubility is known for water (e.g. Holtz et al., 1995). When comparing bulk carbon solubility from the present study with data on pure $CO_2$ solubility, it is important to consider that the fraction of CO in a CO-$CO_2$ gas phase in equilibrium with graphite is strongly dependent on pressure and temperature. According to Le Chatelier's principle, in the equilibrium $2\ CO = CO_2 + C$, the reaction shifts to the right when pressure increases and temperature decreases. Fugacities of CO and $CO_2$ can be calculated from the experimentally calibrated oxygen fugacity of a CO-$CO_2$ gas phase in equilibrium with graphite (Jakobsson and Oskarsson, 1994) and thermodynamic data for CO and $CO_2$ tabulated by Robie and Hemingway (1995). For example, at 1300 ˚C the molar fraction of CO in the gas phase is about 37 % at 0.2 GPa, 18 % at 1 GPa and 2 % at 3 GPa. At 3 GPa, it increases from 2 % at 1300 ˚C to 8 % at 1600 ˚C. Since the CO fraction in a CO-$CO_2$ gas at the conditions of the present study is low, whereas $CO_2$ is the dominant component, bulk carbon solubility data from the present study are comparable to data for $CO_2$ solubility. Available data for $CO_2$ solubility in silicate melts up to 0.7 GPa compiled by Ni and Keppler (2013) yield 1.55 ppm of carbon per MPa. This is the same range as the Henry coefficient observed in the present study for MORB and rhyolite at pressure up to 0.5 GPa. Therefore the data provided by the present study suggest that bulk carbon solubility in silicate melts in equilibrium with a CO-$CO_2$ gas phase buffered by graphite is by no means much lower than the solubility of pure $CO_2$.

### *3.2.3. Speciation and solubility of reduced carbon*

The infrared spectra of glasses quenched from melts in equilibrium with a CO-$CO_2$ gas phase were measured. Absorption bands of carbonates and/or $CO_2$ molecules were prominent in the spectra. In accordance with previous studies (Ni and Keppler, 2013), carbonates were dominant in MORB glasses, whereas $CO_2$ molecules prevailed in rhyolite glasses; in andesite glasses, both carbonate and molecular $CO_2$ were present.. Weak

bands in the 2100 - 2200 $cm^{-1}$ region, which may be assigned to CO (Yoshioka et al., 2015), were only occasionally observed. Similarly, Raman spectra of the glasses showed CO-related bands only in a few samples. C-H stretching bands near 2900 $cm^{-1}$ were only detected near graphite inclusions and may represent surface absorbed material. Methane was not observed in the Raman spectra of fluid inclusions, in agreement with the nominally anhydrous conditions of the experiments. Therefore, it is plausible to assume that all reduced carbon in the glasses is likely related to dissolved CO.

Fig. 3.4a,b,c show concentrations of reduced carbon in the glasses, which were calculated by subtracting concentrations of oxidized carbon ($CO_2$ and carbonate) quantified with the infrared spectra from bulk carbon contents measured by SIMS. As the SIMS measurements were calibrated by FTIR data and the procedure of evaluating carbon in SIMS standards was exactly same as for the determination of oxidized carbon in the samples, the calculated concentration of reduced carbon should be reliable, although the statistical uncertainties are significant. A comparison of Fig. 3.3 and Fig. 3.4a,b,c suggests that the fraction of reduced carbon in the bulk carbon concentrations is about 10 - 20 % in MORB and rhyolite glasses, while the fraction in andesite glasses is lower and about 5 %. The similarity of the reduced carbon concentrations in MORB and rhyolite cannot be explained by a simple ionic porosity argument, because ionic porosity decreases as the melt composition becomes more mafic (i.e. MORB has a lower ionic porosity than rhyolite). Possibly, some kind of chemical interaction with the silicate melt may affect the

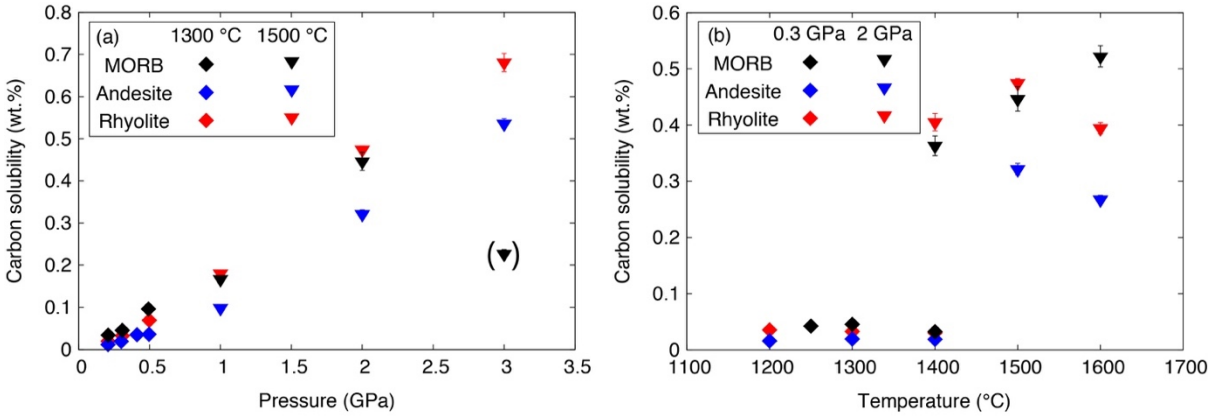


*Fig. 3.3. Bulk carbon solubility in silicate melts coexisting with a CO-$CO_2$ gas phase and graphite as a function of (a) pressure and (b) temperature. The MORB data point at 3 GPa shown in brackets is anomalously low, possibly due to a leak of the capsule.*

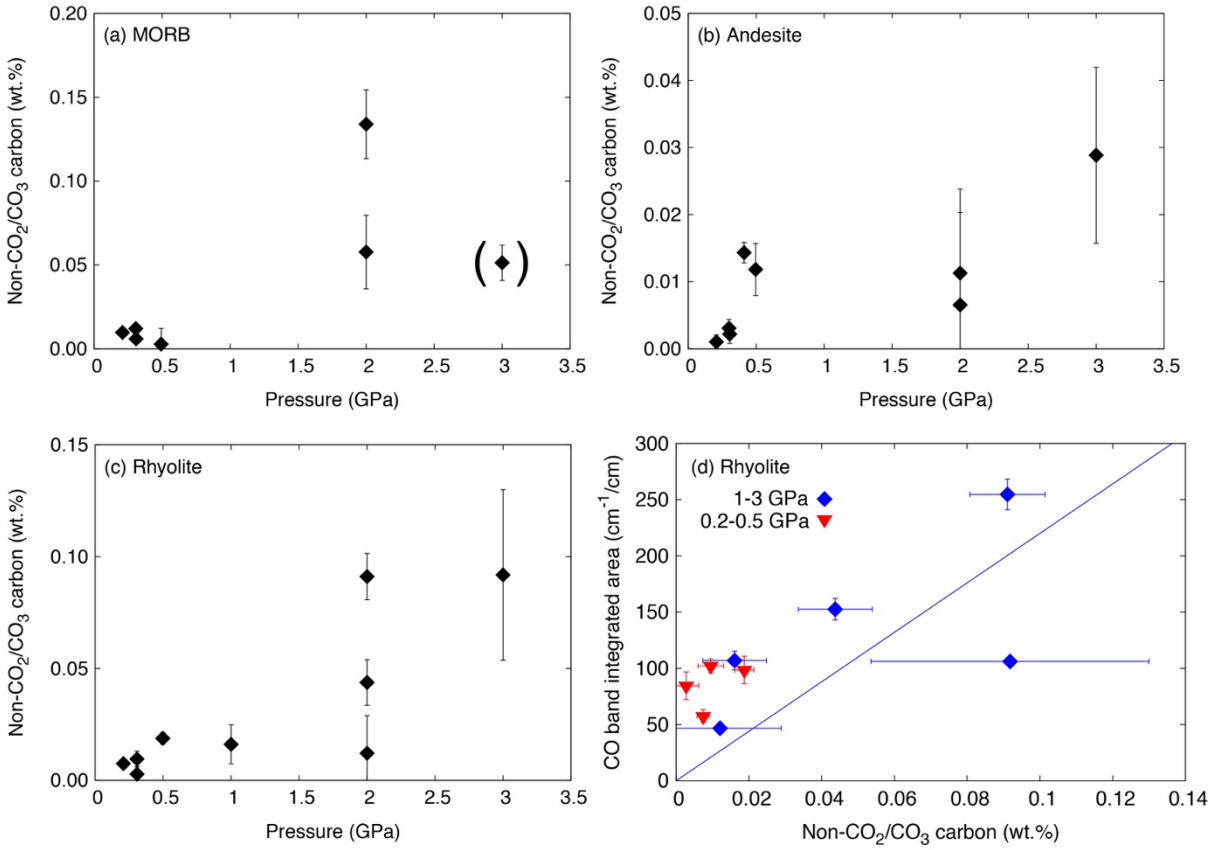


*Fig. 3.4. (a)-(c) Solubility of reduced carbon in silicate melts in equilibrium with CO-$CO_2$ gas phase and graphite as a function of pressure. Data were obtained by subtracting the $CO_2$ content determined by FTIR from the bulk carbon data obtained by SIMS. The MORB data point shown in brackets has anomalously low bulk carbon contents, possibly due to a leak of the capsule. (d) Integrated intensity of the CO band at 2100 – 2200 $cm^{-1}$ in the infrared spectrum as a function of reduced carbon content for the rhyolite glasses. The regression fit is based on the 1 – 3 GPa data only.*

reduced carbon solubility. Since the CO molecule has a permanent dipole moment, some interaction of the positively charged carbon atom with non-bridging oxygen atoms in the MORB melt may enhance solubility.

The combined effect of chemical interaction and ionic porosity may also produce the low solubility in andesite melt. However, given the analytical uncertainties it is not certain how significant this minimum for andesite is.

While the concentrations of reduced carbon are highest in MORB samples, CO-related infrared bands in the 2100 – 2200 $cm^{-1}$ range were only occasionally observed for these glasses. However, such bands were often seen in the rhyolite glass samples. Fig. 3.4d shows a plot of the integral CO band intensity as a function of reduced carbon content in

the rhyolite samples. Despite the significant uncertainties of the data, there appears to be some correlation between these numbers. The regression fit shown in Fig. 3.4d corresponds to an integral molar extinction coefficient of 966 liter $mol^{-1}$ $cm^{-2}$. This number is more than one order of magnitude lower than the typical extinction coefficients of molecular $CO_2$ or carbonate in silicate glasses. Moreover, detailed inspection of the infrared spectra showed that sometimes the absorption band in the 2100 – 2200 $cm^{-1}$ range is split into several distinct peaks, which are probably due to CO molecules in different chemical environments. Theoretical studies of CO molecules adsorbed on oxide surfaces (e.g. Neyman and Rösch, 1992) suggest that the infrared extinction coefficient of CO may be very sensitive to the chemical environment. Therefore, the scatter of the data in Fig. 3.4d may be due to different CO species with different individual extinction coefficients occurring in the samples in variable proportions. Together with the very low extinction coefficient, the dependence of infrared extinction on the environment of the CO molecule may explain why CO was not detected in the infrared spectrum of many MORB glasses, as the extinction coefficient for MORB glasses may be even lower than that inferred for rhyolite. Consequently, the infrared extinction coefficient given here for rhyolite glasses should not be used to evaluate CO contents in samples with different composition.

In general, the measured concentrations of reduced carbon, which are interpreted to be due to dissolved CO, correlate well with the calculated CO fugacity in the experiments. For MORB and rhyolite, a linear regression fit of the data yielded the following relationships

$$\log c_{CO}^{MORB} = -5.83 + 0.98 \log f_{CO} \quad (R^2 = 0.84)$$
$$\log c_{CO}^{Rhyolite} = -4.52 + 0.65 \log f_{CO} \quad (R^2 = 0.74)$$

where $\log c_{CO}$ is the logarithm of the concentration of reduced carbon (in wt. %) and $\log f_{CO}$ is the logarithm of CO solubility. For andesite, no regression equation is given, since the large scatter of the data at low pressure (≤ 0.5 GPa) introduces considerable uncertainties in the fit parameters.

The solubility of pure CO can be predicted from the equations shown above, although these numbers are of limited significance in nature because they only apply to situations where equilibrium with $CO_2$ by precipitation of graphite through the reaction 2 CO = $CO_2$ + C is not achieved. The equation yields 13 ppm at 100 MPa for MORB. The result can be compared with previous studies by Stanley et al. (2014) and Armstrong et al. (2015), who investigated graphite solubility in silicate melts under reducing conditions at 1 to 3 GPa. Note that their experiments were carried out under vapor-undersaturated conditions, but with controlled oxygen fugacity. The carbon concentrations reported in their studies were generally low (about 1-200 ppm) due to the absence of simultaneous saturation of CO-$CO_2$ gas phase. The regression equation by Armstrong et al. (2015) yields a carbon solubility of 78 ppm at 100 MPa, which is significantly higher than obtained from the present study. However, their system was chemically more complex, including N and H, such that not all reduced carbon detected may be related to CO.

### 3.2.4. *The role of CO in volcanic activity on the Moon*

For the fire-fountain type eruption on the ancient Moon, CO was proposed as the main propellant because the lunar magmas for a long time were believed to be essentially dry and the oxygen fugacities were rather low (Fogel and Rutherford, 1995). Analyses of picritic glasses from the Moon, such as the Apollo 15 green and yellow glasses and the Apollo 17 orange glasses, revealed that the parent magmas contained not only 0.3 – 0.7 ppm of carbon, but also hydrogen equivalent up to 70 ppm of $H_2O$ (Wetzel et al., 2015). In the corresponding melt inclusion, up to 4 ppm of carbon and more than 1000 ppm of $H_2O$ were reported. The compositional trends shown by Wetzel et al. (2015) also suggest that carbon degassed before hydrogen. Under the low oxygen fugacity in these magmas, it is plausible that a significant fraction of the carbon was dissolved as CO. The CO solubilities derived by the present study may be used to estimate the plausible CO partial pressures in equilibrium with the melts. For 0.3 – 0.7 ppm of carbon as observed in the lunar glasses, a CO fugacity of 2.3 – 5.4 MPa is predicted, while 4 ppm of carbon as recorded in melt inclusions yields 31 MPa, which is equivalent to about 7.4 km below the lunar surface. Overall, by combining the CO solubility data with the carbon contents of the lunar glasses, it is suggested that degassing of CO may have played important role in

the initial volatile saturation and bubble nucleation event during the ascent of the magma to the surface.

### *3.2.5. CO in a primordial atmosphere coexisting with a magma ocean*

Carbon is a volatile element which has high a $D^{metal/silicate\ melt}$ partition coefficient and probably preferentially partitioned into the metal phase during the formation of Earth's core (e.g. Dasgupta et al. 2013). On the other hand, the silicate minerals of the mantle may dissolve only trace amounts of carbon (< ~10 ppm; Keppler et al. 2003, Shcheka et al. 2006). Accordingly, one may expect that during the evolution of a magma ocean, carbon may be partially retained in the core and the primordial atmosphere. The redox state of the magma ocean during accretion is initially much lower than the iron-wüstite buffer (e.g. Hirschmann 2012, Rubie et al. 2015), implying that some CO and $CO_2$ was likely reduced to graphite under chemical equilibration of the magma ocean with the atmosphere. Since graphite is specifically lighter than a peridotitic melt, it would have accumulated on the surface of the magma ocean. If a large fraction of total carbon were reduced to graphite, a low $CO/CO_2$ partial pressure would result. In such a situation, the atmosphere becomes richer in CO, which is poorly soluble in silicate melts. This effect may have produced a carbon-poor magma ocean and therefore may have limited the amount of carbon that partitioned into the core. This could also be a plausible mechanism for retaining a significant fraction of total carbon near the surface of the early Earth.

## 3.3. Nitrogen solubility in the deep mantle and the origin of Earth's primordial nitrogen budget.

### *3.3.1. Run products*

To determine nitrogen solubility in transition zone and lower mantle minerals, multi anvil experiments were carried out to crystallize these phases from oxide mixtures or glasses in the presence of a nitrogen-rich fluid phase. All run products contained silicate minerals coexisting with metallic iron and FeO. Fine-grained crystals, which likely precipitated from a fluid during quenching, were often observed. Therefore, the experiments constrain nitrogen solubility in silicate minerals under fluid-saturated and reducing conditions close to the Fe-FeO (iron-wüstite) buffer.

### *3.3.2. Nitrogen solubility in minerals and metal*

The measured nitrogen ($^{15}N$) solubility in wadsleyite and ringwoodite as a function of pressure and temperature is shown in Fig. 3.5. Nitrogen solubility in wadsleyite ranged up to ~250 μg/g (ppm by weight). The data clearly show that pressure and temperature enhance nitrogen solubility in wadsleyite. In a run at 16 GPa and 1500 °C, wadsleyite and olivine coexisted. Measured nitrogen concentrations in wadsleyite and olivine were 188.8 ± 15.6 μg/g and 36.9 ± 12.3 μg/g, respectively, yielding a nitrogen partition coefficient of $D^{wadsleyite/olivine} = 5.1 \pm 2.1$.

Nitrogen solubility in ringwoodite ranged up to 150 μg/g and increased with temperature, whereas pressure had only a minor effect. The large scatter of the data at 1800 °C is likely due to progressive reaction of iron metal and platinum (the capsule material) at high temperature, which changed oxygen fugacity. In a run at 19 GPa and 1400 °C, ringwoodite and wadsleyite coexisted and their nitrogen content was 44.5 ± 7.2 μg/g and 91.5 ± 38.8 μg/g, respectively. Thus, the nitrogen partition coefficient between ringwoodite and wadsleyite is $D^{ringwoodite/wadsleyite} = 0.49 \pm 0.29$.

Since the nitrogen solubility in the transition zone minerals was found to be rather high, the nitrogen dissolution mechanism was investigated by FTIR spectroscopy. The infrared spectra of wadsleyite showed a band at 3176 $cm^{-1}$, which is not observed in other hydrous

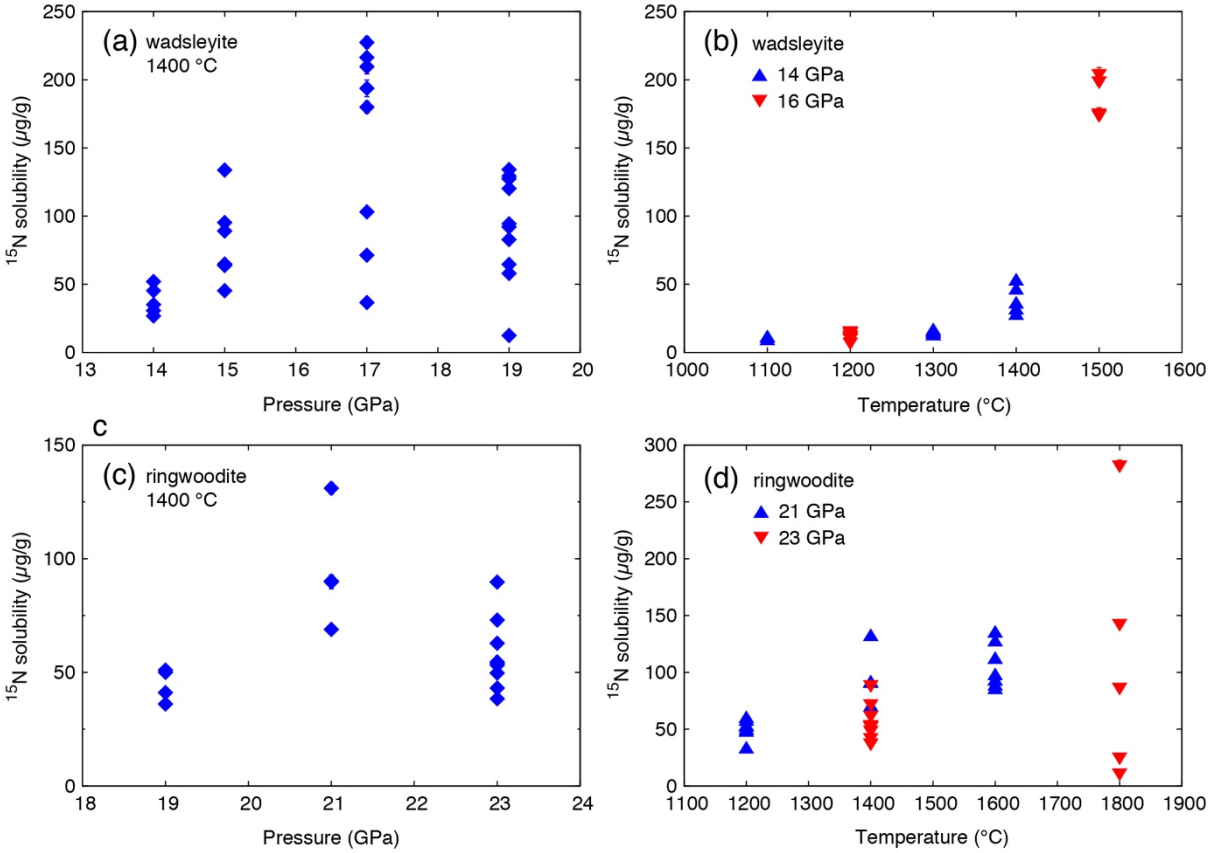


*Fig. 3.5. Nitrogen solubility in (a), (b) wadsleyite and (c), (d) ringwoodite as a function of pressure and temperature.*

wadsleyite samples and may be due to a N-H stretching vibration. Plausible explanation for it may be a substitution of $NH_4^+$ for $Mg^{2+}$ charge balanced by some protonation of oxygen atoms, or a substitution of protonated $N^{3-}$ for $O^{2-}$.

Nitrogen solubility in the lower mantle minerals, bridgmanite and Ca-silicate perovskite synthesized at 24 GPa and 1600 °C was 21.5 ± 18.1 μg/g and 28.3 ± 23.6 μg/g, respectively. The nitrogen concentration in ringwoodite coexisting with bridgmanite was 90.8 ± 37.5 μg/g, yielding a partition coefficient $D^{bridgmanite/ringwoodite}$ = 0.24 +0.30/-0.19. Nitrogen solubility in Fe-rich metal, which coexisted with the silicate minerals, was up to 1.04 wt.% and strongly depended on pressure and temperature. Pressure enhanced nitrogen dissolution, whereas temperature strongly decreased nitrogen solubility.

The nitrogen solubility in olivine (including data from Li et al., 2013), wadsleyite, ringwoodite and Fe-rich metal may be described by the following regression equations:

in olivine, $\ln c_N$ (μg/g) = 2.53 – 1.04 · $10^4$ $T^{-1}$ + 0.246 P - 0.953 ΔNiNiO ($R^2$ = 0.88)

in wadsleyite, $\ln c_N$ (μg/g) = 11.2 – 1.67 · $10^4$ $T^{-1}$ + 0.194 P ($R^2$ = 0.84)

in ringwoodite, $\ln c_N$ (μg/g) = 5.05 – 5.21 · $10^3$ $T^{-1}$ + 0.104 P ($R^2$ = 0.86)

in Fe-rich metal, $\ln c_N$ (wt.%) = - 13.0 + 1.22 · $10^4$ $T^{-1}$ + 0.188 P + 0.871 $x_{Fe}$ ($R^2$ = 0.82)

where $c_N$ is nitrogen solubility of $^{15}N$, T is temperature in Kelvin, P is pressure in GPa, ΔNiNiO is the difference in the logarithm of the oxygen fugacity to the value of the Ni-NiO buffer and $x_{Fe}$ is the molar fraction of iron (Fe/(Fe+Pt)) in the Fe-rich metal. Note that the equations for wadsleyite, ringwoodite, and Fe-metal all refer to conditions close to the Fe-FeO buffer and accordingly, oxygen fugacity is not included in the regression fit.

### *3.3.3. Nitrogen storage capacity of the entire mantle*

From the equations shown above, the nitrogen storage capacity of the entire mantle was calculated (Fig. 3.6). For the model, several assumptions were made. The mantle geotherm was taken from Turcotte and Schubert (2002). The oxygen fugacity of the upper mantle was taken from Frost & McCammon (2008) and that of the transition zone and lower mantle was assumed to be equivalent to the experimental conditions, which are close to the iron-wüstite buffer. In each layer of the mantle, only olivine and pyroxenes (Li et al., 2013) in the upper mantle, wadsleyite and ringwoodite in the transition zone, and bridgmanite, Ca-silicate perovskite and iron metal in the lower mantle were considered as nitrogen hosts. The calculation suggested that the nitrogen ($^{14}N$) storage capacity of the upper mantle, transition zone and lower mantle are 20, 8.0 and 25 times the mass of present atmospheric nitrogen (PAN), respectively. For the upper mantle with a nitrogen capacity of 20 PAN, most of the nitrogen is stored in pyroxenes, whereas olivine may contain only 0.77 PAN. It should be noted that the calculated nitrogen storage capacity is a lower limit, because possible contributions from majorite and ferropericlase and the possible increase of nitrogen solubility with pressure and

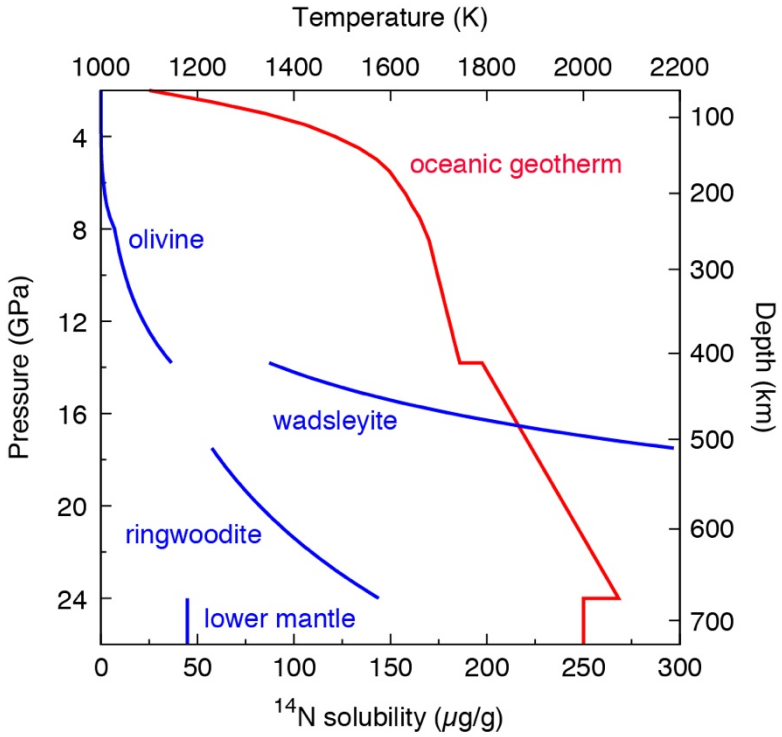


*Fig. 3.6. Nitrogen solubility in major mantle minerals as a function of pressure along an oceanic geotherm. "Lower mantle" is the estimated bulk nitrogen solubility of the lower mantle, including bridgmanite, Ca-perovskite, and iron metal.*

temperature in the lower mantle, which was observed for the other minerals, was not considered.

### *3.3.4. The initial nitrogen budget of the Earth*

The solubility data obtained in this study can be combined with data from previous experimental studies on nitrogen solubility in silicate melts in order to explore the behavior of nitrogen during magma ocean crystallization. Although nitrogen solubility in silicate melts at low to middle pressure was reported by several studies, only Roskosz et al. (2013) provided nitrogen solubility data for melts at high pressure and temperature (5 - 17.5 GPa and 2350 - 2850 °C), which are most relevant for the present study. The nitrogen solubility in peridotitic melts in equilibrium with iron metal was nearly constant at 0.6-0.8 wt.%. By comparing it with data from the present study, the nitrogen partition coefficients between minerals and melts were calculated. The partition coefficient between wadsleyite (189 μg/g $^{15}N$ at 16 GPa and 1500 °C) and melt is $D^{wadsleyite/melt}$ =

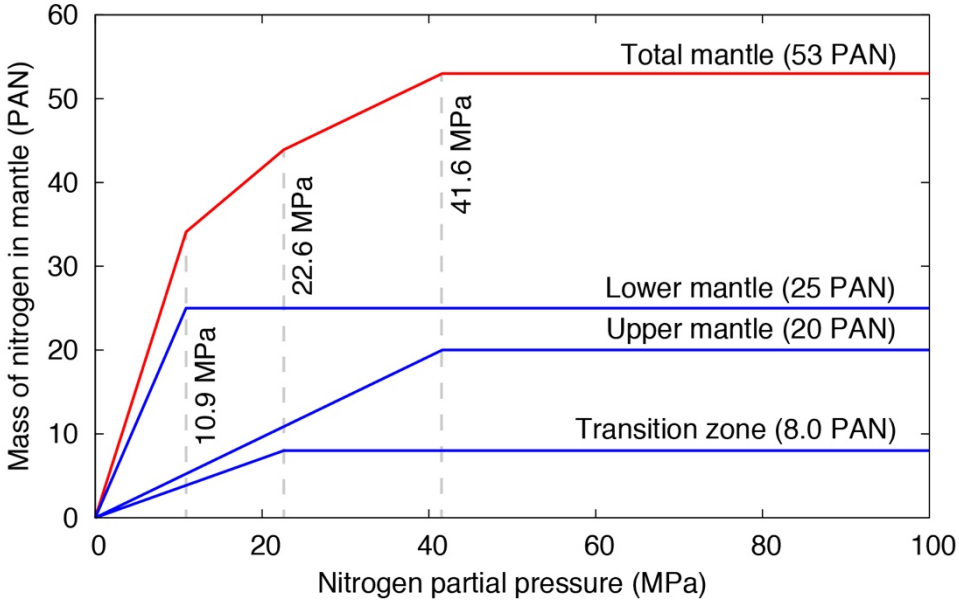


*Fig. 3.7. Mass of nitrogen stored in the mantle as a function of the nitrogen partial pressure of a primordial atmosphere coexisting with the crystallizing magma ocean. PAN = Mass of present atmospheric nitrogen.*

0.023. Similarly, the ringwoodite data (104 µg/g at 21 GPa, 1600 °C) yield $D^{ringwoodite/melt}$ = 0.014. Therefore, the partition coefficient for the bulk transition zone would be $D^{transition\ zone/melt}$ = 0.020. For the lower mantle, $D^{bridgmanite/melt}$ = 0.0029 and $D^{Ca\text{-}perovskite/melt}$ = 0.0038 were obtained, resulting in a bulk partition coefficient for the lower mantle of $D^{lower\ mantle/melt}$ = 0.0030. For the upper mantle, simplified as a 60 % olivine and 40 % pyroxene model, the data from Li et al. (2013) yield $D^{upper\ mantle/melt}$ = 0.0073 at Fe-FeO buffer conditions.

Using the nitrogen solubility data, a model was developed, which predicts the amount of nitrogen stored in the mantle during magma ocean solidification. For the model, it was assumed that the mantle convects and reaches equilibrium with atmospheric nitrogen as long as it is more than 50% molten . After 50% of the mantle is crystalized, convection stops and it behaves as a closed system. After this point, nitrogen dissolved in melts is incorporated into minerals until it reaches gas saturation. The nitrogen solubility in silicate melts close to the Fe-FeO buffer reported by Libourel et al. (2003) is 0.62 µg/g N/MPa. However, this number refers to a hydrogen-free system and Li et al. (2015) showed that nitrogen solubility in silicate melts is one order of magnitude higher at conditions under which $NH_3$ may form. Therefore, we estimated that a plausible value

for nitrogen solubility in silicate melts of the magma ocean is about 6 μg/g N/MPa. Fig. 3.7 shows model results as the mass of nitrogen stored in the mantle (expressed in PAN) as a function of the nitrogen partial pressure of a primordial atmosphere. To evaluate the mass of nitrogen stored in the mantle during solidification, the nitrogen partial pressure of the primordial atmosphere is required. When considering the initial bulk nitrogen abundance on Earth, enstatite chondrites are a primary candidate for the main source of nitrogen on Earth (Li et al., 2016 and references therein). If one assume that Earth's nitrogen source were mostly enstatite chondrites, the bulk Earth contained 605 μg/g of nitrogen. However, loss of light elements during the accretion by impact degassing should be considered. The abundance of C, H, $^{36}Ar$ and $^{84}Kr$ in the present Earth is estimated to be between 1.5 to 5 % of the initial abundance according to enstatite chondritic composition (Marty, 2012). If nitrogen behaved similarly to the other volatile elements, the initial nitrogen partial pressure would be 1.0-3.5 MPa. According to the model shown in Fig 3.7, this corresponds to 3.1-10.9 PAN being initially stored in the mantle.

The bulk nitrogen abundance in the present mantle is usually estimated from $N_2/^{40}Ar$ ratios. The MORB source mantle has a low $N_2/^{40}Ar$ ratios near $10^2$ whereas there is a distinct population of high $N_2/^{40}Ar$ ratios up to $10^4$ among some OIB samples and xenoliths. Therefore, any estimate of nitrogen abundance in the mantle is largely dependent on the size of the reservoirs assigned to "MORB-like" and "high-N" mantle. By assuming that the "high-N" mantle accounts for 3 % of the bulk mantle, Johnson & Goldblatt (2015) obtained an average nitrogen concentration in the mantle of 6 ± 4 μg/g equivalent to 6 ± 4 PAN, which is quite consistent with our prediction derived from modeling the equilibrium between a magma ocean and a primordial atmosphere.

Therefore, it is plausible that Earth is not anomalously depleted in nitrogen but most of the nitrogen may be stored in a deep, poorly sampled reservoir and dynamic exchange of nitrogen between Earth's surface and deep nitrogen reservoirs may have caused fluctuation of Earth's atmosphere over geologic time.

# 4. References


Armstrong, L.S., Hirschmann, M.M., Stanley, B.D., Falksen, E.G. and Jacobsen, S.D., 2015. Speciation and solubility of reduced C–O–H–N volatiles in mafic melt: Implications for volcanism, atmospheric evolution, and deep volatile cycles in the terrestrial planets. Geochim. Cosmochim. Acta 171, 283-302.

Aubaud, C., Pineau, F., Hekinian, R., Javoy, M., 2006. Carbon and hydrogen isotope constraints on degassing of CO2 and H2O in submarine lavas from the Pitcairn hotspot (South Pacific). Geophys. Res. Lett. 33, L02308.

Bell, D.R., Rossman, G.R., 1992. Water in Earth's mantle: The role of nominally anhydrous minerals. Science, 255, 1391-1397.

Biellmann, C., Gillet, P., Guyot, F., Peyronneau, J., Reynard, B., 1993. Experimental evidence for carbonate stability in the Earth's lower mantle. Earth Planet. Sci. Let., 118, 31-41.

Behrens, R.G., 1977. Thermodynamics of transition metal carbonyls I. Fe(CO)5, Ru(CO)5, Os(CO)5. Journal of the Less-Common Metals, 56, 55–68.

Bureau, H., Pineau, F., Metrich, N., Semet, M.P., Javoy, M., 1998. A melt and fluid inclusion study of the gas phase at Piton de la Fournaise volcano (Reunion Island). Chem. Geol. 147, 115–130.

Busigny, V., Cartigny, P., Philippot, P., 2011. Nitrogen isotopes in ophiolitic metagabbros: A re-evaluation of modern nitrogen fluxes in subduction zones and implication for the early earth atmosphere. Geochim. Cosmochim. Acta, 75, 7502–7521.

Dalou, C., Hirschmann, M.M., von der Handt, A., Mosenfelder, J., 2017. Nitrogen and carbon fractionation during core-mantle differentiation at shallow depth. Earth Planet. Sci. Let., 458, 141-151.

Dasgupta, R., Hirschmann, M.M., 2010. The deep carbon cycle and melting in Earth's interior. Earth Planet. Sci. Let., 298, 1-13.

Dixon, J.E., Clague, D.A., Wallace, P., Poreda, R., 1997. Volatiles in alkalic basalts from the north arch volcanic field, Hawaii: extensive degassing of deep submarine-erupted alkalic series lavas. J. Petrol., 38, 911–939.

Fei, H., Wiedenbeck, M., Yamazaki, D., Katsura, T., 2013. Small effect of water on upper-mantle rheology based on silicon self-diffusion coefficients. Nature, 498, 213-216.

Fogel R.A., Rutherford M.J. 1995 Magmatic volatiles in primitive lunar glasses: I. FTIR and EPMA analyses of Apollo 15 green and yellow glasses and revision of the volatile-assisted fire-fountain theory. Geochim. Cosmochim. Acta 59, 201-215.

Frost, D., McCammon, C., 2008. The redox state of Earth's mantle. Annu. Rev. Earth Planet. Sci. 36, 389–420.

Goldblatt, C., Claire, M.W., Lenton, T.M., Mattews, A.J., Watson, A.J., Zahnle, K.J., 2009. Nitrogen-enhanced greenhouse warming on early Earth. Nature Geosc., 2, 891-896.

Isshiki, M., Irifune, T., Hirose, K., Ono, S., Ohishi, Y., Watanuki, T., Nishibori, E., Takata, M., Sakata, M., 2003. Stability of magnesite and its high-pressure form in the lower mantle. Nature, 427, 60-63.

Hirschmann, M.M., 2012. Magma ocean influence on early atmosphere mass and composition. Earth Planet. Sci. Lett. 341-344, 48–57.

Jakobsson, S. and Oskarsson, N., 1994. The system C-O in equilibrium with graphite at high pressure and temperature: An experimental study. Geochim. Cosmochim. Acta 58, 9-17.

Javoy, M., Kaminski, E., Guyot, F., Andrault, D., Sanloup, C., Moreira, M., Labrosse, S., Jambon, A., Agrinier, P., Davaille, A., Jaupart, C., 2010. The chemical composition of the Earth: Enstatite chondrite models. Earth Planet. Sci. Let., 293, 259-268.

Johnson, B., Goldblatt, C., 2015. The nitrogen budget of Earth. Earth-Sci. Rev., 148, 150–173.

Karato, S.I., Paterson, M.S., Fitzgerald, J.D., 1986. Rheology of synthetic olivine aggregates: influence of grain size and water. J. Geophys. Res. 91, 8151–8176.

Kavanagh, L., Goldblatt., C., 2015. Using raindrops to constrain past atmospheric density. Earth Planet. Sci. Lett., 413, 51-58.

Kawakatsu, H., Watada, S., 2007. Seismic evidence for deep-water transportation in the mantle. Science, 316, 1468-1471

Keppler, H., Wiedenbeck, M., Shcheka, S.S., 2003. Carbon solubility in olivine and the mode of carbon storage in the Earth's mantle. Nature, 424, 414–416.

Kerrick, D.M., Connolly, J.A.D., 2001. Metamorphic devolatilization of subducted oceanic metabasalts: implications for seismicity, arc magmatism and volatile recycling. Earth Planet. Sci. Let., 189, 19-29.

Killops, S., Killops, V., 2005. Introduction to Organic Geochemistry, 2nd edition. Blackwell Publishing, Oxford.

Li, Y., Wiedenbeck, M., Shcheka, S., Keppler, H., 2013. Nitrogen solubility in upper mantle minerals. Earth Planet. Sci. Lett. 377, 311–323.

Li, Y., Huang, R., Wiedenbeck, M., Keppler, H., 2015. Nitrogen distribution between aqueous fluids and silicate melts. Earth Planet. Sci. Lett. 411, 218–228.

Li, Y., Marty, B., Shcheka, S., Zimmermann, L., Keppler, H., 2016. Nitrogen isotope fractionation during terrestrial core–mantle separation. Geochem. Perspect. Lett. 2, 138–147.

Libourel, G., Marty, B., Humbert, F., 2003. Nitrogen solubility in basaltic melt, part I: effect of oxygen fugacity. Geochim. Cosmochim. Acta 67, 4123–4135.

Marty, B., 2012. The origins and concentrations of water, carbon, nitrogen and noble gases on Earth. Earth Planet. Sci. Lett., 313, 56–66.

Marty, B., Zimmermann, L., Pujol, M., Burgess, R., Philippot, P., 2013. Nitrogen Isotopic Composition and density of the Archean atmosphere. Science, 342, 101-104.

McSween, H.Y., Jr, Huss, G.,R., 2010. Cosmochemistry. Cambridge University Press, Cambridge.

Mei, S., Kohlstedt, D.L., 2000. Influence of water on plastic deformation of olivine aggregates. 1. Diffusion creep regime. J. Geophys. Res. 105, 21457–21469.

van der Meijde, M., Marone, F., Giardini, D., van der Lee, S., 2003. Seismic evidence for water deep in Earth's upper mantle. Science, 300, 1556-1558.

Miller, S.L., Urey, H.C., 1959. Organic compound synthesis on the primitive Earth. Science, 130 (3370), 245-251.

Mitchell, E.C., Fischer, T.P., Hilton, D.R., Hauri, E.H., Shaw, A.M., Maarten de Moor, J.,Sharp, Z. D., Kazahaya, K., 2010. Nitrogen source and recycling at subduction zones: Insights from the Izu-Bonin-Mariana arc. Geochem. Geophys. Geosys. 11-2.

Molina, J.F., Poli, S., 2000. Carbonate stability and fluid composition in subducted oceanic crust: an experimental study on $H_2O$-$CO_2$-bearing basalts. Earth Planet. Sci. Lett., 176, 295-310.

Neyman, K.M., Rösch, N., 1992. CO bonding and vibrational modes on a perfect MgO (001) surface: LCGTO-LDF model cluster investigation. Chem. Phys., 168, 267–280.

Ni, H., Keppler, H., 2013. Carbon in silicate melts. Rev. Mineral. Geochem. 75, 251-287.

Ozima, M., Podosek, F.A., 2002. Noble Gas Geochemistry. Cambridge University Press, Cambridge.

Pearson, D.G., Brenker, F.E., Nestola, F., McNeill, J., Nasdala, L., Matveev, S., Mather, K., Silversmit, G., Schitz, S., Vekemans, B., Vincze, L., 2014. Hydrous mantle transition zone indicated by ringwoodite included within diamond. Nature, 507, 221-224.

Robie, R.A., Hemingway, B.S., 1995. Thermodynamic Properties of Minerals and Related Substances at 298.15 K and 1 bar (10 Pascals) Pressure and at Higher Temperatures. United States Geological Survey Bulletin 2131.

Rollinson, H., 2007. Early Earth Systems. Blackwell Publishing, Oxford.

Roskosz, M., Bouhifd, M., Jephcoat, A., Marty, B., Mysen, B., 2013. Nitrogen solubility in molten metal and silicate at high pressure and temperature. Geochim. Cosmochim. Acta 121, 15–28.

Rouquette, J., Dolejš, D., Kantor, I. Yu., McCammon, C.A., Frost, D.J., Prakapenka, V.B., Dubrovinsky, L.S., 2008. Iron-carbon iteractions at high temperatures and pressures. Appl. Phys. Lett., 92, 121912.

Rubie, D.C., Jacobson, S.A., Morbidelli, A., O'Brien, D.P., Young, E.D., de Vries, J., Nimmo, F., Palme, H., Frost, D.J., 2015. Accretion and differentiation of terrestrial planet with implications for the compositions of early-formed Solar System bodies and accretion. Icarus, 248, 89-108.

Saal, A.E., Hauri, E.H., Langmuir, C.H., Perfit, M.R., 2002. Vapour undersaturation in primitive mid-ocean-ridge basalt and the volatile content of Earth's upper mantle. Nature, 419, 451–455.

Shcheka, S.S., Wiedenbeck, M., Frost, D. J., Keppler, H., 2006. Carbon solubility in mantle minerals. Earth Planet. Sci. Lett., 245, 730-742.

Stanley, B.D., Hirschmann, M.M., Withers, A.C., 2014. Solubility of C-O-H volatiles in graphite-saturated martian basalts. Geochim. Cosmoch. Acta, 129, 54–76.

Thompson, A.B., 1992. Water in the Earth's upper mantle. Nature, 358, 295-302.

Turcotte, D.L., Schubert, G., 2002. Geodynamics. Cambridge University Press, NewYork.

Wetzel, D.T., Rutherford, M.J., Jacobsen, S.D., Hauri, E.H., Saal, A.E. (2013). Degasing of reduced carbon from planetary basalts. Proc. Nat. Acad. Sci., 110, 8010–8013.

Wetzel, D.T., Hauri, E.H., Saal, A.E., Rutherford, M.J., 2015. Carbon content and degassing history of the lunar volcanic glasses. Nature Geosci. 8, 755-758

Yoder, H.S.Jr., 1976. Generation of basaltic magmas. National Academy of Science, Washington D.C.

# 5. List of manuscripts and statement of the author's contribution

1. **Yoshioka, T., McCammon, C., Shcheka, S., Keppler, H., 2015. The speciation of carbon monoxide in silicate melts and glasses. Am. Mineral. 100, 1641-1644.**
   The research idea was from my supervisor, Prof. Hans Keppler (H.K.). I carried out all the high-pressure experiments with help from Dr. Svyatoslav Shcheka (S.S.). I carried out the Raman spectroscopy and FTIR analyses with help from H.K. Dr. Catherine McCammon carried out and interpreted the Mössbauer analyses. I made thermodynamic calculation with help from H.K. I prepared the figures and tables for the manuscript and H.K. wrote the manuscript.

2. **Yoshioka, T., Nakamura, T., Nakashima, D., Shcheka, S., Keppler, H., 2018. Carbon solubility in silicate melts in equilibrium with a CO-$CO_2$ gas phase and graphite. manuscript for submission to Geochimica et Cosmochimica Acta.**
   The research idea was from H.K. I and S.S. prepared the sample capsules for the IHPV experiments. I carried out all the piston-cylinder experiments. The IHPV experiments were carried out by partly H.K. and partly by myself with help from H.K. I carried out the Raman spectroscopy and FTIR analysis with help from H.K. Prof. Tomoki Nakamura and Dr. Daisuke Nakashima (D.N.) organized the SIMS analysis. D.N., Masakuni Yamanobe and I carried out the SIMS measurements. I calculated the data for the SIMS analyses. Detlef Klaußе (D.K.) made the microprobe analyses. I prepared the figures and tables for the manuscript and partly wrote the draft of the manuscript. H.K. wrote parts of the manuscript and completed it.

3. **Yoshioka, T., Wiedenbeck, M., Shcheka, S., Keppler, H., 2018. Nitrogen solubility in the deep mantle and the origin of Earth's primordial nitrogen budget. Earth Planet. Sci. Lett., 488, 134-143.**
   The research idea was from H.K. I carried out all the multi-anvil experiments with help from S.S. I carried out the Raman spectroscopy and FTIR analyses with help from H.K. I made the microprobe analyses with help from D.K. Dr. Tiziana Boffa-Ballaran carried out and interpreted the X-ray diffraction analyses. Dr. Michael Wiedenbeck,

Frédéric Couffignal and I made the SIMS analyses. I calculated the data from the SIMS analysis. I prepared the figures and tables for the manuscript and partly wrote the draft of the manuscript. H.K. wrote parts of the manuscript and completed it.

# 6. Manuscripts

## 6.1.

## The speciation of carbon monoxide in silicate melts and glasses

Takahiro Yoshioka[1], Catherine McCammon[1], Svyatoslav Shcheka[1] and Hans Keppler[1]*

[1]*Bayerisches Geoinstitut, Universität Bayreuth, 95440 Bayreuth, Germany*

### *6.1.1. Abstract*

We have studied the speciation of carbon monoxide in both Fe-bearing and Fe-free basaltic glasses using Raman, FTIR, and Mössbauer spectroscopy. We show that a band at 2110 $cm^{-1}$ in the Raman spectrum and another band at 2210 $cm^{-1}$ in the FTIR spectrum occur both in the Fe-bearing and Fe-free samples, implying that they cannot be due to any Fe-bearing species. This observation is consistent with $^{57}Fe$ Mössbauer spectra, which do not show any evidence for Fe species with zero isomer shift, as expected for carbonyls. Thermodynamic calculations show that iron carbonyl in basaltic melts under crustal and upper mantle conditions may only be a trace species. Rather than being due to distinct chemical species, the range of vibrational frequencies observed for carbon monoxide in silicate glasses appears to be due to rather subtle interactions of the CO molecule with the matrix. Similar effects are known from the extensive literature on carbon monoxide adsorption on oxides and other surfaces. In the melt at high temperature, there is likely little interaction of the CO molecule with the silicate matrix and solubility may be largely controlled by pressure, temperature, and the overall polymerization or ionic porosity of the melt.

**Keywords:** Silicate melt, carbon monoxide, iron, carbonyl, Raman, Mössbauer

* E-mail: Hans.Keppler@uni-bayreuth.de

### *6.1.2. Introduction*

Carbon dioxide is an important component of volcanic gases, usually second in abundance only to water. Due to its low solubility in silicate melts at low pressure, $CO_2$ may drive bubble nucleation during eruptions and the melting point depression induced by $CO_2$ plays an important role in stabilizing low-degree partial melts in the mantle (e.g. Wyllie and Huang 1976). Accordingly, carbon dioxide solubility in silicate melts has been extensively studied (Ni and Keppler 2013 and references therein). In contrast to $CO_2$, the solubility of carbon monoxide (CO) in silicate melts has received relatively little attention, probably because it is only a trace component in volcanic gases (Symonds et al. 1994) and because thermodynamic calculations suggest that under the oxygen fugacities prevailing in the Earth today, its abundance in crustal and upper mantle fluids is low (e.g. Frost and McCammon 2008). However, carbon monoxide could be an important species of carbon during planetary degasing under reducing conditions, e.g. on the Moon, during core formation on Earth, or perhaps even today in the reduced, deep mantle (e.g. Wetzel et al. 2013; Hirschmann 2013).

Pawley et al. (1992) suggested that carbon monoxide is much less soluble than carbon dioxide in a basaltic melt at 1200 ˚C and 500 to 1500 bar. A similar conclusion was reached by Morizet et al. (2010). Brooker et al. (1999) detected dissolved CO in reduced glasses prepared along the $NaAlO_2$-$SiO_2$ join by FTIR and NMR spectroscopy. In the NMR spectrum, a peak at a chemical shift of 185 ppm was assigned to CO; FTIR spectra showed a band between about 2160 and 2180 $cm^{-1}$, depending on the composition of the glass matrix. Notably, this absorption frequency is significantly higher than for CO in the gas phase (2143 $cm^{-1}$). Wetzel et al. (2013) reported a band at 2110 $cm^{-1}$ in the Raman spectra of reduced, carbon-bearing basalt glasses and attributed it to iron pentacarbonyl $Fe(CO)_5$. They inferred that $Fe(CO)_5$ is the main species of reduced carbon in these glasses. Stanley et al. (2014) suggested that a band at 2205 $cm^{-1}$ in the infrared spectrum in a graphite-saturated basalt could also be due to a carbonyl species.

The stability of carbonyl species in silicate melts and glasses could have important implications for the behavior of carbon, since carbon solubility would then be strongly coupled to the availability of iron. Carbonyls are molecules containing carbon monoxide coordinated to a transition metal. Typical examples are $Ni(CO)_4$ and $Fe(CO)_5$. Stable carbonyls are only known from the central block of the transition metals in the periodic

table, where iron is the only element sufficiently abundant to be relevant for discussing the potential stability of carbonyls in natural silicate melts. The metal atom in simple carbonyls has the formal oxidation state of zero, which is related to an unusual mechanism of chemical bonding (e.g. Greenwood and Earnshaw 1984). An electron pair from the carbon atom is donated to the metal atom to form a σ bond; this bond is strengthened by a back-donation of d electrons from the metal atom into the anti-bonding orbitals of the CO molecule. Populating the anti-bonding orbitals of CO weakens the bond between carbon and oxygen and therefore usually causes the vibrational frequency of CO in a carbonyl to be shifted downwards relative to the free CO molecule.

In this study, we combined Raman, FTIR, and Mössbauer spectroscopy on Fe-bearing and Fe-free basaltic glasses containing reduced carbon in order to investigate the dissolution mechanism of carbon monoxide in silicate melts and glasses.

### *6.1.3. Experimental and analytical methods*

Two different synthetic glasses were used as starting materials. One was equivalent in composition to the lunar green glass used by Wetzel et al. (2013). A second glass had the same composition, with the exception that all FeO (total iron expressed as FeO) was replaced by an equimolar mixture of CaO and MgO. The glasses were prepared from stoichiometric mixtures of high-purity oxides and carbonates. The mixtures were homogenized and first decarbonated by slowly heating them over 12 hours to 1100 ˚C. They were then re-melted for 1 hour at 1600 ˚C and quenched in distilled water. Microprobe analyses of the clear, crystal-free glasses are given in the footnote of Table 6.1. Before the actual high-pressure experiments, the Fe-bearing glass was first wrapped in an iron foil and reduced in a CO-$CO_2$ gas mixture at 1300 ˚C for 3 hours and an oxygen fugacity of one log unit below the iron-wüstite buffer. This is the same oxygen fugacity as expected to prevail in the following piston cylinder experiments in equilibrium with Fe metal and graphite (Wetzel et al. 2013).

High-pressure experiments (Table 6.1) were carried out in an end-loaded piston-cylinder apparatus at 10 kbar and 1450 – 1530 ˚C for 2 hours. Glass powder was loaded into graphite capsules inside platinum rhodium ($Pt_{95}Rh_5$) capsules with 5 mm diameter, 10 mm length and 0.3 mm wall thickness. Only in experiments with the Fe-bearing glass,

some wire of metallic iron was also added to the charge to buffer oxygen fugacity. No water was added in any of the experiments. Some experiments were also carried out with a trace (0.5 wt.%) of $^{57}Fe_2O_3$ added to the Fe-free glass. No iron metal was added in these runs. All experiments were quenched to room temperature within a few seconds by turning off the power to the heater. Run products were usually clear glasses, only in a few runs minor quench crystallization of olivine was observed. No gas bubbles were observed in the glasses and we therefore assume that all volatiles dissolved under run conditions are fully conserved in the glass.

FTIR spectra were measured with a Bruker IRscopeI attached to a Bruker IFS120HR spectrometer. The optics of the spectrometer were kept under vacuum during the measurement, while the microscope was permanently purged with purified air. Measurements were carried out on doubly polished platelets of run product glasses of 248 to 254 µm thickness. For each measurement, 200 scans were accumulated with 4 $cm^{-1}$ resolution, using a tungsten light source, a $CaF_2$ beam splitter and a narrow-band MCT-detector. The spot size was limited to 120 µm by an aperture in the rear focal plane of the 15 X Cassegranian objective.

Raman spectra were measured on the same samples as used for FTIR spectroscopy using a confocal Horiba Jobin-Yvon Labram 800HR UV spectrometer with the 514 nm line of an Ar laser at 200 mW output power as excitation source. Spectra were measured with a 50x objective, a 1800 $mm^{-1}$ grating, and a Peltier-cooled CCD detector, with an optical resolution of 2 $cm^{-1}$ and an accumulation time of 20 times 10 seconds. A reference spectrum of pure $Fe(CO)_5$ (supplied by Sigma-Aldrich) inside a glass cuvette was also measured with the same system, but with an accumulation time of only 2 times 5 seconds and < 10 mW laser power, to avoid evaporating or decomposing the liquid.

Mössbauer spectra were measured at room temperature in transmission mode on a constant acceleration Mössbauer spectrometer with a nominal 370 MBq $^{57}Co$ high specific activity source in a 12 µm thick Rh matrix. The velocity scale was calibrated relative to Fe foil. The dimensionless thickness of the Fe-bearing and the $^{57}Fe_2O_3$-doped sample was 2.9 and 4.9, respectively. Spectra were collected for about 1 day. Spectra were fitted using the xVBF method (e.g., Lagarec and Rancourt 1997) as implemented by MossA software (Prescher et al. 2012).

### *6.1.4. Results and discussion*

**Raman and infrared spectra**

Raman and infrared spectra of both Fe-bearing and Fe-free glasses are shown in Fig. 6.1. The Raman spectra (Fig. 6.1a) of the Fe-bearing glasses show a peak at 2110 $cm^{-1}$, very similar to the peak assigned by Wetzel et al. (2013) to $Fe(CO)_5$. Additional peaks at 1350 $cm^{-1}$ and 1590 $cm^{-1}$ are due to traces of graphite, the band near 3600 $cm^{-1}$ is due to dissolved OH. Methane ($CH_4$, near 2917 $cm^{-1}$) is not detectable. However, essentially the same bands, including the one at 2110 $cm^{-1}$ are also seen in the Raman spectrum of the Fe-free glass. This observation rules out any assignment of this band to a Fe-bearing species. Moreover, while a band near this frequency does indeed occur in the reference spectrum of pure $Fe(CO)_5$ shown in Fig. 6.1b, a strong $Fe(CO)_5$ band near 2014 $cm^{-1}$ (e.g. Bigorgne 1970; Jones et al. 1972) is not seen in the spectra of the CO-bearing glasses.
The infrared spectra (Fig. 6.1c) of the Fe-bearing glasses show a peak near 2210 $cm^{-1}$, that is very similar to a band at 2205 $cm^{-1}$ observed by Stanley et al. (2014), which was tentatively assigned by them to a Fe carbonyl anion. In addition, a band due to dissolved OH occurs near 3500 $cm^{-1}$, corresponding to a water content of about 0.15 wt. %, using the extinction coefficient of Dixon et al. (1988). No clear evidence for carbonate is seen in the infrared spectra. Unlike in the study of Wetzel et al. (2013), no band can be detected near 2110 $cm^{-1}$; however, this band is also very weak in the spectra reported by those authors. The 2210 $cm^{-1}$ band also occurs in the spectrum of the Fe-free glass, again ruling out any assignment to a Fe-bearing species.

**Mössbauer spectra**

Mössbauer spectroscopy should readily allow the identification of any Fe-carbonyl species in a glass, because the formal oxidation state of Fe in carbonyls is zero. This causes the isomer shift of Fe-carbonyl species to be nearly zero (Kalvius et al. 1962; Herber et al. 1963), which is easily distinguishable from the normal isomer shift of $Fe^{2+}$ or $Fe^{3+}$ in glasses (e.g. Virgo and Mysen 1985). Fig. 6.2a shows the Mössbauer spectrum of a graphite-saturated, Fe-bearing glass. Only the normal doublet of $Fe^{2+}$ is seen, with an

*Table 6.1. Synthesis conditions of glasses and a summary of the Raman and infrared bands observed in them.*

| Run no. | Starting material | P (GPa) | T (°C) | Duration (hours) | Crystals§ | FTIR ($cm^{-1}$) | | Raman spectroscopy ($cm^{-1}$) | | | | | | | |
|---|---|---|---|---|---|---|---|---|---|---|---|---|---|---|---|
| | | | | | | 2025 | 2210 | 1350 | 1590 | 1725 | 2110 | 2710 | 2965 | 3075 | 3570 |
| A717 | Fe-bearing glass* | 1 | 1530 | 2 | | | ✔ | ✔ | ✔ | | ✔ | ✔ | | | ✔ |
| B809 | Fe-bearing glass* | 1 | 1450 | 2 | | | ✔ | ✔ | ✔ | | ✔ | | | | ✔ |
| A726 | Fe-free glass** | 1 | 1530 | 2 | | | | ✔ | ✔ | | ✔ | ✔ | | | ✔ |
| A727 | Fe-free glass** | 1 | 1450 | 2 | ✔ | ✔ | ✔ | ✔ | ✔ | | ✔ | ✔ | | | ✔ |
| A732 | Fe-free glass** | 1 | 1530 | 2 | ✔ | | ✔ | ✔ | ✔ | | ✔ | ✔ | | | ✔ |
| A751 | $^{57}$Fe-doped glass# | 1 | 1530 | 2 | | | ✔ | ✔ | ✔ | ✔ | ✔ | ✔ | ✔ | ✔ | ✔ |
| A752 | $^{57}$Fe-doped glass# | 1 | 1530 | 2 | ✔ | | ✔ | ✔ | ✔ | | ✔ | ✔ | ✔ | | ✔ |

** 44.65 wt% $SiO_2$, 8.69 wt% $Al_2O_3$, 23.12 wt% MgO, 8.71 wt% CaO, 14.57 wt% FeO, 0.32 wt% $TiO_2$,.*

*** 48.00 wt% $SiO_2$, 9.78 wt% $Al_2O_3$, 24.44 wt% MgO, 16.50 wt% CaO, 0.37 wt% $TiO_2$.*

*# Fe-free glass doped with 0.5 wt.% of $^{57}Fe_2O_3$*

*§ Small amounts of quench crystals of olivine in some glasses*

*All runs were saturated with graphite (the capsule material); runs A717 and B809 were also in equilibrium with iron metal*

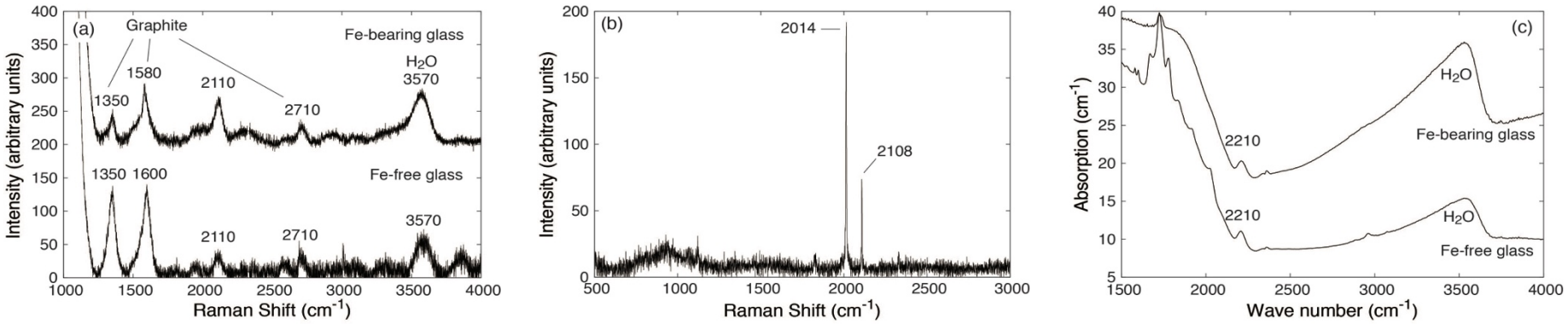


*Fig. 6.1. Raman and infrared spectra of graphite-saturated glasses and of iron pentacarbonyl $Fe(CO)_5$. a) Raman spectra of a Fe-bearing and Fe-free, graphite saturated glass; b) Raman spectrum of pure $Fe(CO)_5$, supplied by Sigma-Aldrich; c) infrared spectra of a Fe-bearing and Fe-free, graphite saturated glass.*

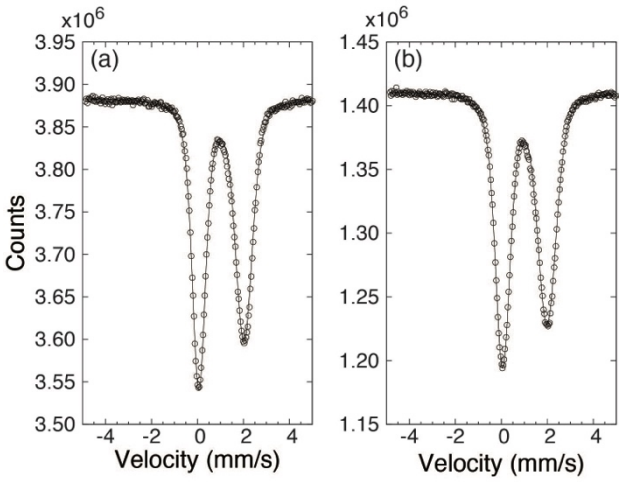


*Fig. 6.2. $^{57}$Fe Mössbauer spectra of two graphite-saturated glasses. a) Glass with 8.69 wt. % FeO, no isotopic enrichment, sample thickness 253 µm; b) glass with 0.5 wt. % $^{57}$FeO, sample thickness 252 µm.*

isomer shift of 1.04 mm/s and a quadrupolar splitting of 1.96 mm/s. However, from these data, one cannot conclude that iron carbonyl species are absent from the sample, since the Fe concentration (8.69 wt.% bulk FeO) is much higher than the concentration of dissolved CO. The latter cannot be directly inferred from spectroscopic data, as the infrared extinction coefficient of CO in glass is not known; however, it is likely that CO concentration is in the order of hundreds to a few thousand ppm for the conditions where the samples were synthesized (e.g. Wetzel et al. 2013; Stanley et al. 2014). Therefore, a glass was prepared with a much lower bulk iron content (0.5 wt. % FeO), where all iron was added as $^{57}Fe_2O_3$. The Raman and infrared spectra of this glass showed the same bands at 2110 and 2210 $cm^{-1}$ as the glass with higher Fe content. The Mössbauer spectrum (Fig. 6.2b) is also virtually indistinguishable from the spectrum of the Fe-rich glass. If iron carbonyls were major CO species in this sample, they should represent a considerable fraction of the total iron, and therefore an enhancement of absorption near zero isomer shift should be seen. This is not observed.

**Thermodynamic considerations**

The thermodynamic properties of iron pentacarbonyl are known from a combination of calorimetric and spectroscopic data (Behrens 1977). By combining them with standard

state thermodynamic data for carbon monoxide and iron metal (Robie and Hemingway 1995), the equilibrium constant $K$ for the reaction

$$Fe + 5\ CO = Fe(CO)_5$$

can readily be calculated. This yields $\ln K = -66.71 + 20363/T$, where $T$ is temperature in Kelvin. The equilibrium constant is defined as

$$K = \frac{f_{Fe(CO)_5}}{a_{Fe} f_{CO}^5}$$

where $f$ are fugacities and $a_{Fe}$ is the activity of iron. Assuming equilibrium with metallic iron – as in some of our experiments – $a_{Fe}$ becomes 1 and the fugacity of the pentacarbonyl can easily be calculated for a given CO fugacity. The results of these calculations are shown in Fig. 6.3. For all plausible conditions of temperature and CO fugacity in the crust and upper mantle, the ratio of the pentacarbonyl fugacity to the CO fugacity is very low, implying that $Fe(CO)_5$ may only be a trace species in a gas phase at run conditions. The ratio of $Fe(CO)_5$ to CO in a coexisting silicate melt could potentially be higher, due to preferential partitioning of $Fe(CO)_5$ into the melt. However, the fugacity ratios in the gas phase are so unfavorable for the formation of $Fe(CO)_5$ that this effect is unlikely to stabilize significant amount of iron carbonyl in the melt. The high volatility of $Fe(CO)_5$ (boiling point of 103 ˚C at 1 bar) also makes preferential partitioning into a silicate melt in equilibrium with a gas phase unlikely. For conditions where the melt is

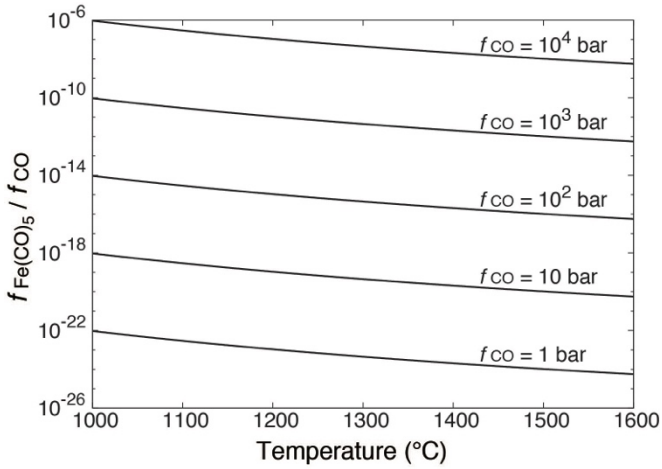


*Fig. 6.3. Calculated ratio of the fugacity of $Fe(CO)_5$ to the fugacity of CO for various temperatures and CO fugacities.*

not in equilibrium with metallic iron, $Fe(CO)_5$ abundances will be even lower. For more complicated (polynuclear) Fe carbonyl species, thermodynamic data are lacking; however, the main reason for the low stability of $Fe(CO)_5$ at high temperatures is the strongly negative entropy of formation from Fe and CO ($\Delta S^\circ$ = - 574.3 J/mol K for $Fe(CO)_5$ gas). For larger, more complicated Fe carbonyl species, this number will be even more negative, making their stability at high temperatures very unlikely.

**A comparison with carbon monoxide adsorbed on surfaces**

The bands in the 2100 $cm^{-1}$ to 2200 $cm^{-1}$ range observed here and in previous studies (Brooker et al. 1999; Wetzel et al. 2013; Stanley et al. 2014) are very likely due to some kind of CO dissolved in the glass, as they occur in a frequency range where normally only triple-bonded light elements are observed. Vibrational frequencies of acetylene HCCH, hydrogen cyanide HCN, and derived species may occur in a similar range. However, the C-H bands of acetylene are not observed and our samples do not contain measurable nitrogen, so assigning these bands to carbon monoxide is the only plausible possibility. This would imply that the vibrational frequencies of CO in glasses are much more strongly affected by the glass matrix than those of $CO_2$. For molecular carbon dioxide in glasses, the infrared spectra always show a band very close to the antisymmetric stretching frequency of the free $CO_2$ molecule (2349 $cm^{-1}$; Ni and Keppler 2013). The stronger interaction of CO with the silicate matrix may be related to the fact that CO has a permanent dipole moment, which $CO_2$ does not have. Moreover, the CO has antibonding molecular orbitals at relatively low energy (e.g. Greenwood and Earnshaw 1984), so that it can accept electron density, which reduces the bond strength and therefore the stretching frequency.

Some insights into possible interactions between the CO molecule with the glass matrix may be gained from the extensive literature on CO adsorption on surfaces. While the chemical bonding of CO on a surface may not be exactly the same as the interaction of the CO molecule with a surrounding glass matrix, the data provide a useful guide for understanding the relationship between chemical bonding and vibrational frequencies. Raman frequency shifts for CO adsorbed on surfaces have been reported, which are even

larger than the shifts observed in glasses. Interestingly, both shifts to higher and to lower frequencies are observed and they also occur in systems without transition metals and systems where carbonyls are not stable. Bordiga et al. (1995) observed that the stretching frequency of CO adsorbed on a zeolite (mordenite) shifts from 2155 $cm^{-1}$ to 2188 $cm^{-1}$, depending on the alkali ion present. Similar shifts were observed for the adsorption on a titanosilicate (Zecchina et al. 1999). Several theoretical studies have investigated the adsorption of CO on the surface of MgO crystals (Neymann and Rösch 1992, 1993; Pacchioni et al. 1992). Interestingly, these models predict an increase of the CO stretching frequency, if the carbon atom docks to the surface, while a decrease in frequency is predicted, if CO is coordinated to the surface by the oxygen atom. Predicted frequency shifts range from – 124 $cm^{-1}$ to + 99 $cm^{-1}$ relative to the stretching frequency of the free CO molecule. The effect is mainly attributed to electrostatic fields acting on the CO dipole, rather than to direct chemical bonding to the surface. Adsorption experiments on silver surfaces also show some interesting effects. Note that no stable silver carbonyls are known and silver, being a noble metal, is not expected to easily form chemical bonds. Yamamoto and Nanba (1988) observed that they could reduce the stretching frequency of CO adsorbed on a silver film by 29 or 23 $cm^{-1}$, respectively, by co-adsorbing xenon and krypton. Mahoney et al. (1984) reported that they could induce large shifts in the stretching frequency of CO adsorbed on a silver electrode simply by changing the chemical potential on the electrode. This effect, sometimes called “Stark tuning” has also been observed for other electrode materials (Zhou and Weaver 1996). All of these observations suggest that the CO stretching frequency is extremely sensitive to very subtle changes in the environment of the molecule.

### *6.1.5. Implications*

The experimental data presented here imply that bands observed in the 2100 – 2200 $cm^{-1}$ range of the Raman and infrared spectra of reduced, carbon-bearing glasses are not due to several, distinct chemical species, but caused by CO molecules weakly interacting with the matrix. This conclusion is consistent with the extensive literature on CO adsorbed on surfaces. In silicate melt at high temperature, these weak interactions are small compared to thermal energy and therefore, the CO molecule probably dissolves in

the melt with little interaction with the matrix. CO solubility is therefore likely a simple function of pressure, temperature and the bulk structure of the silicate melt, as expressed by the degree of polymerization or ionic porosity. However, theoretical studies of surface adsorbed CO suggest that CO molecules with different stretching frequencies may have very different infrared absorption coefficients (Neyman and Rösch, 1992), which may require matrix-specific calibrations for measuring CO in silicate glasses by infrared spectroscopy.

### *6.1.6. Acknowledgments*

Constructive reviews by Jim Webster, Alexander Borisov, Fabrice Gaillard, and Ian Swainson helped to improve the manuscript.

### *6.1.7. References cited*

Behrens, R.G. (1977) Thermodynamics of transition metal carbonyls I. $Fe(CO)_5$, $Ru(CO)_5$, $Os(CO)_5$. Journal of the Less-common Metals, 56, 55-68.

Bigorgne, M. (1970) Étude spectroscopique Raman et infrarouge de $Fe(CO)_5$, $Fe(CO)_4L$ et trans-$Fe(CO)_3L_2$ (L=$PMe_3$, $AsMe_3$, $SbMe_3$). I. Attribution des bandes de $Fe(CO)_5$. Journal of Organometallic Chemistry, 24, 211-229.

Bordiga, S., Lamberti, C., Geobaldo, F., and Zecchina, A. (1995) Fourier-transform infrared study of CO adsorbed at 77 K on H-Mordenite and alkali-metal exchanged mordenites. Langmuir, 11, 527-533

Brooker, R.A., Kohn, S.C., Holloway, J.R., McMillan, P.F., and Carroll, M.R. (1999) Solubility, speciation and dissolution mechanism for $CO_2$ in melts on the $NaAlO_2$-$SiO_2$ join. Geochimica et Cosmochimica Acta, 63, 3549-3565.

Dixon, J.E., Stolper, E.M., and Delaney, J.R. (1988) Infrared spectroscopic measurements of $CO_2$ and $H_2O$ in Juan de Fuca Ridge basaltic glasses. Earth and Planetary Science Letters, 90, 87-104.

Frost, D.J., and McCammon, C.A. (2008) The redox state of Earth´s mantle. Annual Review of Earth and Planetary Sciences, 36, 389-420.

Greenwood, N.N., and Earnshaw, A. (1984) Chemistry of the Elements. Pergamon Press.

Herber, R.H., Kingston, W.R., and Wertheim, G.K. (1963) Mossbauer effect in iron pentacarbonyl and related carbonyls. Inorganic Chemistry, 2, 153-158.

Hirschmann, M.M. (2013) Fe-carbonyl is a key player in planetary magmas. Proceedings of the National Academy of Sciences of the United States of America, 110, 7967-7968.

Jones, L.H., McDowell, R.S., Goldblatt, M., and Swanson, B.I. (1972) Potential constants of iron pentacarbonyl from vibrational spectra of isotopic species. The Journal of Chemical Physics, 57, 2050-2064.

Kalvius, M., Zahn, U., Kienle, P., and Eichner, H. (1962) Hyperfeinstruktur des 14,5 keV-Zustandes von $Fe^{57}$, gebunden in verschiedenen Eisencarbonylen. Zeitschrift für Naturforschung, A 17, 494-499.

Lagarec, K., and Rancourt, D.G. (1997) Extended Voigt-based analytic lineshape method for determining N-dimensional correlated hyperfine parameter distributions in Mössbauer spectroscopy. Nuclear Instruments and Methods in Physics Research, B 129, 266-280

Mahoney, M.R., Howard, M.W., and Cooney, R.P. (1984) Raman spectra of carbon monoxide adsorbed on silver electrodes. Journal of Electroanalytical Chemistry, 161, 163-167.

Morizet, Y., Paris, M., Gaillard, F., and Scaillet, B. (2010) C-O-H fluid solubility in haplobasalt under reducing conditions: An experimental study. Chemical Geology, 279, 1-16.

Neyman, K.M., and Rösch, N. (1992) CO bonding and vibrational modes on a perfect MgO (001) surface: LCGTO-LDF model cluster investigation. Chemical Physics, 168, 267-280.

Neyman, K.M., and Rösch, N. (1993) Bonding and vibration of CO molecules adsorbed on low-coordinated sites on MgO: a LCGTO-LDF cluster investigation. Surface Science, 297, 223-234.

Ni, H., and Keppler, H. (2013) Carbon in silicate melts. Reviews in Mineralogy and Geochemistry, 75, 251-287.

Pacchioni, G., and Cogliandro, G. (1992) Molecular orbital cluster model study of bonding and vibrations of CO adsorbed on MgO surface. International Journal of Quantum Chemistry, 42, 1115-1139.

Pawley, A.R., Holloway, J.R., and McMillan, P.F. (1992) The effect of oxygen fugacity on the solubility of carbon oxygen fluids in basaltic melt. Earth and Planetary Science Letters, 110, 213-225.

Prescher, C., McCammon, C., and Dubrovinsky, L. (2012) MossA - a program for analyzing energy-domain Mossbauer spectra from conventional and synchrotron sources. Journal of Applied Crystallography, 45, 329-331

Robie, R.A., and Hemingway, B.S. (1995) Thermodynamic Properties of Minerals and Related Substances at 298.15 K and 1 bar ($10^5$ Pascals) Pressure and at Higher Temperatures. United States Geological Survey Bulletin 2131.

Stanley, B.D., Hirschmann, M.M., and Withers, A.C. (2014) Solubility of C-O-H volatiles in graphite-saturated martian basalts. Geochimica et Cosmochimica Acta, 129, 54-76.

Symonds, R.B., Rose, W.I., Bluth, G.J.S., and Gerlach, T.M. (1994) Volcanic-gas studies: Methods, results, and applications. Reviews in Mineralogy, 30, 1-66.

Virgo, D., and Mysen, B.O. (1985) The structural state of iron in oxidized vs. reduced glasses at 1 atm: A $^{57}$Fe Mössbauer study. Physics and Chemistry of Minerals, 12, 65-76.

Wetzel, D.T., Rutherford, M.J., Jacobsen, S.D., Hauri, E.H., and Saal, A.E. (2013) Degasing of reduced carbon from planetary basalts. Proceedings of the National Academy of Sciences of the United States of America, 110, 8010-8013.

Wyllie, P.J., and Huang, W.L. (1976) Carbonation and melting reactions in system CaO-MgO-$SiO_2$-$CO_2$ at mantle pressures with geophysical and petrological applications. Contributions to Mineralogy and Petrology, 54, 79-107.

Yamamoto, I., and Nanba, T. (1988) Change in the stretching frequency of a CO molecule absorbed on a silver film induced by coadsorption. Surface Science, 202, 377-387.

Zecchina, A., Otero Areán, C., Turnes Palomona, G., Geobaldo, F., Lamberti, C., Spoto, G., and Bordiga, S. (1999) The vibrational spectroscopy of $H_2$, $N_2$, CO and NO adsorbed on

the titanosilicate molecular sieve ETS-10. Physical Chemistry Chemical Physics, 1, 1649-1657.

Zhou, S., and Weaver, M.J. (1996) Potential dependent metal-adsorbate stretching frequencies for carbon monoxide on transition metal electrodes: Chemical bonding versus electrostatic field effects. Journal of Physical Chemistry, 100, 4237-4242

Manuscript received January 29, 2015
Manuscript accepted March 21, 2015
Manuscript handled by Ian Swainson

## 6.2.

# Carbon solubility in silicate melts in equilibrium with a CO-$CO_2$ gas phase and graphite

Takahiro Yoshioka[1], Tomoki Nakamura[2], Daisuke Nakashima[2], Svyatoslav Shcheka[1], Hans Keppler[1*]

[1]Bayerisches Geoinstitut, Universität Bayreuth, 95440 Bayreuth, Germany
[2]Tohoku University, Sendai, Japan

## *6.2.1 Abstract*

The solubility of carbon in silicate melts (Fe-free MORB basalt, Fe-free andesite and Fe-free rhyolite) coexisting with graphite and a CO-$CO_2$ fluid phase was measured to 3 GPa and 1500˚C. Experiments in the 0.2 – 0.5 GPa range were carried out in an internally heated pressure vessel equipped with a rapid-quench device. In these experiments, glass powder and pure CO gas were directly loaded into platinum capsules; during the runs, graphite precipitated, indicating that the equilibrium 2 CO = C + $CO_2$ in the gas phase was reached. Experiments at higher pressures were carried out in a piston cylinder apparatus, starting with glass powder, graphite, and $Ag_2C_2O_4$ as a source of $CO_2$. Carbon contents in quenched glasses were measured by secondary ion mass spectrometry (SIMS). Carbon was found to be homogeneously distributed throughout the samples, implying attainment of equilibrium with the gas phase. Experiments with the internally heated gas pressure vessel and the piston cylinder apparatus gave very consistent results. Bulk carbon solubility is directly proportional to pressure and follows Henry´s law with good approximation. The effect of temperature on solubility is small. Henry coefficients of bulk carbon solubility obtained by fitting all data were 2.15 ppm C/MPa for MORB, 1.57 ppm C/MPa for andesite and 2.14 ppm C/MPa for rhyolite. In almost all samples, bulk carbon contents were higher than the content of oxidized carbon ($CO_2$ and carbonate). The difference is interpreted to

* hans.keppler@uni-bayreuth.de

be due to dissolved CO, consistent with bands in the 2100 – 2200 $cm^{-1}$ range of the infrared and Raman spectra. For MORB, the solubility $c_{CO}$ of CO (expressed as wt. % carbon) may be described by the relationship $\log c_{CO}^{MORB} = -5.83 + 0.98 \log f_{CO}$ ($R^2 = 0.84$), where $f_{CO}$ is CO fugacity, while the rhyolite data are best described by $\log c_{CO}^{Rhyolite} = -4.52 + 0.65 \log f_{CO}$ ($R^2 = 0.74$). Our data imply that the solubility of carbon in silicate melts depends very strongly on whether or not graphite saturation in the gas phase is reached. If the equilibrium $2\ CO = C + CO_2$ is attained through graphite precipitation, bulk carbon solubility will be close to the solubility of $CO_2$ over a wide pressure and temperature range, since the gas phase consists mostly of $CO_2$. Only at low pressures of a few 100 MPa or below, the fraction of CO in the gas phase becomes so large that bulk carbon solubility is significantly reduced compared to $CO_2$. Low carbon solubilities may also be observed in situations where graphite precipitation is kinetically inhibited. This could have been the case in the source region of lunar fire fountain eruptions, where dissolved CO may have caused vapor saturation up to 7 km below the lunar surface. We argue that in a Hadean magma ocean on Earth, the primordial atmosphere was almost certainly in equilibrium with graphite floating on the surface. Extensive graphite precipitation and a low atmospheric pressure on the surface could have stabilized a CO-rich atmosphere that may have limited carbon sequestration in the core. While under vapor-saturated conditions, CO in silicate melt is a subordinate species as compared to $CO_2$ or carbonate, CO is expected to be the dominant species of dissolved carbon at oxygen fugacities about 2 log units below the CCO buffer. We suggest that this dissolved CO may be easily overlooked, because the infrared extinction coefficient for CO (about 966 liter $mol^{-1}$ $cm^{-2}$ in rhyolite glass) is more than one order of magnitude lower than that of $CO_2$ or carbonate and in addition, this extinction coefficient may be strongly matrix dependent.

### *6.2.2. Introduction*

Carbon dioxide ($CO_2$) is an important component of volcanic gases, usually second in abundance only to water vapor. In contrast to this, carbon monoxide (CO) is only a minor or trace component in volcanic gases on Earth today, with a

maximum abundance of 1 – 2 mol % in gases from some reduced magmas sourced in the deep mantle (e.g. Kilauea, Mt. Erebus; Symonds et al. 1994, Oppenheimer and Kyle 2008). However, the redox state of the mantle has evolved over time. Earth´s accretion likely started at redox conditions far below the iron wüstite buffer (Rubie et al. 2015), such that an early magma ocean may have been in equilibrium with a rather reduced atmosphere, where a significant fraction of carbon may have been present as CO. The equilibrium between this magma ocean and a primitive atmosphere may have had a strong influence on the incorporation of volatiles in the growing planet (Hirschmann 2012). While Earth´s upper mantle likely became oxidized in the Archean or perhaps even earlier (Trail et al. 2011), the mantle of other terrestrial planets and of the Moon may have remained in a highly reducing state, such that CO may have played a significant role in carbon degassing and in driving volcanic activity (e.g. Rutherford et al. 2017). Indeed, it has been suggested that CO degasing may have driven lunar fire-fountain eruptions (e.g. Fogel and Rutherford 1995, Wetzel et al. 2015). Accordingly, there has recently been a strong interest in understanding the solubility of carbon species in silicate melt under reducing conditions. Most of these studies (e.g. Stanley et al. 2014, Armstrong et al. 2015, Yoshioka et al. 2015) have, however, been carried out a relatively high pressures and at conditions where a free fluid phase likely did not coexist with the silicate melt, such that they cannot directly be applied to model near-surface volcanic degasing or the equilibrium between a magma ocean and a primordial atmosphere.

While methane ($CH_4$) may be an important constituent of fluids in the deep, reduced mantle (e.g. Frost and McCammon 2008), it is unlikely to be an important species of carbon during volcanic degassing or in low-pressure silicate melt – gas equilibria. Methane has a distinctly positive free energy of formation at 1 bar and magmatic temperatures, such that it nearly completely decomposes to graphite and $H_2$. Stabilization of magmatic methane would require high partial pressures of hydrogen ($H_2$) that are implausible for the surface of terrestrial planets. Accordingly, CO is likely the only important species of reduced carbon that needs to be considered (in addition to $CO_2$) when modeling carbon degasing from reduced magmas. Available data on the solubility and speciation of CO in silicate

melts are, however, rather limited and sometimes contradictory. Brooker et al. (1999) detected dissolved CO in the $^{13}C$ NMR spectra of reduced silicate glasses. While some studies considered CO solubility to insignificantly small (Pawley et al. 1992, Morizet et al. 2010), other studies implied an important contribution of reduced carbon to overall carbon solubility (e.g. Stanley et al. 2014, Armstrong et al. 2015). Carbonyls were proposed to be the main species of CO dissolved in silicate melts (Wetzel et al. 2013), while more recent studies support the notion that probably physically dissolved CO molecules dominate CO speciation in silicate melts (Yoshioka et al. 2015).

Pure CO gas rapidly attains equilibrium with $CO_2$ by precipitating graphite at high temperature, according to the reaction

(1) $$2\ CO = C + CO_2$$

Indeed, as we will show below, even in experiments where all carbon was loaded as CO gas into capsules, precipitation of graphite was observed already after a few hours at magmatic temperatures. It is therefore rather likely that under most circumstances where a gas phase rich in CO coexists with silicate melts in nature, it is also in equilibrium with graphite, such that the composition of the coexisting gas phase is controlled by the graphite-CO-$CO_2$ equilibrium. Accordingly, it is impossible – and in most cases not directly relevant for nature - to experimentally study the solubility of pure CO gas in a silicate melt. Rather, the most simple experiment that may be done is to quantify the solubility of carbon in a silicate melt in equilibrium with graphite and a CO-$CO_2$ gas phase. Systematic experiments of this type, covering a wide range of pressure, temperature and melt compositions are reported for the first time in the present study. Note that the actual composition of the CO-$CO_2$ gas phase coexisting with graphite changes significantly with pressure and temperature; high temperatures shift equilibrium (1) to the left hand side, while an increase in pressure will shift it to the right.

An important observation is that the equilibrium (1) between a CO-$CO_2$ gas mixture and graphite buffers oxygen fugacity ("CCO buffer", French and Eugster

1965, Frost and Wood 1997). This is already obvious from the phase rule, which implies that in a system with two components (C and O), the coexistence of two phases (gas and solid graphite) implies that there are only two degrees of freedom. Therefore, if pressure and temperature are fixed, all intensive variables, including gas phase composition and oxygen fugacity have to be fixed and are functions of pressure and temperature only. If one imposes an oxygen different from that dictated by the gas graphite equilibrium onto this system, one of the phases (graphite or gas) has to disappear according to the phase rule. At oxygen fugacities higher than the CCO buffer, graphite is not stable anymore; at lower oxygen fugacities, the gas phase disappears.

In the present study, we have investigated the solubility of carbon in silicate melts coexisting with both graphite and a CO-$CO_2$ gas phase from 0.2 to 3 GPa and from 1200 ˚C to 1500 ˚C. We investigated melts ranging from rhyolite over andesite to basalt (MORB). In order to avoid complications due to redox reactions between carbon species and $Fe^{2+}$ or $Fe^{3+}$ in the melt, we always used simplified Fe-free model compositions. While this may seem as a severe limitation, Yoshioka et al. (2015) showed that there is no discernible difference in CO speciation between Fe-bearing and Fe-free synthetic basalt melts.

### *6.2.3. Experimental and analytical methods*

**Starting materials**

Synthetic glasses with three different compositions were used as starting materials. They were prepared according to the compositions of average MORB (Albarede 2005), average andesite (Cox et al. 1979), and average rhyolite (Cox et al. 1979). For the synthetic glasses, all FeO was replaced by an equimolar amount of a 1:1 (molar) mixture of CaO and MgO. Stoichiometric mixtures of analytical grade $SiO_2$, $TiO_2$, $Al(OH)_3$, $Mg(OH)_2$, $CaCO_3$, $Na_2CO_3$ and $K_2CO_3$ were prepared for each composition. The mixtures were homogenized with a mortar under ethanol for 1 hour and then dried for one night in an oven at 140 °C. The mixtures were

decarbonated in a platinum crucible by slowly heating to 1100 °C over 12 hours and sintering at this temperature for 6 hours. The sintered charges were then melted at 1600 °C in a high-temperature furnace for 1 hour and quenched in deionized water. Run products were clear, crystal-free glasses.

Densities of the starting MORB and andesite glasses (Table 6.1) were measured with a pycnometer using pieces of bubble-free glass and distilled water. The density of the rhyolite glass was not measurable because it contained numerous bubbles. Therefore, its density was taken from a glass of similar composition as given in Nowak et al. (2003). A JEOL JXA-8200 electron microprobe was used to quantify the major element composition of the starting glasses. Measurements were carried out with a 15 kV acceleration voltage and a 15 nA beam current. The counting time was 20 s on peak and 10 s on background. 10 points were measured for every glass. Standards used were andradite for Si and Ca, $MnTiO_3$ for Ti, spinel for Al, Fe metal for Fe, enstatite for Mg, albite for Na and orthoclase for K. Compositions of the starting glasses according to electron microprobe analyses are given in Table 6.1.

*Table 6.1. Composition of starting materials*

| | MORB 1 | MORB 2 | Andesite | Rhyolite |
|---|---|---|---|---|
| $SiO_2$ | 51.38 | 52.25 | 57.87 | 70.88 |
| $Na_2O$ | 3.29 | 3.23 | 4.00 | 4.21 |
| $K_2O$ | 0.05 | 0.01 | 1.74 | 4.75 |
| $TiO_2$ | 1.81 | 1.80 | 0.91 | 0.24 |
| FeO | 0.02 | 0.02 | 0.02 | 0.02 |
| MgO | 11.50 | 11.70 | 5.68 | 1.21 |
| $Al_2O_3$ | 15.20 | 15.06 | 18.35 | 14.81 |
| CaO | 15.54 | 14.88 | 9.88 | 2.58 |
| Total | 98.80 | 98.95 | 98.44 | 98.70 |
| density (g/liter) | 2726 | - | 2537 | 2312 |

*MORB 1 and MORB 2 are two different batches of the same starting material. The density of the rhyolite glass was not measured, because the sample contained bubbles. The density given is for a glass with similar composition from Nowak et al. (2003).*

**Experiments in the internally heated gas pressure vessel**

Experiments at 0.2-0.5 GPa and 1200-1400 °C were carried out with an internally heated pressure vessel (IHPV). A 150 000 psi Harwood autoclave with an inverted Bridgman seal was used with argon as a pressure medium. Pressure was measured by a manganin cell. Samples were heated by a vertical, two-zone molybdenum heater. Temperature was measured by two type S thermocouples, which were placed 15 mm apart from each other above and below the sample. During an experiment, the power on the two heaters was adjusted such that the gradient along the length of the sample was less than 2 ˚C. Run durations ranged between 2 and 6 hours. Samples were suspended on a thin (100 µm thick) Pt wire. For quenching, this wire was fused by a short voltage pulse, such that the sample dropped into a cold zone of the autoclave within 1 – 2 s. Capsules were prepared by directly loading glass powder and carbon monoxide gas into platinum tubes of 3.5 mm outer diameter and 0.3 mm wall thickness with a welded 0.3 mm thick bottom. A gas-loading device similar to that described by Boettcher et al. (1989) was used. After carbon monoxide gas of about 80 bar was loaded, the upper part of the platinum tube was compressed by a vise and sealed by welding. The capsule always expanded after release from the vise after welding, due to the high pressure of carbon monoxide gas inside. The final length of the capsule was typically 12-15 mm.

**Piston cylinder experiments**

Experiments at 1-3 GPa and 1400-1600 °C were carried out with an end-loaded piston-cylinder apparatus. The assembly consisted of a 1/2 inch outer diameter talc sleeve, a pyrex sleeve, a tapered graphite heater and a crushable $Al_2O_3$ inner sleeve. Crushable $Al_2O_3$ spacers were placed below and above the platinum capsule containing the sample and $Al_2O_3$ powder was used to fill the gap. Temperatures were measured by type D thermocouples almost touching the sample. A 18 % friction correction was applied to the nominal pressures. Runs were started with the hot-piston-in procedure and usually lasted for 6 hours. All

experiments were rapidly quenched to room temperature by turning off the power of the heater, which caused the sample to cool close to room temperature within 20 – 30 s. Samples were sealed by arc-welding into capsules made of a $Pt_{95}Rh_5$ tube with 5 mm outer diameter, 10 mm length and 0.3 mm wall thickness. The tube was closed by two 0.3 mm thick lids at the both ends. As starting materials, silver oxalate $Ag_2C_2O_4$, graphite powder, glass powder and a piece of gold foil were filled into the capsule in the given sequence from bottom to top. Upon heating, $Ag_2C_2O_4$ decomposes instantaneously to silver metal and carbon dioxide. The equilibrium composition of the fluid phase is then achieved through the reaction of $CO_2$ with graphite. Gold foil was added to produce clear glasses by absorbing silver metal particles. During the experiment, the gold melts and the droplets of gold sinking through the silicate melt absorb the silver.

**Investigation of run products**

After the IHPV experiments, the recovered capsules were weighed to check for leaks and then pierced with a needle. Upon piercing, a hissing sound of gas flow and significant weight loss was always observed, indicating gas saturation and the absence of leaks. Capsules from piston cylinder experiments always had some $Al_2O_3$ adhering on the surface, such that checking for leaks by weighing was not possible. However, fluid inclusions in the quenched glasses usually demonstrated the existence of an excess gas phase during the experiment.

All quenched glasses were prepared for both SIMS measurement and for spectroscopic analysis. For SIMS measurement, samples were cut and polished down to ~200 μm thickness and then mounted on round glass slides using a carbon-free ceramic glue (a solution of sodium silicate in water). The glasses were then polished down to ~50 μm thickness. For spectroscopic measurements, another piece of glass from each sample was cut and doubly polished to ~250 μm thick slices. If necessary, the pieces were later polished down further to avoid complete absorbance in FTIR measurements. These slices were also used for Raman measurements and for investigations with an optical microscope.

**Secondary ion mass spectrometry (SIMS)**

SIMS analyses were carried out with the Cameca IMS-7f ion probe at Tohoku University. Samples were first cleaned with distilled water in an ultrasonic bath and then coated with gold. A primary beam of $Cs^+$ ions with 1-1.5 nA current and 10 kV acceleration voltage was used. The beam was focused on an area of 17 x 12 μm. The extraction voltage for secondary ions was 5 kV and the E-gun was used to compensate electric charge on the sample surface. The mass resolution was ~4000. In one measurement cycle, after pre-sputtering with a 25 x 25 μm raster for 3 min, signals of $^{12}C^-$, $^{28}Si^-$ and at a mass of 28.5 (background) were collected for 4.0 s, 1.0 s and 1.0 s, respectively, for 10 cycles. $CO_2$-bearing glass standards synthesized with the piston cylinder apparatus were used for the calibration of the SIMS data. To assure that all carbon in these glasses was present in oxidized form, $Ag_2O$ was added to the $Ag_2C_2O_4$ in the synthesis of the glasses and $Fe_2O_3$ was packed on the outside of the platinum capsules. $CO_2$ contents were determined by FTIR (see below). The measured $CO_2$ contents were always close to the nominal $CO_2$ contents as expected from the amount of $Ag_2C_2O_4$ loaded into the capsules for synthesis. Two or three glasses of MORB, andesite, or rhyolite with different carbon contents were used to define calibration curves (Fig. 6.4). All standards with corresponding composition were measured before and after each session.

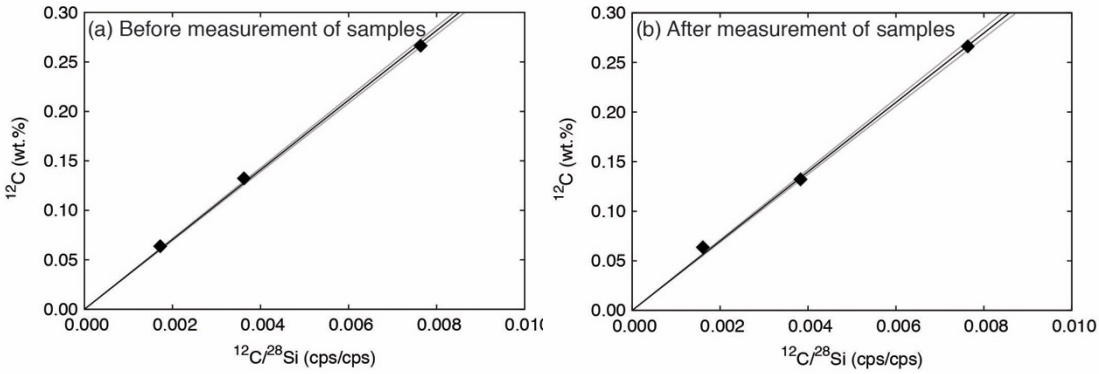


*Fig. 6.4. Examples of the SIMS calibration for MORB, using synthetic carbon-doped glasses. Carbon contents of the glasses were measured by FTIR; they are close to the nominal carbon contents of the standards according to the weight of $Ag_2C_2O_4$ loaded into the capsules for synthesis. The gray lines show the standard error (1σ) of the calibration curve.*

One of the standards was also measured before the measurement of each sample to monitor the stability of the SIMS device. Measured cps (counts per second) of $^{28}Si$ and $^{12}C$ were corrected by subtracting the cps of the 28.5 mass station and the cps of $^{12}C$ of C-free synthetic glasses, respectively. According to the calibration line obtained from the standards, the cps ratio of $^{12}C$ and $^{28}Si$ was then converted into carbon concentration, assuming that the concentration of Si in the standards and in the samples is the same.

**Infrared and Raman spectroscopy**

Infrared (FTIR) measurements were carried out with a Bruker IFS 120 HR Fourier transform spectrometer coupled to a Bruker A490 microscope with an all-reflecting 15x Cassegranian objective. A globar light source, a KBr beam splitter, and a narrow-band MCT detector were used. For each spectrum, 200 scans were measured on a doubly polished slice with a spot size of 100 – 500 µm. The sample thickness was 32-251 µm, depending on the carbon content, in order to avoid saturation of the carbonate and $CO_2$ absorption band. Background absorbance was corrected by subtracting the spectrum of a carbon-free blank glass of otherwise identical composition. Carbonate bands were quantified using the extinction coefficient given by Fine and Stolper (1986). For quantifying molecular $CO_2$ in andesite and rhyolite, the extinction coefficients given by Nowak et al. (2003) for dacite and albite were used.

Raman spectra were obtained with a confocal Horiba-Yvon Labram 800HR UV spectrometer using the 514 nm line of an argon laser at 200 mW output power. Spectra were accumulated for 5 x 4 s using a 50 x long-distance objective, a 1800 $mm^{-1}$ grating and a Peltier-cooled CCD detector.

**Fugacity calculations**

The oxygen fugacity imposed by a CO-$CO_2$ gas phase in equilibrium with graphite was obtained from the experimentally calibrated regression equation given by Jakobsson and Oskarsson (1994). Fugacities of CO and $CO_2$ were then calculated from the equilibrium constants of the reactions C + ½ $O_2$ = CO and C + $O_2$ = $CO_2$, using thermodynamic data tabulated in Robie and Hemingway (1995).

## *6.2.4. Results*

**Bulk carbon solubility**

Both IHPV and piston cylinder experiments yielded clear glasses containing some inclusions of graphite and occasionally, fluid inclusions (Fig. 6.5). In particular, in the IHPV experiments, which started with pure CO gas, the formation of graphite was always observed. Raman spectra of the fluid inclusions (Fig. 6.6) showed the presence of both $CO_2$ and CO in the gas phase, without any evidence for other gas species. Details of the high-pressure experiments and measured carbon solubilities are compiled in Table 6.3. Carbon contents measured by SIMS were always found to be homogeneous in the samples, with variations not exceeding a few percent (relative), indicating that equilibrium between the gas phase and the melt was reached. This is consistent with Nowak et al. (2004) who observed a diffusion coefficient of $CO_2$ in rhyolitic to basaltic melts near $10^{-11}$ $m^2s^{-1}$ at 1350 °C.

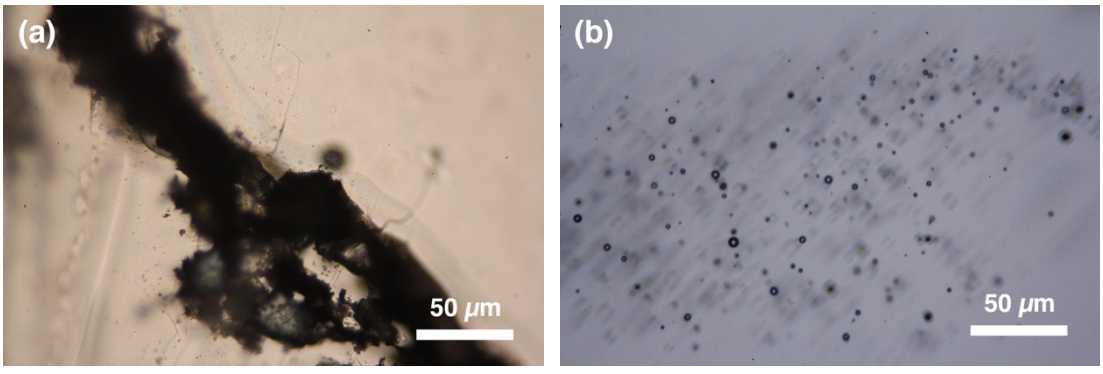


*Fig. 6.5. Optical microscope images of run products. (a) Precipitation of graphite (run A951, 2 GPa, 1600 °C) and (b) fluid inclusions (run M02, 0.2 GPa, 1300 °C) are seen in optically clear MORB glasses.*

*Table 6.3. Summary of high-pressure experiments*

| Run | Starting glass | P (GPa) | T (˚C) | Duration (h) | log $f_{CO}$ | Total carbon (wt%) | Oxidized carbon (wt%) | Reduced carbon (wt%) | CO band absorbance ($cm^{-2}$) |
|---|---|---|---|---|---|---|---|---|---|
| M02 | MORB 1 | 0.208 | 1300 | 4 | 3.62 | 0.0342 (17) | 0.0244 (17) | 0.0097 (24) | - |
| M10b | MORB 2 | 0.306 | 1250 | 6 | 3.57 | 0.0423 (10) | n.m. | - | - |
| M13 | MORB 2 | 0.308 | 1300 | 6 | 3.67 | 0.0455 (25) | 0.0396 (5) | 0.0059 (26) | - |
| M12 | MORB 2 | 0.306 | 1400 | 3 | 3.85 | 0.0325 (14) | 0.0205 (7) | 0.012 (15) | - |
| M09 | MORB 2 | 0.492 | 1300 | 6 | 3.78 | 0.0961 (38) | 0.0933 (86) | 0.0028 (94) | - |
| C398 | MORB 2 | 1 | 1500 | 6 | 4.34 | 0.1672 (49) | 0.1679 (33) | -0.0007 (60) | - |
| A868 | MORB 1 | 2 | 1400 | 6 | 4.72 | 0.3633 (176) | n.m. | - | n.m. |
| A897 | MORB 1 | 2 | 1500 | 6 | 4.82 | 0.4465 (218) | 0.3889 (28) | 0.0577 (220) | 62.71 (360) |
| A951 | MORB 1 | 2 | 1600 | 6 | 4.90 | 0.5223 (190) | 0.3884 (77) | 0.1339 (205) | 119.21 (207) |
| A914 | MORB 1 | 3 | 1500 | 6 | 5.30 | 0.2273 (100) | 0.1761 (32) | 0.0513 (105) | - |
| | | | | | | | | | |
| A07 | Andesite | 0.207 | 1300 | 2+3.5 | 3.62 | 0.0118 (5) | 0.0108 (9) | 0.0010 (10) | - |
| A04 | Andesite | 0.309 | 1200 | 2 | 3.48 | 0.0160 (44) | n.m. | - | n.m. |
| A13b | Andesite | 0.300 | 1300 | 7 | 3.67 | 0.0194 (12) | 0.0163 (5) | 0.0031 (13) | - |
| A12 | Andesite | 0.305 | 1400 | 3 | 3.85 | 0.0188 (8) | 0.0166 (11) | 0.0022 (14) | - |
| A09c | Andesite | 0.411 | 1300 | 6 | 3.73 | 0.0352 (12) | 0.0208 (9) | 0.0143 (15) | - |
| A09b | Andesite | 0.496 | 1300 | 6 | 3.78 | 0.0361 (6) | 0.0243 (28) | 0.0118 (39) | - |
| C399 | Andesite | 1 | 1500 | 6 | 4.34 | 0.0987 (38) | 0.1185 (40) | -0.0198 (55) | - |
| A911 | Andesite | 2 | 1500 | 6 | 4.82 | 0.3215 (100) | 0.315 (94) | 0.0065 (138) | - |
| A954 | Andesite | 2 | 1600 | 6 | 4.90 | 0.2676 (74) | 0.2563 (101) | 0.0113 (125) | 21.22 (419) |
| A955 | Andesite | 3 | 1500 | 6 | 5.30 | 0.5361 (115) | 0.5073 (63) | 0.0288 (131) | 23.82 (188) |

| Run | Starting glass | P (GPa) | T (˚C) | Duration (h) | log $f_{CO}$ | Total carbon (wt%) | Oxidized carbon (wt%) | Reduced carbon (wt%) | CO band absorbance ($cm^{-2}$) |
|---|---|---|---|---|---|---|---|---|---|
| R02 | Rhyolite | 0.208 | 1300 | 4 | 3.62 | 0.0199 (13) | 0.0124 (10) | 0.0075 (17) | 57.51 (584) |
| R04 | Rhyolite | 0.309 | 1200 | 2 | 3.48 | 0.0355 (31) | 0.0327 (13) | 0.0028 (34) | 84.56 (1223) |
| R01 | Rhyolite | 0.308 | 1300 | 2 | 3.67 | 0.0327 (23) | 0.0232 (26) | 0.0095 (35) | 102.22 (620) |
| R12c | Rhyolite | 0.307 | 1400 | 3 | 3.85 | 0.0303 (26) | 0.0345 (18) | -0.0042 (31) | 58.02 (555) |
| R03 | Rhyolite | 0.498 | 1300 | 2 | 3.78 | 0.0694 (10) | 0.0506 (25) | 0.0188 (26) | 98.56 (1223) |
| A987 | Rhyolite | 1 | 1500 | 6 | 4.34 | 0.1803 (17) | 0.1642 (86) | 0.0161 (88) | 106.96 (827) |
| A919 | Rhyolite | 2 | 1400 | 6 | 4.72 | 0.4053 (154) | 0.3932 (66) | 0.0121 (168) | 46.66 (133) |
| A910 | Rhyolite | 2 | 1500 | 6 | 4.82 | 0.4749 (78) | 0.4312 (65) | 0.0437 (102) | 152.62 (962) |
| A952 | Rhyolite | 2 | 1600 | 6 | 4.90 | 0.3946 (101) | 0.3035 (24) | 0.0911 (103) | 254.77 (1363) |
| C394 | Rhyolite | 3 | 1500 | 6 | 5.30 | 0.6811 (216) | 0.5893 (315) | 0.0918 (382) | 106.09 (334) |

*log $f_{CO}$ is the calculated logarithm of the CO fugacity (in bar). Total carbon was determined by SIMS. Oxidized carbon is the sum of molecular $CO_2$ and carbonate, as determined by FTIR. Reduced carbon is the difference between total carbon and oxidized carbon. CO band absorbance is the integral absorbance of the bands in the 2100 – 2000 $cm^{-1}$ range, normalized to 1 cm thickness. Where numbers for absorbance are not given, the band was not detectable. Numbers in parentheses are one standard deviation in the last digits. n.m. = not measured (samples contained some crystals).*

*Table 6.4. Henry coefficients of bulk carbon solubility (in ppm/MPa) in silicate melts in equilibrium with graphite and a CO-$CO_2$ gas phase*

| | Henry coefficient 1300 ˚C up to 0.5 GPa | Henry coefficient all data |
|---|---|---|
| MORB | 1.80 (14) | 2.15 (13)* |
| Andesite | 0.69 (4) | 1.57 (10) |
| Rhyolite | 1.26 (13) | 2.14 (8) |

*All Henry coefficients are given in ppm by weight of carbon per MPa. Numbers in parentheses give the standard error in the last digits of the Henry constant.*
** For the calculation of the Henry coefficient of MORB, the data from run A914 were excluded, as the measured carbon solubility appears anomalously low and may have been affected by a leakage of the capsule.*

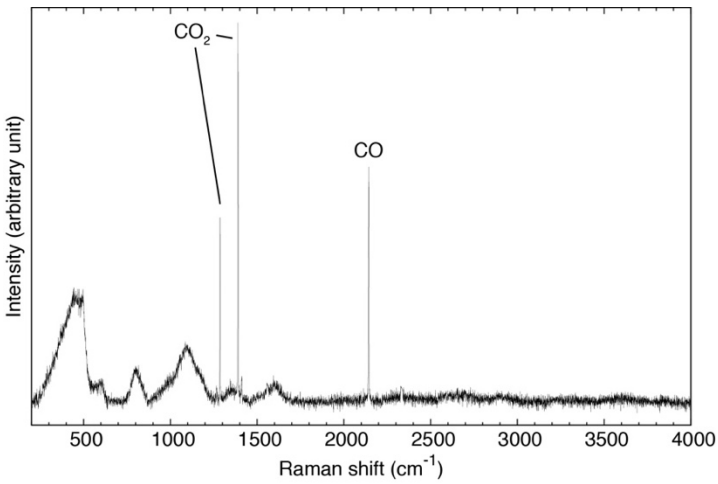


*Fig. 6.6. Baseline-corrected Raman spectrum of a fluid inclusion inside a rhyolite glass. Sharp bands of both $CO_2$ (1286 and 1390 $cm^{-1}$) and CO (2143 $cm^{-1}$) gas are visible (run R01, 0.3 GPa, 1300 ˚C).*

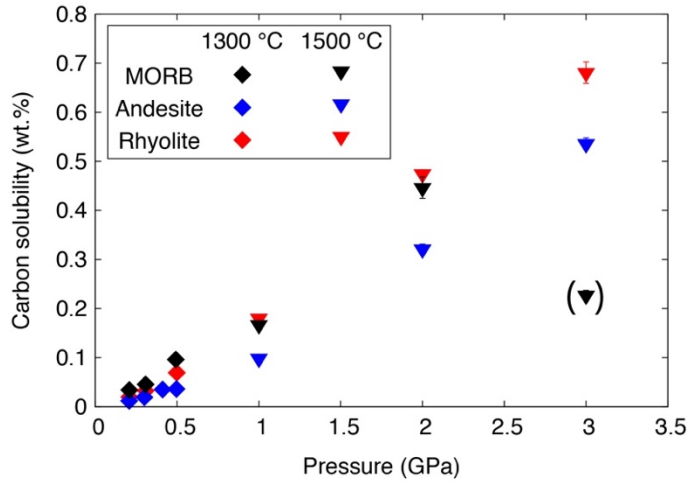


*Fig. 6.7.. Bulk carbon solubility in silicate melts coexisting with graphite and a CO-$CO_2$ fluid phase as a function of pressure. The MORB data point at 3 GPa (experiment A914) shown in brackets appears anomalous, possibly due to a leak of the capsule.*

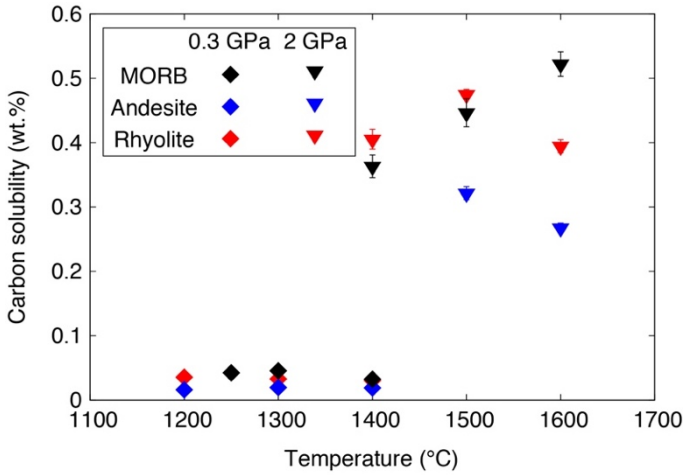


*Fig. 6.8. Bulk carbon solubility in silicate melts coexisting with graphite and a CO-$CO_2$ fluid phase as a function of temperature.*

This translates into a mean diffusion path of 0.3 mm for 1 hour run duration, which is much larger than the initial grain size of the powder loaded into the capsule (about 10 μm). Since CO is smaller than $CO_2$, it should diffuse even faster. The consistency between the IHPV (0.2 – 0.5 GPa) and piston cylinder experiments (1 – 3 GPa) is another line of evidence demonstrating attainment of equilibrium, since the former experiments started with pure CO gas, while in the latter experiments, the gas phase was initially pure $CO_2$ (from the decomposition of $Ag_2C_2O_4$) and CO was produced only during the run by reaction with graphite. As shown in Fig. 6.7, carbon solubility in all three melt compositions studied is almost directly proportional to pressure, i.e. it follows Henry´s law with good approximation. Table 6.4 compiles Henry coefficients of carbon solubility for MORB, andesite, and rhyolite, using all data for each composition or only the low-pressure data up to 0.5 GPa at a constant temperature at 1300 ˚C. The Henry coefficients including all data over the full pressure range studied are rather similar for the three melt compositions. However, close inspection of Fig. 6.7 shows that while the MORB data closely adhere to a linear trend over the entire pressure range studied, both andesite and rhyolite solubility initially follow a more shallow slope. Accordingly, the apparent Henry coefficients for andesite and rhyolite increase with pressure (Table 6.4).

Temperature has only a subordinate effect on bulk carbon solubility. Fig. 6.8 compares the observed temperature dependence of bulk carbon solubility at 0.3 GPa and at 2 GPa. There is only a minor temperature effect at 0.3 GPa; in particular for rhyolite, the solubility appears to slightly decrease with temperature. On the other hand, the 2 GPa MORB data suggest an increase of solubility with temperature, while for andesite and rhyolite, the trend is not clear. However, a change from negative to positive temperature dependence of solubility with pressure has been observed for other volatiles as well, in particularly for water (e.g. Holtz et al. 1995). Such a change may be rationalized by considering the entropy of the dissolution reaction. At low pressure, the entropy of the low-density gas phase is high. As with increasing temperature the entropy contribution to the Gibbs free energy increases, the equilibrium of a volatile species between melt and gas should shift towards the gas phase. At high pressures, however, the gas phase becomes a dense fluid with a liquid-like structure; the higher mixing entropy in the melt phase may then have the effect that increasing temperature promotes volatile dissolution in the melt.

## Carbon speciation and CO solubility

Infrared spectra of carbon-saturated MORB, andesite, and rhyolite glasses obtained at 0.3 and at 2 GPa are shown in Fig. 6.9. Bands of oxidized carbon – molecular $CO_2$ and/or carbonate, depending on composition (see also Konschak and Keppler 2014) – are prominent in the spectra, while weak bands in the 2100 – 2200 $cm^{-1}$ region that may be assigned to CO (Yoshioka et al. 2015) are only occasionally seen. This observation agrees well with the previous study of Pawley et al. (1992) who failed to detect any indication for dissolved CO in the infrared spectra of MORB glasses synthesized at up to 150 MPa in the presence of graphite and a CO-$CO_2$ fluid. Similarly, Raman spectra of the glasses (Fig. 6.10) only occasionally show bands that may be assigned to dissolved CO. C-H stretching bands near 2900 $cm^{-1}$ were only observed near graphite inclusions and may represent surface absorbed material. Methane ($CH_4$) was never observed in the Raman spectra of fluid inclusions (Fig. 6.6), in agreement with the nominally anhydrous nature of the

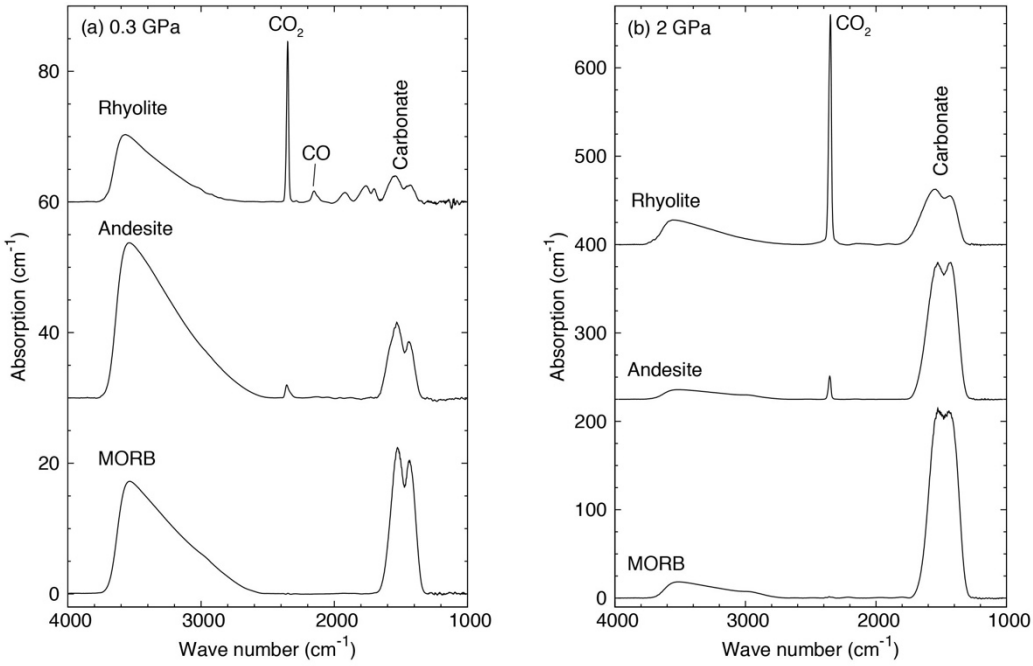


*Fig. 6.9. Infrared (FTIR) spectra of run product glasses after background correction and normalized to 1 cm sample thickness. (a) Samples synthesized at 0.3 GPa and 1300 ˚C (MORB M13, andesite A13b, rhyolite R01). (b) Samples synthesized at 2 GPa and 1500 ˚C (MORB A897, andesite A911, rhyolite A910). Note that bands of oxidized carbon ($CO_2$ or carbonate) are prominent in all spectra, while a weak band due to CO is only occasionally seen.*

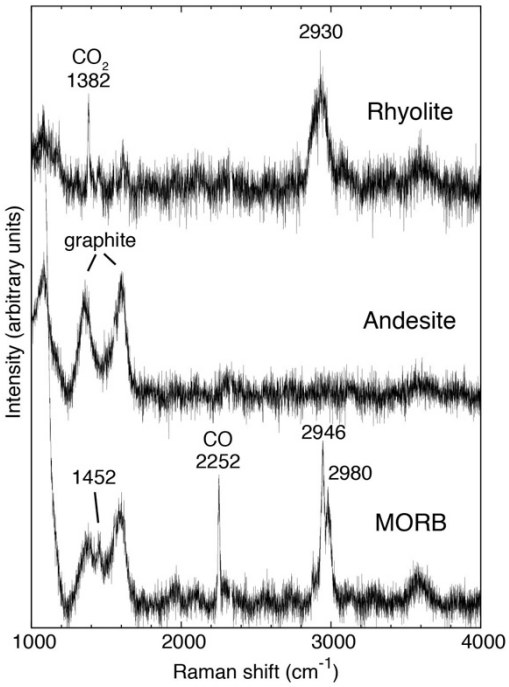


*Fig. 6.10. Raman spectra of glasses synthesized at 2 GPa (MORB A897; 1500 °C, andesite A954; 1600 °C, rhyolite A910; 1500 °C). Evidence for the presence of reduced carbon is only occasionally visible, particularly in the MORB spectrum with a prominent band at 2252 cm¹ that may be assigned to CO. The bands near 2900 cm⁻¹ may be due to $CH_4$ or other hydrocarbons; however, they are usually only observed close to graphite inclusions and may represent material absorbed on the graphite surface. The 1452 cm⁻¹ band in the MORB spectrum could be due to a C-H bending vibration of such species. The carbonate bands overlap in the Raman spectrum with the prominent Si-O stretching bands around 1000 cm¹ and are therefore hard to detect However, the rhyolite spectrum shows a band of molecular $CO_2$ at 1382 cm⁻¹.*

experiments. Accordingly, in the following discussion we will assume that any reduced carbon in the glasses is most likely related to dissolved CO.

Fig. 6.11 shows the concentrations of reduced carbon in the run product glasses as a function of pressure. These data were obtained by subtracting the concentration of oxidized carbon quantified by the $CO_2$ and carbonate peaks in the infrared spectra from the total carbon as measured by SIMS. Table 6.3 shows that in very few cases, this subtraction produced spurious, slightly negative differences, but in most cases, it indicated that indeed a non-negligible fraction of carbon in the glasses is present in reduced form. Naturally, subtracting carbon concentrations obtained by two different analytical methods may lead to results that are biased by some systematic errors inherent

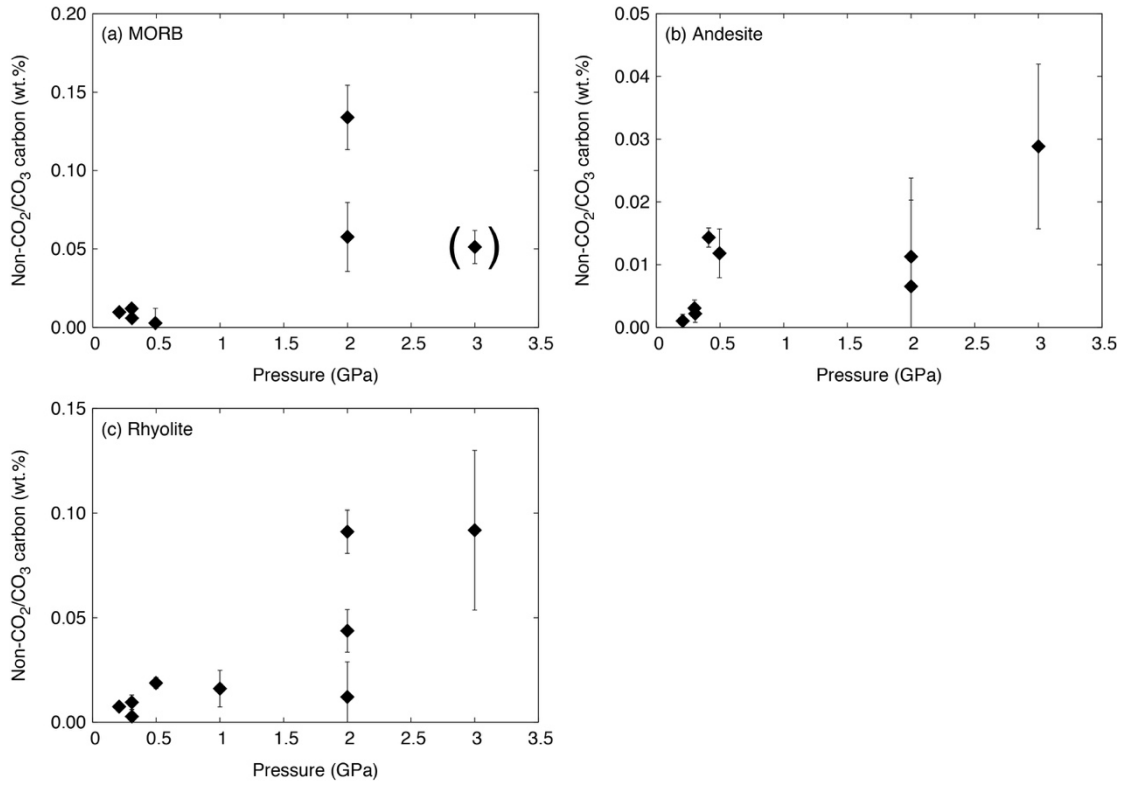


*Fig. 6.11. Solubility of reduced carbon in silicate melts in equilibrium with graphite and a $CO_2$-CO gas phase as function of pressure. Data were obtained by subtracting the $CO_2$ content determined by FTIR from the bulk carbon data obtained by SIMS. The MORB data point shown in brackets (experiment A914) has anomalously low bulk carbon contents, possibly due to a leak of the capsule.*

to one or the other method. In the present study, however, the SIMS measurements were calibrated by FTIR data obtained on standard glasses of exactly the same bulk compositions as the samples studied. Moreover, the procedure used for the FTIR quantification of carbon in the SIMS standards was exactly the same as that used for determining the oxidized carbon concentration in the samples. Accordingly, we are confident that the concentrations of reduced carbon shown in Fig. 6.11 are real, although the statistical uncertainties are considerable. A comparison of Fig. 6.7 and Fig. 6.11 shows that for MORB and rhyolite, on average about 10 - 20 % of the total carbon is dissolved in reduced form, while for andesite, this fraction is lower, on the order of 5 %. The similarity of CO solubility in MORB and rhyolite is not what one would expect from ionic porosity arguments. Noble gas solubilities generally increase with ionic porosity (Carroll and Webster 1994 and references therein). Possibly, some kind of chemical interaction with the silicate melt may affect the observed solubility trend. Since the CO molecule has a permanent dipole moment, some interaction of the positively charged carbon atom with

non-bridging oxygen atoms in the MORB melt may enhance solubility and compensate for the effect of reduced ionic porosity. The combined effect of chemical interaction and ionic porosity could also produce the apparent solubility minimum in andesite melt. However, due to the considerable analytical uncertainties in these measurements, it is not entirely certain how significant this minimum is.

In general, the measured concentrations of reduced carbon – interpreted to be due to dissolved CO - correlate well with the calculated CO fugacity in the experiments (Table 6.3). For MORB and rhyolite, linear regression yielded the following relationships

$$(2) \qquad \log c_{CO}^{MORB} = -5.83 + 0.98 \log f_{CO} \qquad (R^2 = 0.84)$$

$$(3) \qquad \log c_{CO}^{Rhyolite} = -4.52 + 0.65 \log f_{CO} \qquad (R^2 = 0.74)$$

where $\log c_{CO}$ is the logarithm of the concentration of reduced carbon (in wt. %) and $\log f_{CO}$ is the logarithm of CO solubility. Note that the coefficient before the $\log f_{CO}$ term in these equations is close to unity, particularly for MORB. This is consistent with the direct dissolution of CO as CO molecules in the melt. In accordance with the small influence of temperature on bulk carbon solubility, the effect of temperature is neglected in these equations. Pressure influences CO solubility primarily through its effect on CO fugacity. The effect of changes in the volume of the melt due to the dissolution of CO is ignored. The latter effect could be described by an additional term depending on pressure, but this term is expected to be small and it is not well constrained by the available data. For andesite, the large scatter of the data at low pressure (≤ 0.5 GPa, see Fig. 6.11b) introduces considerable uncertainties in the fit and therefore, no regression equation is given.

While the concentrations of reduced carbon detected are highest in MORB samples, FTIR spectra of these glasses only occasionally show weak bands in the 2100 – 2200 $cm^{-1}$ range that may be related to dissolved CO (Table 6.3). However, such bands are often seen in the rhyolite glass samples. Fig. 6.12 shows a plot of the integral CO band intensity as a function of reduced carbon content for the rhyolite samples. Despite the significant uncertainties of the data, there appears to be a correlation between these numbers, consistent with the assignment of the reduced carbon to CO molecules in the (quenched)

melt. The regression fit shown in Fig. 6.12 ($R^2$ = 0.82) has a slope of 2201 $cm^{-2}$ per wt.%. This translates into an integral molar extinction coefficient of 966 liter $mol^{-1}$ $cm^{-2}$. Notably, this number is between one and two orders of magnitude lower than the typical extinction coefficients of molecular $CO_2$ or carbonate in silicate glasses (Ni and Keppler 2013). Moreover, detailed inspection of the infrared spectra shows that sometimes, the absorbance in the 2100 – 2200 $cm^{-1}$ range is due to a combination of several bands (Fig. 6.13), which are probably due to CO molecules in different chemical environments. Theoretical studies of CO molecules adsorbed on oxide surfaces (Neyman and Rösch 1992) suggest that the infrared extinction coefficient of CO may be very sensitive to subtle

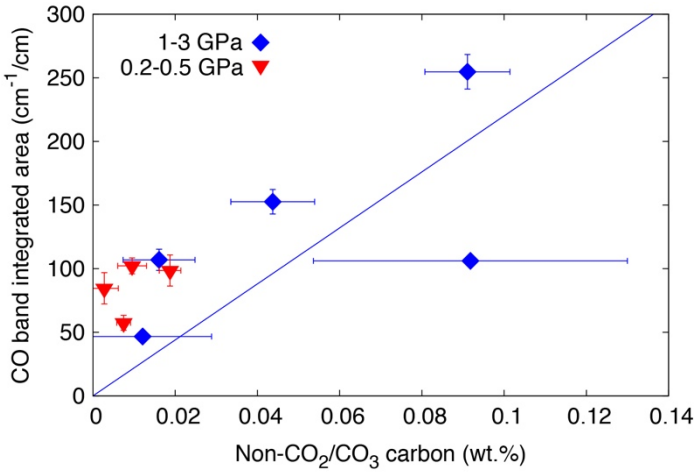


*Fig. 6.12. Integrated intensity of the CO band at 2100 – 2200 $cm^{-1}$ in the infrared spectrum as a function of reduced carbon content. The regression fit is based on the 1 – 3 GPa data only.*

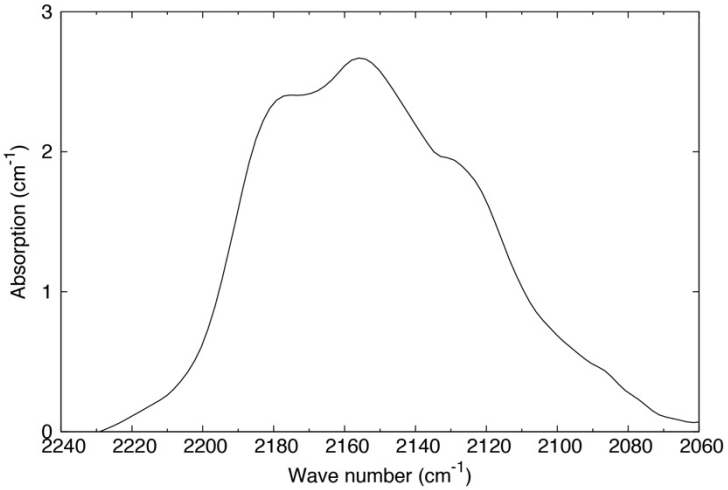


*Fig. 6.13. Detail of the CO band region of the infrared spectrum of rhyolite sample A952, synthesized at 2 GPa and 1600 °C. At least three different band components are seen in the spectrum.*

variations in the chemical environment. The scatter of the data in Fig. 6.12 may therefore be due to different CO species with different individual extinction coefficients occurring in the samples in variable proportions. Together with the generally very low extinction coefficient, the dependence of infrared extinction on the environment of the CO molecule may explain why in the majority of the MORB glasses, CO is not detectable in the infrared spectra, as the extinction coefficient for MORB may be even lower than that inferred for rhyolite. Accordingly, the infrared extinction coefficient of 966 liter $mol^{-1}$ $cm^{-2}$ given here for rhyolite glasses should not be used to estimate CO contents in samples of different composition.

### *6.2.5. Discussion*

**A comparison of CO and $CO_2$ solubility in silicate melts**

When comparing the results of the present study with data on $CO_2$ solubility in silicate melts, it is important to note that the CO-$CO_2$ gas phase composition in equilibrium with graphite strongly changes as function of pressure and temperature. For example, at 1300 ˚C, the molar fraction of CO in the gas phase decreases from about 37 % at 200 MPa to 18 % at 1 GPa and to a mere 2 % at 3 GPa. This strong effect of pressure is due to the fact that the reaction 2 CO = C + $CO_2$ involves a large decrease in molar volume, since there are two molecules of gas on the left hand side of the equation, but only one on the right hand side. For similar reasons, the entropy is higher on the CO side of the equilibrium and accordingly, high temperatures shift the equilibrium to the left. As a result of this effect, the molar fraction of CO at 3 GPa increases from 2 % at 1300 ˚C to 8 % at 1600 ˚C. In any case, however, at high pressures above 1 GPa, the gas phase consists mostly of $CO_2$ with only subordinate amounts of CO. Accordingly, the bulk carbon solubility observed in the present experiments at high pressure should be comparable to data for $CO_2$ solubility. Indeed, Ni and Keppler (2013) showed that available data for $CO_2$ solubility in basaltic and rhyolitic melts to 0.7 GPa may be described by a single Henry constant of 0.57 ppm $CO_2$ /bar, which is equivalent to 1.55 ppm of carbon per MPa. This is in the same range as most of the Henry coefficients reported in Table 6.4. Notably, the Henry coefficients for MORB and rhyolite fit to all data – where the overall fit is mostly controlled by the high-

pressure data points – suggest a carbon solubility in equilibrium with a CO-$CO_2$ gas phase that is even slightly higher than that predicted for pure $CO_2$ according to Ni and Keppler (2013). This may perhaps be due to differences in temperature or bulk melt composition between the two data sets; a significant positive deviation from ideal mixing in the CO-$CO_2$ gas phase at high pressure could also contribute to this effect. If only the carbon solubility data up to 0.5 GPa in equilibrium with a CO-$CO_2$ gas phase are considered, the Henry coefficients Table 6.4 are lower, but (with the exception of the andesite data), they are still quite similar to the value of 1.55 ppm carbon per MPa for equilibrium with pure $CO_2$. The data of the present study therefore show that carbon solubility in silicate melts in equilibrium with a CO-$CO_2$ gas phase buffered by graphite above 200 MPa is by no means much lower than for pure $CO_2$.

The regression equations (2) and (3) also allow predicting the solubility of carbon in equilibrium with a pure CO gas phase. Since our experiments show that a pure CO gas at magmatic temperatures already within a few hours precipitates graphite and therefore attains the equilibrium 2 CO = C + $CO_2$, this solubility will only be relevant under special circumstances, e.g. during vapor saturation upon rapid decompression, when graphite precipitation may be suppressed for kinetic reasons. For a pressure of 100 MPa, a carbon solubility in MORB in equilibrium with pure CO in the order of 13 ppm is predicted, about one order of magnitude below that predicted for pure $CO_2$.

The results of the present study may be compared with the results of Stanley et al. (2014) and Armstrong et al. (2015), who investigated graphite solubility in silicate melts under reducing conditions in the 1 – 3 GPa pressure range. Notably, these experiments are conceptually different from those described here, since they were carried out under vapor-undersaturated conditions, but with controlled oxygen fugacity. Due to the absence of simultaneous saturation with a CO-$CO_2$ vapor phase, the reduced carbon concentrations reported by Stanley et al. (2014) and Armstrong et al. (2015) are generally lower (about 1 – 200 ppm) than those observed in the present study. However, the dependence of reduced carbon concentration on CO fugacity appears to follow a similar exponent (0.876) as observed here, while the Wetzel et al. (2013) data describe a steeper trend. The regression equation given by Armstrong et al. (2015) would predict a carbon solubility in equilibrium with 100 MPa of pure CO near 78 ppm, significantly

higher than inferred from the present data (13 ppm, see above). However, this calculation involves a rather far extrapolation of the experimental data. Moreover, the systems studied by Stanley et al. (2014) and Armstrong et al. (2015) are chemically more complex, containing both significant H and N, such that not all of the measured reduced carbon may be due to dissolved CO. Indeed, Armstrong et al. (2015) did not observe a clear correlation of reduced carbon contents with the infrared absorbance in the 2100 – 2200 $cm^{-1}$ range.

The studies of Pawley et al. (1992) and of Morizet et al. (2010) investigated carbon solubility in equilibrium with a C-O or C-O-H fluid at moderate pressures up to 300 MPa. Both studies concluded that the carbon solubility due to reduced species is negligibly small. This conclusion was, however, mostly based on spectroscopic (FTIR) measurements and may partially reflect the low infrared extinction coefficient of CO in silicate melts, as shown in the present study, which makes the detection of CO even at the 100 ppm level difficult (see the CO band absorbances and reduced carbon contents in Table 6.3).

**The role of CO in volcanic activity on the Moon**

Picritic glasses from the Moon, such as the Apollo 15 green and yellow glasses and the Apollo 17 orange glasses have traditionally been interpreted as the products of volcanic fire-fountain eruptions (e.g. Heiken et al. 1974). Because the lunar magmas for a long time were believed to be essentially dry and because of the rather low oxygen fugacities prevailing, CO was proposed as the main propellant of these eruptions (Fogel and Rutherford 1995). However, recent analyses of these glasses and associated melt inclusions suggest that the parent magmas contained not only 0.3 – 0.7 ppm of carbon, but also hydrogen equivalent up to 70 ppm of $H_2O$ (Wetzel et al. 2015). In the associated melt inclusions, volatile concentrations are even higher, with up to 4 ppm carbon and more than 1000 ppm $H_2O$ (Wetzel et al. 2015). Therefore, the contribution of all these volatiles to the dynamics of the fire fountain eruption has to be considered, including the initial nucleation of gas bubbles, the magma fragmentation and the overall energy balance. Already the much larger initial concentrations of hydrogen as compared to

carbon suggest that at the fragmentation stage, when most of the volatiles had been lost, the gas phase was dominated by hydrogen and water, in agreement with the quantitative modeling by Newcombe et al. (2017). However, the compositional trends shown by Wetzel et al. (2015) also suggest that carbon degassed before hydrogen. Under the low oxygen fugacity imposed by these magmas, it is plausible that a significant fraction of the carbon was dissolved as CO. The CO solubilities obtained in the present study may therefore be used to infer the plausible CO partial pressures in equilibrium with the melt. For 0.3 – 0.7 ppm of carbon as observed in the glass samples, equation (2) predicts a CO fugacity of 2.3 – 5.4 MPa, while 4 ppm of carbon as recorded in melt inclusions yield 31 MPa, equivalent to about 7.4 km below the lunar surface. Because of the low pressures that imply nearly ideal gas behavior, the fugacities can be considered to be equivalent to partial pressures. In general, these estimates are in very good agreement with those obtained by Newcombe et al. (2017) using different thermodynamic arguments. The calculations, however, assume that graphite precipitation from the gas phase and therefore attainment of the equilibrium 2 CO = C+ $CO_2$ does not occur. If graphite precipitates and $CO_2$ forms, the inferred gas pressures would decrease significantly due to the higher solubility of $CO_2$ in the melt.

Overall, the CO solubility data in conjunction with the carbon contents of the lunar glasses suggest that CO degassing may have been important in the initial volatile saturation and bubble nucleation event during the ascent of the magma to the surface. The final carbon contents retained in the lunar glasses are out of equilibrium with the near-vacuum conditions on the lunar surface and suggest some kinetic limitation of degasing, perhaps due to rapid ascent and quenching on the surface.

**CO in a primordial atmosphere coexisting with a magma ocean**

The distribution of elements between core, mantle and near-surface reservoirs on Earth was likely influenced by chemical fractionation processes in a deep magma ocean that formed during the late stages of accretion (e.g. Elkins-Tanton 2008, 2012, Rubie et al. 2015). Carbon is a volatile element that is expected to partition strongly into the metal phase of the core (e.g. Dasgupta et al. 2013), while the silicate minerals of the mantle

incorporate almost no carbon in their structure (Keppler et al. 2003, Shcheka et al. 2006). Accordingly, one may expect that during the evolution of a magma ocean, carbon may be partially retained in the primordial atmosphere and partially be concentrated in the core (e.g. Hirschmann 2012, 2016). The efficiency of these processes depends on the redox state and depth of the magma ocean, which influence the metal/melt partitioning, and on the speciation of carbon in the primordial atmosphere, which controls the solubility of carbon in the coexisting melt phase. Since CO is much less soluble in silicate melts than $CO_2$, one may perhaps expect that with decreasing oxygen fugacity, as imposed by the $Fe^{3+}/Fe^{2+}$ ratio of the magma ocean, the concentration of carbon in equilibrium with a primordial atmosphere continuously decreases. However, it is very likely that the composition of a primordial atmosphere is buffered by the equilibrium with graphite. Many carbonaceous chondrites have C/H weight ratios exceeding 10 (Kerridge 1985), implying that even if all this hydrogen were present in the form of $H_2O$ or OH groups, the amount of oxygen contained in it would not be sufficient to oxidize all the carbon to CO or $CO_2$. Moreover, the redox state of the magma ocean during accretion (e.g. Hirschmann 2012, Rubie et al. 2015) is initially far below the IW-buffer, such that chemical equilibration of the magma ocean with the overlying atmosphere would tend to reduce CO and $CO_2$ to graphite. Graphite is specifically lighter than a peridotitic melt (density of 2.7 g/cm$^3$ at 2000 K; Courtial et al. 1997) and would therefore accumulate on the surface of the magma ocean. If a large fraction of total carbon were reduced to graphite, this would imply a low $CO/CO_2$ partial pressure. In such a situation, the equilibrium between $CO_2$ and CO in the primordial atmosphere is shifted towards CO, which is poorly soluble in silicate melts. This could be a plausible mechanism for limiting the partitioning of carbon into the core and for retaining a significant fraction of total carbon near the surface of the early Earth.

**A note of caution: CO in silicate melts is easily overlooked**

The comparison of Fig. 6.7 and Fig. 6.11 shows that under saturation with a $CO\text{-}CO_2$ gas phase and graphite, dissolved CO is only a minor species of carbon in the silicate melt in the range of pressures studied, about one order of magnitude less abundant than oxidized carbon in the form of molecular $CO_2$ or carbonate. However, this situation will change at

more reducing conditions below the CCO buffer. Due to the equilibrium CO + ½ $O_2$ = $CO_2$, the fugacity ratio of $CO_2$ and CO, $f_{CO2}/f_{CO}$ has to increase with the square root of the oxygen fugacity. This implies that at already two log units in oxygen fugacity below the CCO buffer, dissolved CO will be as abundant as oxidized carbon and at even more reducing conditions, it will dominate carbon speciation in the melt. Due to the very low and probably matrix-dependent infrared extinction coefficient of CO, it is quite possible that a significant fraction of carbon dissolved in graphite-saturated glasses (e.g. Duncan et al. 2017, Duncan and Dasgupta 2017) may remain invisible in infrared spectra.

### *6.2.6. Acknowledgments*

The authors would like to thank Raffael Njul and Hubert Schulze for sample polishing, Detlef Krausse for help with the microprobe analyses and Masakuni Yamanobe and Takamichi Miyazaki for help with SIMS analyses.
This work was supported by the JSPS Japanese-German Graduate Externship.

### *6.2.7. References*

Albarède, F. (2005). The survival of mantle geochemical heterogeneities. In Earth's Deep Mantle: Structure, Composition, and Evolution (Eds van der Hilst R.D., Bass, J., Matas, J. and Trampert. J.). AGU Geophys. Monogr. 160, 27-46.

Armstrong L.S., Hirschmann M.M., Stanley B.D., Falksen, E.G. and Jacobsen, S.D. (2015) Speciation and solubility of reduced C–O–H–N volatiles in mafic melt: Implications for volcanism, atmospheric evolution, and deep volatile cycles in the terrestrial planets. Geochim. Cosmochim. Acta 171, 283-302.

Boettcher S.L., Guo Q. and Montana, A. (1989) A simple device for loading gases in high pressure experiments. Am. Mineral. 74, 1383–1384.

Brooker R.A., Kohn S.C., Holloway J.R., McMillan P.F. and Carroll M.R. (1999) Solubility, speciation and dissolution mechanism for $CO_2$ in melts on the $NaAlO_2$-$SiO_2$ join. Geochim. Cosmochim. Acta 63, 3549-3565.

Carroll M.R. and Webster J.D. (1994) Solubilities of sulfur, noble gases, nitrogen, chlorine, and sulfur in magmas. Rev. Mineral. 30, 231-279.

Courtial P., Ohtani E and Dingwell D.B. (1997) High-temperature densities of some mantle melts. Geochim. Cosmochim. Acta 61, 3111-3119.

Cox K.G., Bell J.D. and Pankhurst R.J. (1979) The interpretation of igneous rocks. Springer, Heidelberg, New York.

Dasgupta R., Chi H., Shimizu N., Buono A.S. and Walker, D. (2013) Carbon solution and partitioning between metallic and silicate melts in a shallow magma ocean: implications for the origin and distribution of terrestrial carbon. Geochim. Cosmochim. Acta 102, 191–212.

Duncan M.S. and Dasgupta R. (2017) Rise of Earth's atmospheric oxygen controlled by efficient subduction of organic carbon. Nature Geosci. 10, 387-392.

Duncan M.S., Dasgupta R. and Tsuno K. (2017) Experimental determination of $CO_2$ content at graphite saturation along a natural basalt-peridotite melt join: Implications for the fate of carbon in terrestrial magma oceans. Earth Planet. Sci. Lett. 466, 115–128.

Elkins-Tanton L.T. (2008) Linked magma ocean solidification and atmospheric growth for Earth and Mars. Earth Planet. Sci. Lett. 271, 181–191.

Elkins-Tanton L.T. (2012) Magma oceans in the inner solar system. Annu. Rev. Earth Planet. Sci. 40, 113–139.

Fine G. and Stolper E. (1986) Dissolved carbon dioxide in basaltic glasses: concentrations and speciation. Earth Planet. Sci. Lett. 76, 263-278.

Fogel R.A., Rutherford M.J. (1995) Magmatic volatiles in primitive lunar glasses: I. FTIR and EPMA analyses of Apollo 15 green and yellow glasses and revision of the volatile-assisted fire-fountain theory. Geochim. Cosmochim. Acta 59, 201-215.

French B.M and Eugster H.P. (1965) Experimental control of oxygen fugacities by graphite-gas equilibriums. J Geophys. Res. 70, 1529-1539.

Frost D.J. and McCammon C.A. (2008) The redox state of Earth's mantle. Annu. Rev. Earth Planet. Sci. 36, 389–420.

Heiken G.H., McKay D.S. and Brown R.W. (1974) Lunar deposits of possible pyroclastic origin. Geochim. Cosmochim. Acta 38, 1703-1704.

Hirschmann M.M. (2012) Magma ocean influence on early atmosphere mass and composition. Earth Planet. Sci. Lett. 341-344, 48–57.

Hirschmann, M.M. (2016) Constraints on the early delivery and fractionation of Earth's major volatiles from C/H, C/N, and C/S ratios. Am Mineral 101, 540-553

Holtz F., Behrens H., Dingwell D.B. and Johannes W. (1995) Water solubility in haplogranitic melts. Compositional, pressure and temperature dependence. Am. Mineral. 80, 94-108.

Jakobsson S. and Oskarsson N. (1994) The system C-O in equilibrium with graphite at high pressure and temperature: An experimental study. Geochim. Cosmochim. Acta 58, 9-17.

Keppler H., Wiedenbeck M. and Shcheka S.S. (2003) Carbon solubility in olivine and the mode of carbon storage in the Earth's mantle. Nature 424, 414–416.

Kerridge J.F. (1985) Carbon, hydrogen and nitrogen in carbonaceous chondrites: Abundances and isotopic compositions in bulk samples. Geochim. Cosmochim. Acta 49, 1707-1714.

Konschak A. and Keppler H. (2014) The speciation of carbon dioxide in silicate melts. Contrib. Mineral. Petrol. 167, 998.

Morizet Y., Paris M., Gaillard F. And Scaillet B. (2010) C–O–H fluid solubility in haplobasalt under reducing conditions: an experimental study. Chem. Geol. 279, 1–16.

Newcombe M.E., Brett A., Beckett J.R., Baker M.B., Newman S., Guan Y., Eiler J.M. and Stolper E.M. (2017) Solubility of water in lunar basalt at low $pH_2O$. Geochim. Cosmochim. Acta 200, 330–352.

Neyman K.M., and Rösch N. (1992) CO bonding and vibrational modes on a perfect MgO (001) surface: LCGTO-LDF model cluster investigation. Chem. Phys. 168, 267–280.

Ni H. and Keppler H. (2013) Carbon in silicate melts. Rev. Mineral. Geochem. 75, 251-287.

Nowak M., Porbatzki D., Spickenbom K. and Diedrich O. (2003) Carbon dioxide speciation in silicate melts: a restart. Earth Planet. Sci. Lett. 2003, 131-139.

Nowak M., Schreen D. and Spickenbom K. (2004) Argon and $CO_2$ on the race track in silicate melts: A tool for the development of a $CO_2$ speciation and diffusion model. Geochim. Cosmochim. Acta 68, 5127-5138.

Oppenheimer C. and Kyle P.R. (2008) Probing the magma plumbing of Erebus volcano, Antarctica, by open-path FTIR spectroscopy of gas emissions. J. Volcanol. Geothermal Res. 177, 743-754.

Pawley A.R., Holloway J.R. and McMillan P.F. (1992) The effect of oxygen fugacity on the solubility of carbon oxygen fluids in basaltic melt. Earth Planet. Sci. Lett. 110, 213–225.

Robie R.A. and Hemingway B.S. (1995) Thermodynamic Properties of Minerals and Related Substances at 298.15 K and 1 Bar ($10^5$ Pascals) Pressure and at Higher Temperatures. US Geological Survey Bull. 2131.

Rubie D.C., Jacobson S.A., Morbidelli A., O'Brien D.P., Young E.D., de Vries J., Nimmo F., Palme H., and Frost, D.J. (2015) Accretion and differentiation of the terrestrial planets with implications for the compositions of early-formed Solar System bodies and accretion of water. Icarus 248, 89–108.

Rutherford M.J., Head J.W., Saal A.E., Hauri E. and Wilson L. (2017) Model for the origin, ascent, and eruption of lunar picritic magmas. Am Mineral. 102, 2045-2053.

Shcheka S., Wiedenbeck M., Frost D. J. and Keppler H. (2006) Carbon solubility in mantle minerals. Earth Planet. Sci. Lett. 245, 730–742.

Stanley B.D., Hirschmann M.M. and Withers A.C. (2014) Solubility of C–O–H volatiles in graphite-saturated martian basalts. Geochim. Cosmochim. Acta 129, 54–76.

Symonds R.B., Rose W.I., Bluth G.J.S., Gerlach T.M. (1994) Volcanic-gas studies: Methods, results, and applications. Rev. Mineral 30, 1-66.

Trail D., Watson E.B., and Tailby N.D. (2011) The oxidation state of Hadean magmas and implications for early Earth's atmosphere. Nature 480, 79-82.

Wetzel D.T., Rutherford M.J., Jacobsen S.D., Hauri E.H. and Saal A.E. (2013) Degassing of reduced carbon from planetary basalts. Proc. Nat. Acad. Sci. 110, 8010–8013.

Wetzel D.T., Hauri E.H., Saal A.E. and Rutherford M.J. (2015) Carbon content and degassing history of the lunar volcanic glasses. Nature Geosci. 8, 755-758.

Yoshioka T., McCammon C., Shcheka S. and Keppler H. (2015) The speciation of carbon monoxide in silicate melts and glasses. Am. Mineral. 100, 1641-1644.

## *6.2.8. Supplementary information*

*Supplementary Table 6.S1. Calculation of bulk carbon concentration in the glasses from SIMS data.*

MORB

| Run No. | P (kbar) | T (C°) | time (h) | $^{12}C$ blank (cps) | $^{12}C$ cor. sample (cps) | $^{28}Si$ cor. sample (cps) | $^{12}C/^{28}Si$ cor. sample (cps/cps) | s.d. (cps/cps) | $^{12}C/(^{12}C/^{28}Si)$ std. cor. [wt%/(cps/cps)] | s.d. [wt%/(cps/cps)] | $^{12}C$ sample (wt%) | s.d. (wt%) |
|---|---|---|---|---|---|---|---|---|---|---|---|---|
| A914 | 30 | 1500 | 6 | 4.93E+02 | 1.65E+04 | 2.56E+06 | 6.45E-03 | 2.69E-04 | 35.21 | 0.5064 | 0.2271 | 0.0100 |
| M02 | 2.08 | 1300 | 4 | 4.93E+02 | 3.11E+03 | 3.22E+06 | 9.70E-04 | 4.66E-05 | 35.18 | 0.5186 | 0.0341 | 0.0017 |
| M12 | 3.06 | 1400 | 3 | 4.93E+02 | 3.31E+03 | 3.58E+06 | 9.25E-04 | 3.61E-05 | 35.16 | 0.5309 | 0.0325 | 0.0014 |
| M13 | 3.08 | 1300 | 6 | 4.93E+02 | 4.75E+03 | 3.68E+06 | 1.30E-03 | 6.94E-05 | 35.13 | 0.5431 | 0.0455 | 0.0025 |
| M10b | 3.057 | 1250 | 6 | 4.93E+02 | 4.31E+03 | 3.59E+06 | 1.21E-03 | 2.22E-05 | 35.11 | 0.5553 | 0.0423 | 0.0010 |
| M09 | 4.92 | 1300 | 6 | 4.93E+02 | 8.02E+03 | 2.94E+06 | 2.74E-03 | 9.82E-05 | 35.08 | 0.5676 | 0.0960 | 0.0038 |
| A897 | 20 | 1500 | 6 | 4.93E+02 | 4.99E+04 | 3.93E+06 | 1.27E-02 | 5.86E-04 | 35.05 | 0.5798 | 0.4462 | 0.0218 |
| A951 | 20 | 1600 | 6 | 4.93E+02 | 5.45E+04 | 3.68E+06 | 1.49E-02 | 4.79E-04 | 35.03 | 0.5921 | 0.5218 | 0.0190 |
| A868 | 20 | 1400 | 6 | 4.93E+02 | 3.22E+04 | 3.12E+06 | 1.04E-02 | 4.71E-04 | 35.00 | 0.6043 | 0.3630 | 0.0176 |
| C398 | 10 | 1500 | 6 | 4.93E+02 | 1.51E+04 | 3.18E+06 | 4.78E-03 | 1.13E-04 | 34.97 | 0.6166 | 0.1670 | 0.0049 |

Andesite

| Run No. | P (kbar) | T (C°) | time (h) | $^{12}C$ blank (cps) | $^{12}C$ cor. sample (cps) | $^{28}Si$ cor. sample (cps) | $^{12}C/^{28}Si$ cor. sample (cps/cps) | s.d. (cps/cps) | $^{12}C/(^{12}C/^{28}Si)$ std. cor. [wt%/(cps/cps)] | s.d. [wt%/(cps/cps)] | $^{12}C$ sample (wt%) | s.d. (wt%) |
|---|---|---|---|---|---|---|---|---|---|---|---|---|
| A09b | 4.92 | 1300 | 6 | 6.97E+02 | 3.69E+03 | 3.52E+06 | 1.05E-03 | 1.12E-05 | 34.42 | 0.4414 | 0.0361 | 0.0006 |
| A07 | 2.07 | 1300 | 2+3.5 | 6.97E+02 | 1.14E+03 | 3.42E+06 | 3.35E-04 | 1.36E-05 | 35.17 | 0.4523 | 0.0118 | 0.0005 |
| A09c | 4.11 | 1300 | 6 | 6.97E+02 | 2.99E+03 | 3.06E+06 | 9.78E-04 | 3.20E-05 | 35.92 | 0.4632 | 0.0351 | 0.0012 |
| A12 | 3.05 | 1400 | 3 | 6.97E+02 | 1.70E+03 | 3.32E+06 | 5.12E-04 | 2.02E-05 | 36.67 | 0.4741 | 0.0188 | 0.0008 |
| A13b | 3.002 | 1300 | 7 | 6.97E+02 | 1.51E+03 | 2.93E+06 | 5.17E-04 | 3.17E-05 | 37.42 | 0.4850 | 0.0194 | 0.0012 |
| A955 | 30 | 1500 | 6 | 6.97E+02 | 4.30E+04 | 3.07E+06 | 1.40E-02 | 2.40E-04 | 38.17 | 0.4959 | 0.5357 | 0.0115 |
| C399 | 10 | 1500 | 6 | 6.97E+02 | 8.87E+03 | 3.51E+06 | 2.53E-03 | 9.08E-05 | 38.92 | 0.5068 | 0.0986 | 0.0038 |
| A954 | 20 | 1600 | 6 | 6.97E+02 | 2.26E+04 | 3.35E+06 | 6.74E-03 | 1.63E-04 | 39.67 | 0.5177 | 0.2674 | 0.0074 |
| A911 | 20 | 1500 | 6 | 6.97E+02 | 3.22E+04 | 4.06E+06 | 7.95E-03 | 2.26E-04 | 40.42 | 0.5286 | 0.3213 | 0.0100 |
| A04 | 3.09 | 1200 | 2 | 6.97E+02 | 1.29E+03 | 3.30E+06 | 3.88E-04 | 1.07E-04 | 41.17 | 0.5395 | 0.0160 | 0.0044 |
| A955 | 30 | 1500 | 6 | 6.97E+02 | 4.61E+04 | 3.74E+06 | 1.23E-02 | 1.43E-04 | 41.92 | 0.5504 | 0.5171 | 0.0091 |

Rhyolite

| Run No. | P (kbar) | T (C°) | time (h) | $^{12}C$ blank (cps) | $^{12}C$ cor. sample (cps) | $^{28}Si$ cor. sample (cps) | $^{12}C/^{28}Si$ cor. sample (cps/cps) | s.d. (cps/cps) | $^{12}C/(^{12}C/^{28}Si)$ std. cor. [wt%/(cps/cps)] | s.d. [wt%/(cps/cps)] | $^{12}C$ sample (wt%) | s.d. (wt%) |
|---|---|---|---|---|---|---|---|---|---|---|---|---|
| A919 | 20 | 1400 | 6 | 5.28E+02 | 1.71E+04 | 3.76E+06 | 4.54E-03 | 1.73E-04 | 89.18 | 0.0129 | 0.4049 | 0.0154 |
| A910 | 20 | 1500 | 6 | 5.28E+02 | 1.91E+04 | 3.69E+06 | 5.19E-03 | 8.55E-05 | 91.37 | 0.0263 | 0.4745 | 0.0078 |
| C394 | 30 | 1500 | 6 | 5.28E+02 | 2.54E+04 | 3.49E+06 | 7.27E-03 | 2.30E-04 | 93.57 | 0.0397 | 0.6806 | 0.0215 |
| A952 | 20 | 1600 | 6 | 5.28E+02 | 1.41E+04 | 3.42E+06 | 4.12E-03 | 1.05E-04 | 95.76 | 0.0531 | 0.3943 | 0.0101 |
| A987 | 10 | 1500 | 6 | 5.28E+02 | 6.65E+03 | 3.61E+06 | 1.84E-03 | 1.73E-05 | 97.96 | 0.0665 | 0.1802 | 0.0017 |
| R03 | 4.98 | 1300 | 2 | 5.28E+02 | 2.13E+03 | 3.07E+06 | 6.92E-04 | 9.55E-06 | 100.15 | 0.0800 | 0.0693 | 0.0010 |
| R02 | 2.08 | 1300 | 4 | 5.28E+02 | 5.03E+02 | 2.59E+06 | 1.94E-04 | 1.31E-05 | 102.35 | 0.0934 | 0.0199 | 0.0013 |
| R01 | 3.08 | 1300 | 2 | 5.28E+02 | 7.96E+02 | 2.55E+06 | 3.13E-04 | 2.25E-05 | 104.54 | 0.1068 | 0.0327 | 0.0023 |
| R04 | 3.09 | 1200 | 2 | 5.28E+02 | 7.81E+02 | 2.35E+06 | 3.32E-04 | 2.94E-05 | 106.73 | 0.1202 | 0.0355 | 0.0031 |
| R12C | 3.07 | 1400 | 3 | 5.28E+02 | 6.60E+02 | 2.43E+06 | 2.72E-04 | 2.31E-05 | 108.93 | 0.1336 | 0.0303 | 0.0026 |

*Abbreviations: cps = count per seconds. s.d. = one standard deviation. std. = standard.*

*Supplementary Table 6.S2. Oxidized carbon concentration (as $CO_2$) in the samples detected by FTIR measurements.*

| sample | P (kbar) | T (°C) | time (h) | $CO_2$ as carbonate (wt%) | s.d. (wt%) | $CO_2$ as $CO_2$ molecule (wt%) | s.d. (wt%) | Total $CO_2$ (wt%) | s.d. (wt%) |
|---|---|---|---|---|---|---|---|---|---|
| MORB | | | | | | | | | |
| M02 | 2.08 | 1300 | 4 | 0.0896 | 0.0063 | - | - | 0.0896 | 0.0063 |
| M12 | 3.06 | 1400 | 3 | 0.0752 | 0.0026 | - | - | 0.0752 | 0.0026 |
| M13 | 3.08 | 1300 | 6 | 0.1453 | 0.0020 | - | - | 0.1453 | 0.0020 |
| M09 | 4.92 | 1300 | 6 | 0.3420 | 0.0315 | - | - | 0.3420 | 0.0315 |
| A914 | 30 | 1500 | 6 | 0.6452 | 0.0119 | - | - | 0.6452 | 0.0119 |
| A951 | 20 | 1600 | 6 | 1.4233 | 0.0283 | - | - | 1.4233 | 0.0283 |
| C398 | 10 | 1500 | 6 | 0.6152 | 0.0122 | - | - | 0.6152 | 0.0122 |
| A897 | 20 | 1500 | 6 | 1.4249 | 0.0101 | - | - | 1.4249 | 0.0101 |
| Andesite | | | | | | | | | |
| A07 | 2.07 | 1300 | 2+3.5 | 0.0329 | 0.0025 | 0.0065 | 0.0012 | 0.0394 | 0.0028 |
| A09b | 4.96 | 1300 | 6 | 0.0809 | 0.0126 | 0.0082 | 0.0015 | 0.0891 | 0.0127 |
| A09c | 4.11 | 1300 | 6 | 0.0682 | 0.0034 | 0.0082 | 0.0002 | 0.0764 | 0.0034 |
| A12 | 3.05 | 1400 | 3 | 0.0541 | 0.0047 | 0.0067 | 0.0005 | 0.0609 | 0.0047 |
| A13b | 3.0002 | 1300 | 7 | 0.0522 | 0.0017 | 0.0076 | 0.0003 | 0.0598 | 0.0017 |
| A911 | 20 | 1500 | 6 | 1.0817 | 0.0342 | 0.0726 | 0.0010 | 1.1543 | 0.0342 |
| A912 | 20 | 1400 | 6 | 1.1934 | 0.0532 | 0.0870 | 0.0042 | 1.2804 | 0.0534 |
| A954 | 20 | 1600 | 6 | 0.8775 | 0.0331 | 0.0617 | 0.0041 | 0.9393 | 0.0334 |
| A955 | 30 | 1500 | 6 | 1.7325 | 0.0200 | 0.1265 | 0.0085 | 1.8590 | 0.0217 |
| C399 | 10 | 1500 | 6 | 0.4075 | 0.0199 | 0.0268 | 0.0056 | 0.4344 | 0.0207 |
| Rhyolite | | | | | | | | | |
| R01 | 3.08 | 1300 | 2 | 0.0201 | 0.0033 | 0.0649 | 0.0062 | 0.0849 | 0.0070 |
| R02 | 2.08 | 1300 | 4 | 0.0147 | 0.0004 | 0.0308 | 0.0037 | 0.0455 | 0.0037 |
| R03 | 4.98 | 1300 | 2 | 0.0447 | 0.0073 | 0.1408 | 0.0033 | 0.1855 | 0.0080 |
| R04 | 3.09 | 1200 | 2 | 0.0375 | 0.0052 | 0.0824 | 0.0018 | 0.1199 | 0.0055 |
| R12c | 3.07 | 1400 | 3 | 0.0640 | 0.0020 | 0.0623 | 0.0044 | 0.1263 | 0.0048 |
| A910 | 20 | 1500 | 6 | 0.3123 | 0.0061 | 1.2679 | 0.0226 | 1.5801 | 0.0234 |
| A919 | 20 | 1400 | 6 | 0.3133 | 0.0072 | 1.1274 | 0.0201 | 1.4408 | 0.0214 |
| A952 | 20 | 1600 | 6 | 0.2071 | 0.0055 | 0.9051 | 0.0080 | 1.1122 | 0.0098 |
| C394 | 30 | 1500 | 6 | 0.6108 | 0.0157 | 1.5488 | 0.1054 | 2.1596 | 0.1065 |
| A987 | 10 | 1500 | 6 | 0.1276 | 0.0155 | 0.4743 | 0.0177 | 0.6019 | 0.0235 |

*s.d. = one standard deviation*

*$CO_2$ molecule bands were not observed in the MORB composition glasses.*

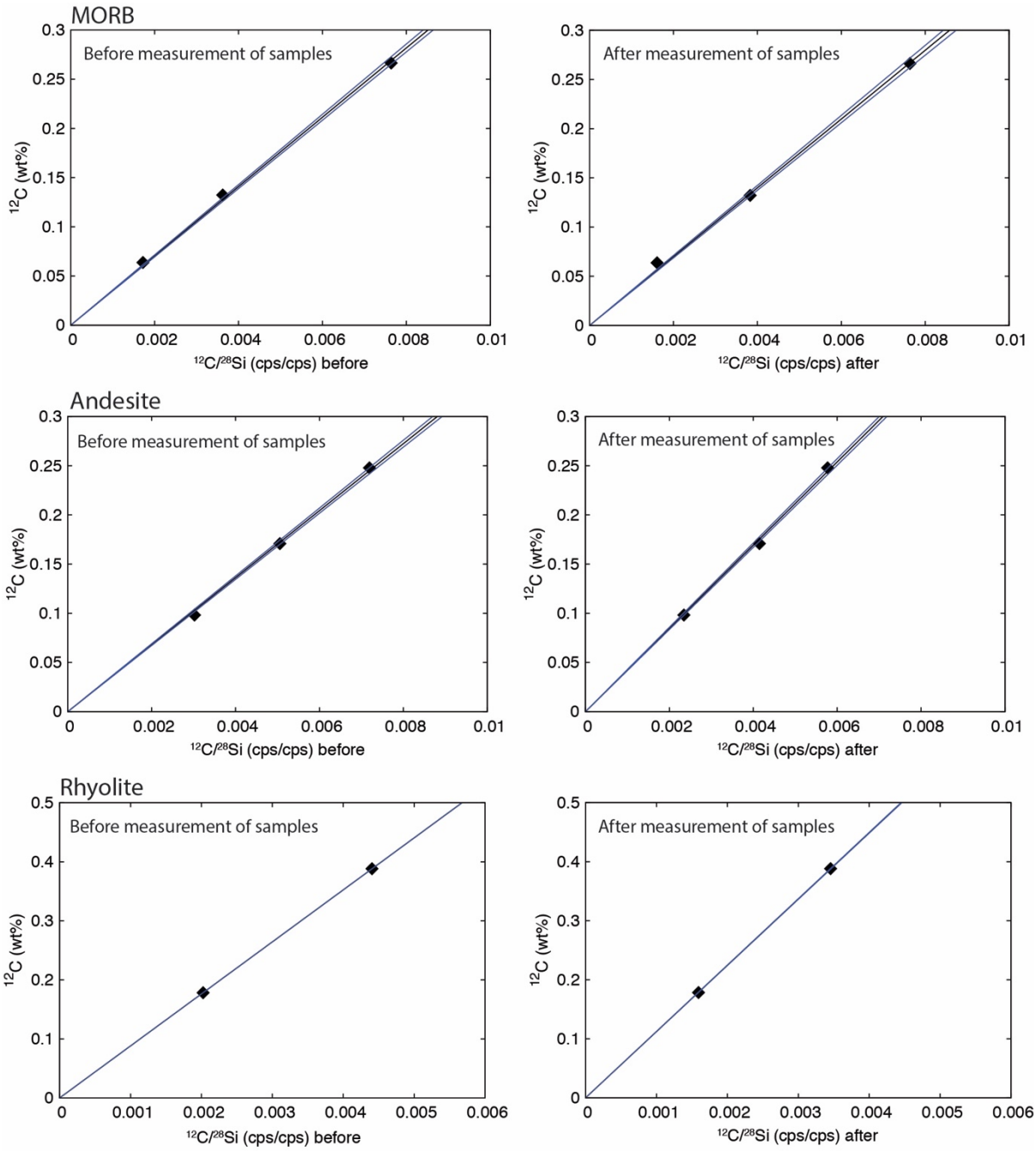


*Supplementary Fig. 6.S1. The SIMS calibration for each composition of glasses, using synthetic carbon-doped glasses. Carbon contents of the glasses were measured by FTIR. The gray lines show the standard error (1σ) of the calibration curve. The transition of the calibration line through the analyses were considered on evaluation of carbon concentration in the glass samples.*

## 6.3.

# Nitrogen solubility in the deep mantle and the origin of Earth's primordial nitrogen budget

Takahiro Yoshioka [a], Michael Wiedenbeck [b], Svyatoslav Shcheka [a], Hans Keppler [a,*]

[a] *Bayerisches Geoinstitut, Universität Bayreuth, 95440 Bayreuth, Germany*

[b] *GFZ German Research Centre for Geosciences, 14473 Potsdam, Germany*

## *6.3.1. Abstract*

The solubility of nitrogen in the major minerals of the Earth's transition zone and lower mantle (wadsleyite, ringwoodite, bridgmanite, and Ca-silicate perovskite) coexisting with a reduced, nitrogen-rich fluid phase was measured. Experiments were carried out in multi-anvil presses at 14 to 24 GPa and 1100 to 1800°C close to the Fe–FeO buffer. Starting materials were enriched in $^{15}N$ and the nitrogen concentrations in run products were measured by secondary ion mass spectrometry. Observed nitrogen ($^{15}N$) solubilities in wadsleyite and ringwoodite typically range from 10 to 250 µg/g and strongly increase with temperature. Nitrogen solubility in bridgmanite is about 20 µg/g, while Ca-silicate perovskite incorporates about 30 µg/g under comparable conditions. Partition coefficients of nitrogen derived from coexisting phases are $D_N^{\text{wadsleyite/olivine}} = 5.1 \pm 2.1$, $D_N^{\text{ringwoodite/wadsleyite}} = 0.49 \pm 0.29$, and $D_N^{\text{bridgmanite/ringwoodite}} = 0.24\ (+0.30/-0.19)$. Nitrogen solubility in the solid, iron-rich metal phase coexisting with the silicates was also measured and reached a maximum of nearly 1 wt.% $^{15}N$ at 23 GPa and 1400 °C. These data yield a partition coefficient of nitrogen between iron metal and bridgmanite of $D_N^{\text{metal/bridgmanite}} \sim 98$, implying that in a lower mantle containing about 1% of iron metal, about half of the nitrogen still resides in the silicates. The high nitrogen solubility in wadsleyite and ringwoodite may be responsible for the low nitrogen concentrations often observed in ultradeep diamonds from the transition zone. Overall, the solubility data suggest that the transition zone and the lower mantle have the capacity to store at least 33 times the mass of nitrogen presently residing in the atmosphere. By combining the nitrogen solubility data in minerals with data on nitrogen solubility in silicate melts,

* Corresponding author.
E-mail adress: hans.keppler@uni-bayreiuth.de (H. Keppler)

mineral/melt partition coefficients of nitrogen can be estimated, from which the behavior of nitrogen during magma ocean crystallization can be modeled. Such models show that if the magma ocean coexisted with a primordial atmosphere having a nitrogen partial pressure of just a few bars, several times the current atmospheric mass of nitrogen must have been trapped in the deep mantle. It is therefore plausible that the apparent depletion of nitrogen relative to other volatiles in the near-surface reservoirs reflects the storage of a larger reservoir of nitrogen in the solid Earth. Dynamic exchange between these reservoirs may have induced major fluctuations of bulk atmospheric pressure over Earth's history.
**Keywords:** nitrogen, mantle, atmospheric pressure, magma ocean, volatiles

## *6.3.2. Introduction*

Earth's atmosphere consists mostly of nitrogen (78 vol.%, equivalent to $3.87 \cdot 10^{18}$ kg $N_2$) and traditionally, the atmosphere has been regarded as the main nitrogen reservoir on our planet (e.g. Hall, 1999). However, for Venus, which in many aspects is similar to Earth, the mass of nitrogen in the atmosphere is about three times larger (Johnson and Goldblatt, 2015). This is one of several lines of evidence suggesting that either nitrogen is anomalously depleted on Earth (Marty, 2012), or a major nitrogen reservoir may reside somewhere within Earth's interior (Johnson and Goldblatt, 2015). The existence of such a deep nitrogen reservoir would imply that bulk atmospheric pressure may have fluctuated significantly in the geologic past, with important implications for climate and habitability. High nitrogen partial pressures may enhance the greenhouse effect by broadening the infrared absorption bands of greenhouse gases (Goldblatt et al., 2009). Evidence for a dynamic exchange between the atmosphere and Earth's interior comes from data on nitrogen fluxes in subduction zones. The present day nitrogen flux into the mantle at subduction zones has been estimated to be about three times larger than nitrogen outgassing at midocean ridges, arc and intraplate volcanoes (Busigny et al., 2011), although there is some controversy about the efficiency of nitrogen subduction into the deep mantle (Busigny et al., 2003; Elkins et al., 2006; Halama et al., 2010, 2014; Mikhail et al., 2017; Mallik et al., 2018). Nitrogen transfer rates into the mantle are probably high enough to allow a complete recycling of all atmospheric nitrogen into the

mantle over the history of the Earth (Busigny et al., 2011), perhaps even several times (Johnson and Goldblatt, 2015). Direct evidence for possible fluctuations in atmospheric pressure over geologic time is sparse and contradictory (e.g. Marty et al., 2013; Som et al., 2016).

In general, data on current-day nitrogen abundances become increasingly uncertain with depth in the solid Earth. Sediments may contain several 100 µg/g of nitrogen, which is mostly ammonium ($NH_4^+$) of biological origin (e.g. Karl et al., 1997). The average nitrogen concentration of about 120 µg/g in the continental crust is constrained by direct sampling, mostly of the upper crust, and translates into $1.7 \cdot 10^{18}$ kg N (Johnson and Goldblatt, 2015). However, the nitrogen budget of Earth's mantle is rather uncertain and the amount of nitrogen residing in the core is largely unknown. Virtually all available mantle samples (xenoliths and mantle derived magmas) are likely degassed and may have lost a significant part of their initial volatile budgets. Estimates of nitrogen abundances are therefore often based on observed $N_2/^{40}Ar$ ratios (Marty, 1995). The overall mantle abundance of $^{40}Ar$, a decay product of $^{40}K$, can be relatively well estimated from the abundance of K in the mantle, corrected for losses to the atmosphere. Estimated nitrogen abundances for the upper mantle range from fractions of a µg/g (e.g. 0.27 ± 0.16 µg/g, Marty and Dauphas, 2003) to a few µg/g (e.g. Cartigny et al., 2001; Johnson and Goldblatt, 2015). While these numbers appear low, it is important to note that 1 µg/g of N in the entire mantle would already be equivalent to one atmospheric mass of nitrogen. Direct data on nitrogen contents in the transition zone and the lower mantle are lacking. Overall, the available evidence suggests that either nitrogen is depleted on Earth relative to other volatiles, such as carbon or water (Marty, 2012), or most of the nitrogen presently resides within the solid Earth (Johnson and Goldblatt, 2015). Partitioning of some nitrogen into the core appears feasible based on a number of experimental studies that suggest a siderophile behavior of nitrogen during core formation (Kadik et al., 2013; Roskosz et al., 2013; Li et al., 2016). However, under all conditions studied, the observed metal/silicate partition coefficient for N is much smaller than for C. Therefore, if core formation had significantly affected the nitrogen budget, it would have depleted C relative to N (Dalou et al., 2017), which is not consistent with observation. While there may be a significant reservoir of N in the core, it is likely much smaller than what is estimated from a bulk core–mantle equilibrium model (Johnson and Goldblatt, 2015) due to the lack of equilibration between metal and silicate in the late stages of core formation (Rubie et al.,

2015). It therefore appears plausible that the mantle could represent the largest reservoir of N in the solid Earth.

Early experimental studies have shown that a variety of ammonium-bearing silicates can be synthesized at high pressures (Watenphul et al., 2009, 2010). These data imply that the $NH_4^+$ ion readily replaces $K^+$ in many silicates (see also Honma and Itihara, 1981; Bebout and Fogel, 1992). Stabilizing $NH_4^+$ in the mantle, however, requires quite reducing conditions, with oxygen fugacities near or below the Fe–FeO buffer. Li et al. (2013) reported the first study of nitrogen solubility in the upper mantle minerals olivine, pyroxenes, and garnet in equilibrium with a nitrogen-rich fluid phase. Nitrogen solubilities generally increase with pressure and under more reducing conditions, reaching values near 100 μg/g in aluminous orthopyroxenes at 1.5 GPa and at the Fe–FeO oxygen fugacity buffer. Compared to pyroxenes, solubilities in forsterite are lower. According to Li and Keppler (2014), ammonia $NH_3$ is the main nitrogen species in aqueous fluids coexisting with mantle minerals under Fe–FeO buffer conditions. The data of Li et al. (2013) suggest that the upper mantle alone has the capacity to store 20–50 times more nitrogen than presently resides in the atmosphere.

The purpose of the present study is to provide the first experimental constraints on the nitrogen storage capacity of the transition zone and the lower mantle. Nitrogen solubility in wadsleyite, ringwoodite, bridgmanite, and Ca-silicate perovskite, the most abundant phases of the deep mantle, was experimentally quantified. Due to the generally reduced nature of the transition zone and the lower mantle (Frost and McCammon, 2008), all experiments were carried out at oxygen fugacities close to the Fe– FeO buffer. While the solubility data cannot give actual nitrogen concentrations in the mantle, they provide upper limits and can constrain the equilibrium partitioning of nitrogen between different mantle domains as well as the behavior of nitrogen upon partial melting and magma ocean crystallization.

## *6.3.3. Experimental and analytical methods*

### Starting materials and preparation of sample capsules

For the synthesis of wadsleyite, ringwoodite, and bridgmanite, stoichiometric mixtures were prepared from analytical grade $SiO_2$ and MgO. Moreover, an additional 20 wt.% $Na_2CO_3$ powder was added as a fluxing agent to enhance crystal growth during the experiment. The mixtures were homogenized for 1 h in a mortar under ethanol and then dried at 140 °C for one night. For Ca-silicate perovskite, we used a glass as starting material. A mixture with molar ratio of Ca:Si:Ti = 1:0.75:0.25 was prepared from analytical grade $CaCO_3$, $SiO_2$ and $TiO_2$. Titanium was added to avoid complete amorphization of the Ca-silicate perovskite upon decompression (Kubo et al., 1997). After decarbonation at 1100 °C, the mixture was converted into a glass by melting at 1700 °C for 30 min, followed by quenching in water.

Upon loading into sample capsules, about 10–20 wt.% $^{15}$N-labeled $^{15}NH_4{}^{15}NO_3$ (>95% $^{15}$N) was added to the starting materials (silicate mixture or glass) as a nitrogen source. The labeling with $^{15}$N was used so as to distinguish nitrogen dissolved in the sample from atmospheric contamination in the subsequent SIMS analysis. Moreover, iron metal powder (more than five times the weight of $^{15}NH_4{}^{15}NO_3$) was loaded into one end of the capsules to maintain reducing conditions close to the Fe–FeO buffer. Samples were sealed by arc welding into $Pt_{95}Rh_5$ capsules with sizes of 1.6 × 1.1 × 3.0 mm (outer diameter × inner diameter × length) or 1.2 × 1.0 × 2.4 mm.

### High-pressure experiments

We conducted a series of experiments at 14–24 GPa and 1100–1800 °C using Kawai-type multi-anvil presses with tungsten carbide cubes as secondary anvils (Supplementary Table 6.S3). Pressure calibration curves reported by Keppler and Frost (2005) were used. Experiments at 14–15, 17–19 and 21–24 GPa were carried out in a 1000-ton press with 14/8, 10/5 and 10/4 assemblies (octahedral edge length/truncation edge length in mm), respectively. Only the runs Z1383 and Z1405 were done in a 5000-ton press using a 18/11 octahedral sample assembly. The octahedral assemblies consisted of an outer

octahedral MgO pressure medium, a $ZrO_2$ sleeve, a $LaCrO_3$ heater and an inner MgO sleeve. Inside the MgO inner sleeve and below the sample, an MgO spacer was inserted for the 18/11 and 14/8 assemblies, while an $Al_2O_3$ spacer was used for the 10/5 and 10/4 assemblies. $W_{95}Re_5$–$W_{74}Re_{26}$ thermocouples were used for all experiments and were placed upon the sample inside a 4-hole $Al_2O_3$ sleeve. The MgO and $Al_2O_3$ parts were heated to 1000 °C for 45 min before the experiments to remove traces of moisture.
At the beginning of an experiment, the assembly was gradually compressed to the target pressure over about 4 h. Once the target pressure was reached, temperature was increased at a rate of 100 °C/min to the target temperature. The target temperature was kept for between 20 min and 1 h depending on the experiment. The runs were quenched to room temperature within a few seconds by switching off the electrical power. Samples were decompressed to ambient conditions over about 9 h. The recovered samples were mounted in epoxy disks and polished for analysis.

**Identification of phases and spectroscopic measurements**

Run product phases were identified by measuring Raman spectra with a confocal LabRAM HR 800 UV Raman spectrometer in backscatter geometry using the 514.5 nm line of an argon ion laser at 200 mW output power. To avoid beam damage and the amorphization of phases, an optical attenuator was used to reduce the beam intensity on the sample by a factor of ten. To further verify phase identification, powder X-ray diffraction patterns were also collected from some opened sample capsules without further grinding of the sample (Bruker D8 DISCOVER micro-focus X-ray diffractometer). In order to constrain the solubility mechanism of nitrogen, FTIR spectra were measured on doubly polished slices (thickness about 100 μm) of some samples. Measurements were carried out with a Bruker IFS 120 HR spectrometer coupled to a Bruker A 490 microscope with an all-reflecting, Cassegranian optics. A globar light source, KBr beam splitter and a narrow-band MCT detector were used. Several hundred scans were accumulated with 4 $cm^{-1}$ resolution on spot sizes of 20–50 μm.

**Electron microprobe analysis**

A JEOL JXA-8200 electron microprobe was used to measure major element compositions of all phases as well as the nitrogen content in the iron metal. For major element analyses, an acceleration voltage of 15 kV and a beam current of 15 nA with a 5 µm defocused beam were used. Counting times were 20 s on peak and 10 s on background. Albite (Na, Al), diopside (Mg, Si, Ca), $MnTiO_3$ (Ti), and andradite (Fe) were used as standards for the analysis of silicate phases. Pure Fe, Pt, and Rh were used as reference for the analysis of iron metal. Nitrogen measurements were carried out at 10 kV and 15 nA with a 5 µm defocused beam in order to avoid nitrogen evaporation during analysis. Titanium nitride (TiN) was used as standard. A blank sample (pure iron metal) was also measured. Counting times were 20 s on peak and 10 s on background. About 10 points for each sample and 6 points for the TiN standard and blank sample were analyzed. Nitrogen concentrations in the samples were calculated using the averaged count rates (cps: count per second) for the samples, for the TiN standard and for the blank sample according to the equation

$$\frac{C_N^{TiN}}{\left(cps_N^{TiN} - cps_N^{blank}\right)} = \frac{C_N^{sample}}{\left(cps_N^{sample} - cps_N^{blank}\right)}$$

where $C_N^{TiN}$ and $C_N^{sample}$ are nitrogen concentration (wt.%) in TiN and sample, respectively. $cps_N^{TiN}$, $cps_N^{sample}$ and $cps_N^{blank}$ are cps for TiN, sample and blank sample, respectively. This procedure is necessary because of the strongly curved background at the position of the nitrogen X-ray lines. Moreover, it makes the implicit assumption that the X-ray absorption by Ti in the TiN standard is similar to the absorption by the iron matrix in the samples studied.

**Secondary ion mass spectrometry (SIMS)**

SIMS measurements were carried out with the Cameca 1280-HR at GFZ Potsdam. Samples were embedded in epoxy, cleaned with high-purity ethanol in an ultrasonic bath and coated with a 35 nm thick high-purity gold coating. A $^{16}O^-$ primary ion beam was

focused to a ~10 μm diameter spot with a 13 kV acceleration voltage and 20–24 nA primary current. The mass resolution was set at ~2500. In one measurement cycle, signals of $^{28}Si_2^+$, $^{14}N^-$ and $^{15}N^-$ (Fig. 6.14) were collected for 1, 2 and 6 s, respectively. As calibration materials, we used $^{15}N$-implanted enstatite for bridgmanite and Ca-silicate perovskite, and $^{15}N$-implanted forsterite for the other minerals. These calibrants were chosen because of their compositional similarity to the samples and because they arestable under the ion beam and during ion implantation, while the high-pressure phases easily become amorphous. A maximum dose density equivalent to 51 μmol/mol $^{15}N$ in the forsterite and 501 μmol/mol in the enstatite was implanted 200 nm below the surface (see Li et al., 2013 for a detailed description). At the start and the end of each session, the relevant calibrant was measured in depth profiling mode. No pre-sputtering was used. An average value from 10 cycles around the highest $^{15}N$ count was taken as the implanted $^{15}N$ concentration. Synthetic buddingtonite with natural isotopic composition was also measured under the same condition as used for the ion-implants in order to estimate nitrogen interference from the atmosphere in the samples (see the equation below). Analyses of the samples were carried out in spot mode after pre-sputtering on an area of 20 μm diameter for 60 s. Signals were collected for 40 cycles. The nitrogen concentrations in the samples were calculated using the equations

$$\frac{C_{^{15}N}^{std}/(cps_{^{15}N^+}^{std} - cps_{^{15}N^+}^{std\_atm})}{C_{^{28}Si}^{std}/cps_{^{28}Si^{2+}}^{std}} = \frac{C_{^{15}N}^{sample}/(cps_{^{15}N^+}^{sample} - cps_{^{15}N^+}^{sample\_atm})}{C_{^{28}Si}^{sample}/cps_{^{28}Si^{2+}}^{sample}}$$

$$\frac{cps_{^{15}N^+}^{bud}}{cps_{^{14}N^+}^{bud}} = \frac{cps_{^{15}N^+}^{std\_atm}}{cps_{^{14}N^+}^{std}} = \frac{cps_{^{15}N^+}^{sample\_atm}}{cps_{^{14}N^+}^{sample}}$$

where $C_B^A$ is concentration of B in A, $cps_B^A$ is cps of B in A and $cps_B^{A\_atm}$ is cps of the atmospheric B interference in A. We assumed that the $^{14}N$ detected in our samples is all of atmospheric origin and the corresponding concentration of $^{15}N^+$ was subtracted from the entire $^{15}N^+$ concentration using data from buddingtonite. Measurements in which the detected cps were not stable through all cycles were discarded.

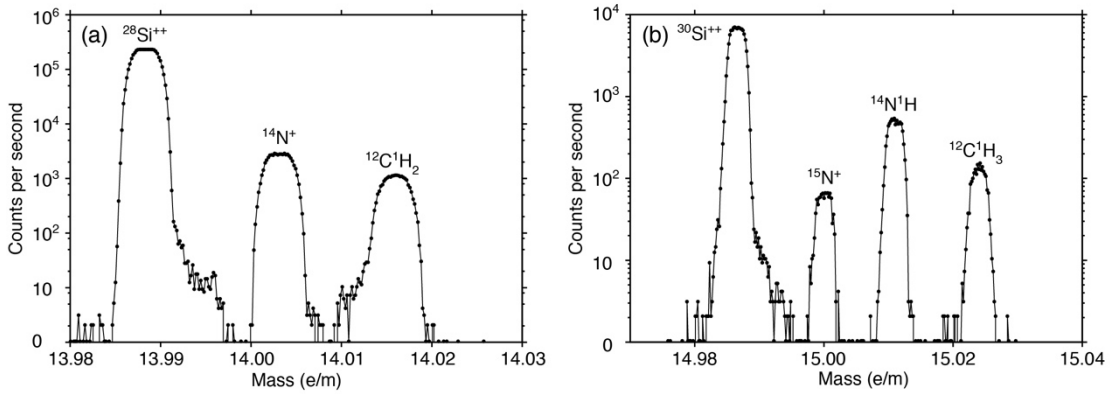


*Fig. 6.14 . SIMS mass spectra of species around peaks for (a) $^{28}Si_2^+$, $^{14}N$ and (b) $^{15}N$. Data were acquired with a M/ΔM ≈ 4000 for (a) and a M/ΔM ≈ 5500 for (b) on a synthetic buddingtonite crystal with natural nitrogen isotopic composition.*

## *6.3.4. Results*

### Description of run products

Table 6.5 summarizes the results of the high-pressure experiments; additional data and microprobe analyses of individual minerals are compiled in Supplementary Tables 6.S3 and 6.S4. In all experiments, silicate phases coexisted with metallic iron and FeO. Fine-grained quench crystals that likely precipitated from a fluid upon cooling were sometimes observed. Fig. 6.15 shows typical BSE (back scattered electron) images of the recovered samples. Due to alloying with the platinum capsule, the iron metal contained some Pt, while the FeO phase often incorporated some Mg and the Fe content of the silicate phases was elevated relative to the starting composition. However, the magnesium numbers of the silicate phases overlap well with those expected in the mantle (Table 6.5; Supplementary Table 6.S4). Ideally, the oxygen fugacity of these runs should have been buffered at Fe–FeO. Diluting the Fe phase with Pt will increase oxygen fugacity, while diluting the FeO by MgO reduces oxygen fugacity. As a first approximation, we will assume that both effects roughly compensated for each other and that all runs were close to the Fe–FeO buffer.

*Table 6.5. Summary of nitrogen solubility in minerals from high-pressure experiments*

| Run No. | P (GPa) | T (°C) | Duration (h) | Mineral | $^{15}N$ (µg/g) | Mg# |
|---|---|---|---|---|---|---|
| Z1045 | 16 | 1500 | 1 | Olivine | 36.9 (12.3) | 90 |
| S6348 | 14 | 1100 | 1 | Wadsleyite | 9.6 (1.2) | 91 |
| S6361 | 14 | 1300 | 1 | Wadsleyite | 13.6 (1.6) | 91 |
| S6350 | 14 | 1400 | 1 | Wadsleyite | 38.0 (10.4) | 85 |
| S6332 | 15 | 1400 | 1 | Wadsleyite | 82.0 (31.2) | 82 |
| Z1383 | 1 | 1200 | 1 | Wadsleyite | 13.4 (2.8) | 91 |
| Z1405 | 16 | 1500 | 1 | Wadsleyite | 188.8 (15.6) | 80 |
| S6519 | 17 | 1400 | 1 | Wadsleyite | 154.7 (73.5) | 82 |
| S6521 | 19 | 1400 | 1 | Wadsleyite | 91.5 (38.8) | 87 |
| S6329 | 14 | 1100 | 1 | Ringwoodite | 12.9 (0.6) | 68 |
| S6521 | 19 | 1400 | 1 | Ringwoodite | 44.5 (7.2) | 73 |
| S6579 | 21 | 1200 | 1 | Ringwoodite | 49.5 (8.7) | 77 |
| H4326 | 21 | 1400 | 1 | Ringwoodite | 94.8 (26.0) | 76 |
| H4327 | 21 | 1600 | 1 | Ringwoodite | 104.5 (19.6) | 76 |
| S6571 | 23 | 1400 | 1 | Ringwoodite | 57.6 (15.7) | 78 |
| S6523 | 23 | 1800 | 1/3 | Ringwoodite | 110.4 (109.8) | 79 |
| S6543 | 24 | 1600 | 1 | Ringwoodite | 90.8 (37.5) | 82 |
| S6543 | 24 | 1600 | 1 | Bridgmanite | 21.5 (18.0) | 97 |
| S6550 | 24 | 1600 | 1 | Ca-perovskite | 11.8 (1.1) | - |
| S6564 | 24 | 1600 | 1 | Ca-perovskite | 44.9 (24.0) | - |

*Numbers in parentheses are one standard deviation. Mg# is the magnesium number, i.e. the molar ratio of Mg/(Mg+Fe) in the respective mineral. Full details of mineral compositions, including coexisting phases, as well as nitrogen concentrations measured on individual spots are compiled in Supplementary Tables 6.S3 and 6.S4. Note that solubilities are given in µg/g of $^{15}N$; to convert to isotopically normal nitrogen, multiply with (14.01/15), where 14.01 g/mol is the atomic weight of normal N.*

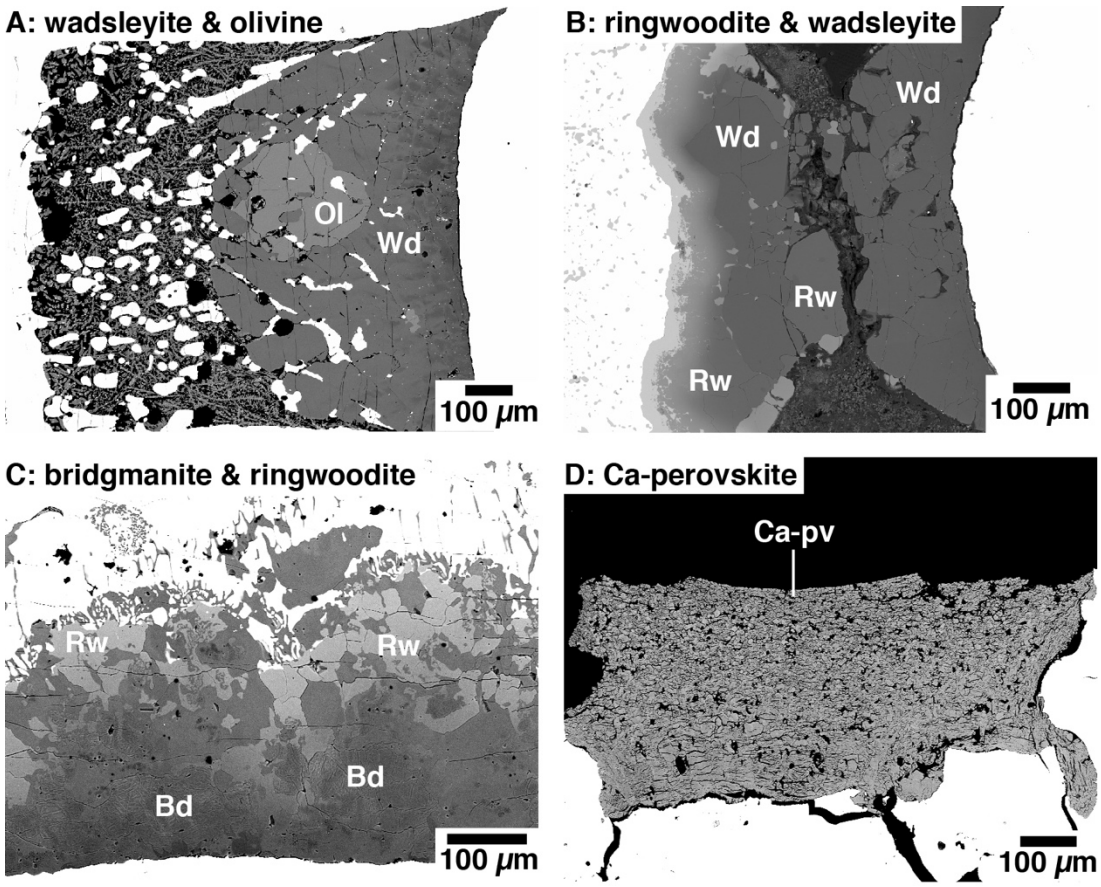


*Fig. 6.15. Selected back-scattered electron images of run products. A: Wadsleyite and olivine synthesized at 16 GPa and 1500 °C for 1 h (run Z1405). B: Ringwoodite and wadsleyite synthesized at 19 GPa and 1400 °C for 1 h (S6521). C: Bridgmanite and ringwoodite synthesized at 24 GPa and 1600 °C for 1 h (S6543). D: Ca-silicate perovskite synthesized at 24 GPa and 1600 °C for 1 h (S6550).*

In the following sections and in Supplementary Table 6.S3, all measured nitrogen concentrations are reported as μg/g of $^{15}N$, since this was the isotope added to the experimental charges. The nitrogen contents observed in the silicate phases and in iron metal were always much smaller than the bulk amount of nitrogen loaded into the capsule; thus, all minerals must have crystallized in the presence of a nitrogen-rich fluid phase. For some experiments, significant variations in nitrogen content were observed within the same mineral. This may indicate that some crystals already had formed before the nitrogen in the fluid had reached equilibrium with the Fe–FeO redox buffer, since nitrogen solubility in minerals is very sensitive to redox state (Li et al., 2013).

**Nitrogen in transition zone minerals**

Data on nitrogen solubility in wadsleyite and ringwoodite, the most abundant phases in the mantle's transition zone, are shown in Fig. 6.16. The measurements of wadsleyite synthesized at 14–19 GPa and 1100–1500 °C (Fig. 6.16a and 6.16b) clearly show that nitrogen solubility increases with both temperature and pressure. At 1500 °C and 16 GPa, 188.8 ± 15.6 µg/g $^{15}N$ were detected, whereas only 13.4 ± 2.8 µg/g were found at 1200 °C and 16 GPa. A regression fit (Fig. 6.17) of the measured nitrogen solubility in wadsleyite yields

$$\ln c_N = 11.2 - 1.67 \cdot 10^4\, T^{-1} + 0.194\, P \qquad (R^2 = 0.84)$$

where $c_N$ is nitrogen solubility in µg/g of $^{15}N$, T is temperature in Kelvin and P is pressure in GPa.

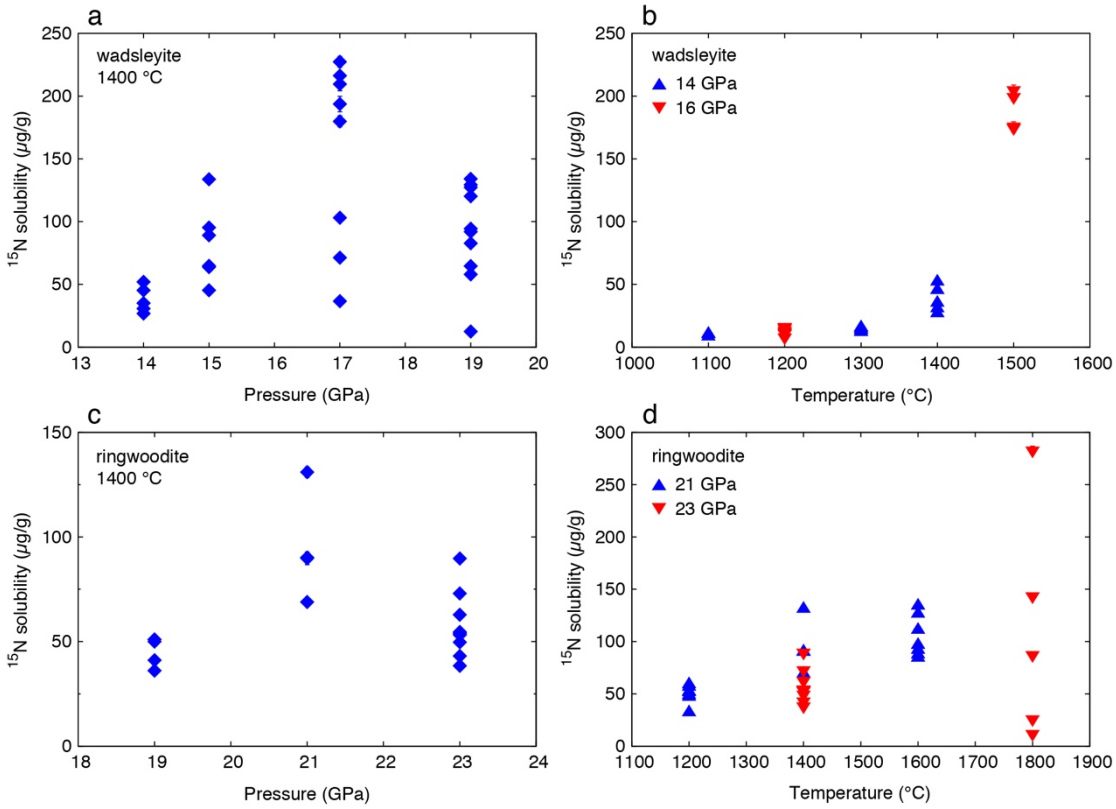


*Fig. 6.16. Nitrogen solubility in the transition zone minerals wadsleyite (a,b) and ringwoodite (c,d) as a function of pressure and temperature. Every point refers to one single measurement on one spot of the sample; uncertainties shown are one standard deviation, but usually they are smaller than the size of the symbol.*

In run Z1405, wadsleyite and olivine coexisted at 16 GPa and 1500 °C. Measured nitrogen concentrations in wadsleyite and olivine were 188.8 ± 15.6 µg/g and 36.9 ± 12.3 µg/g, respectively. These data yield a nitrogen partition coefficient between wadsleyite and olivine of $D_N^{\text{wadsleyite/olivine}} = 5.1 \pm 2.1$.

Nitrogen solubility in ringwoodite synthesized at 14–24 GPa and 1100–1800 °C increases with temperature, whereas pressure was found to have only a minor effect (Fig. 6.16c and 6.16d). At 21 GPa, the solubility is 49.5 ± 8.7 µg/g $^{15}N$ at 1200 °C, but 104.5 ± 19.6 µg/g at 1600 °C. The large scatter of the data at 1800◦C and 23 GPa (run S6523) may be due to variations in oxygen fugacity and/or nitrogen speciation in the fluid during the experiment, which may have been aggravated by the progressive alloying of Fe and Pt metal during the experiment.

A regression fit (Fig. 6.17) of the measured nitrogen solubility in ringwoodite without the data of run S6523 yields

$$\ln c_N = 5.05 - 5.21 \cdot 10^3\, T^{-1} + 0.104\, P \qquad (R^2 = 0.86)$$

In run S6521, ringwoodite and wadsleyite coexisted at 19 GPa and 1400 °C. Nitrogen concentration in ringwoodite and wadsleyite from this sample were 44.5 ± 7.2 µg/g and 91.5 ± 38.8 µg/g, respectively. This yields a nitrogen partition coefficient between ringwoodite and wadsleyite of $D_N^{\text{ringwoodite/wadsleyite}} = 0.49 \pm 0.29$.

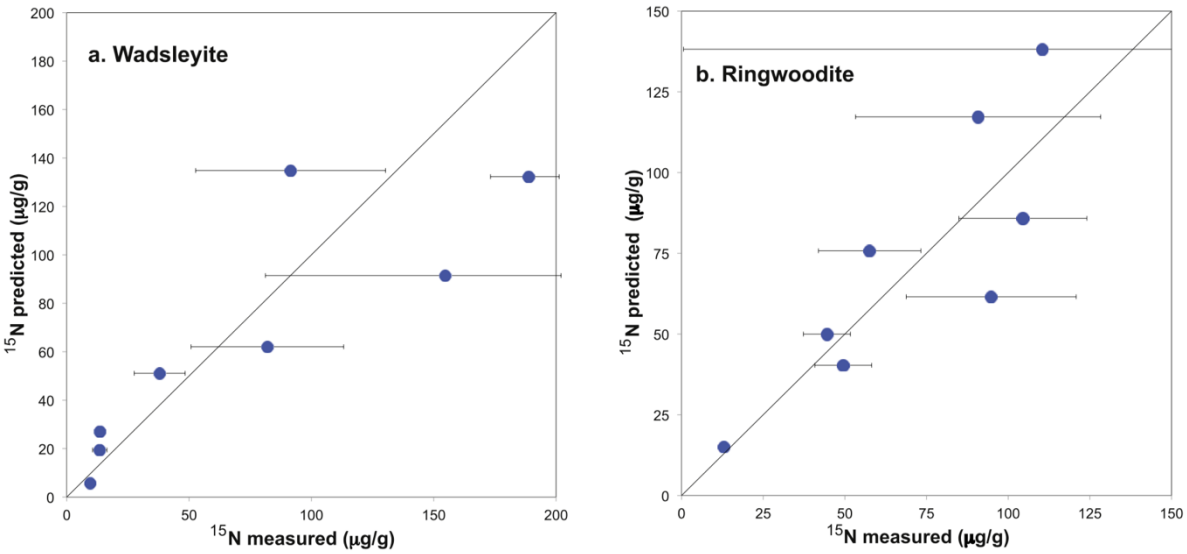


*Fig. 6.17. Comparison of the average measured nitrogen solubility in (a) wadsleyite and (b) ringwoodite with that predicted by the regression equations given in the text. Uncertainty bars are one standard deviation.*

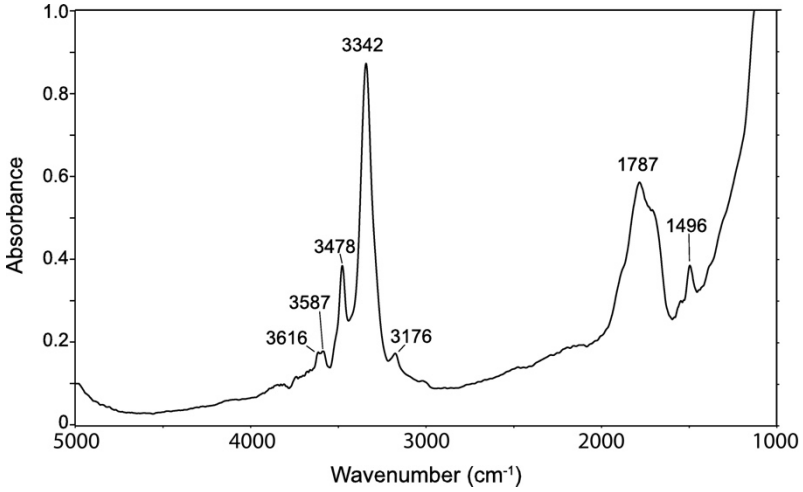


*Fig. 6.18. Unpolarized infrared spectrum of nitrogen-bearing wadsleyite (sample S6332 synthesized a 15 GPa and 1400 °C, thickness 92 μm). The band at 3176 cm$^{-1}$ is not seen in nitrogen-free hydrous wadsleyite (Jacobsen et al., 2005) and may be due to the stretching mode of an N–H species.*

Since the observed nitrogen solubilities in wadsleyite and ringwoodite are rather high, some samples were also studied in detail by Raman and infrared spectroscopy so as to constrain the dissolution mechanism of nitrogen. The clearest evidence was found in the infrared spectra of wadsleyite (Fig. 6.18). They show a band at 3176 cm$^{-1}$, which is not observed in nitrogen-free, hydrous wadsleyite (Jacobsen et al., 2005). This band may be due to the stretching vibration of some N–H species; possibly, the band at 1496 cm$^{-1}$ is the corresponding bending vibration, although the latter band could also be an overtone of a lattice vibration. Plausible nitrogen species could be the ammonium ion ($NH_4^+$ ) substituting for $Mg^{2+}$, or a protonated $N^{3-}$ ion directly substituting for $O^{2-}$. Distinguishing these two possibilities is not straightforward, as the stretching and bending frequencies of various N–H species are mainly controlled by the strength of hydrogen bonding, which depends on the nitrogen–oxygen distance (Lautié et al., 1976). The infrared absorbance of the wadsleyite sample in Fig. 6.18 implies a water content near 2700μg/g. This is one order of magnitude below the value expected for wadsleyite coexisting with pure water (Kohlstedt et al., 1996), implying that the coexisting fluid as very rich in nitrogen and measured nitrogen contents are indeed close to maximum solubility.

**Nitrogen in lower mantle minerals**

Nitrogen solubility was measured in bridgmanite, the most abundant phase of the lower mantle, and in Ca-silicate perovskite. The Raman measurements sometimes also showed peaks of ringwoodite within the bridgmanite phase, while the microprobe analyses were consistent with a pure bridgmanite composition. Therefore, a very minor contamination of the bridgmanite phase by ringwoodite cannot be ruled out. The X-ray diffraction patterns of the Ca-silicate perovskite phases showed broad peaks, indicating elastic strain and/or partial amorphization of the Ca-silicate perovskite structure. The small size of these crystals (<20 µm) led to large uncertainties in the SIMS measurements due in part to non-uniform surface electric field caused by cracks or grain boundaries.

At 24 GPa and 1600 °C, 21.5 ± 18.1 µg/g $^{15}$N were measured in bridgmanite, while Ca-silicate perovskite contained 28.3 ± 23.6 µg/g (Fig. 6.19). Although these data show considerable scatter, they suggest that nitrogen is less soluble in these two lower mantle minerals than in wadsleyite or ringwoodite. Indeed, in run S6543, bridgmanite and ringwoodite coexisted at 24 GPa and 1600◦C. While bridgmanite contained 21.5 ± 18.1 µg/g $^{15}$N, 90.8 ± 37.5 µg/g were found in ringwoodite. This yields a partition coefficient $D_N^{\text{bridgmanite/ringwoodite}}$ = 0.24 (+0.30/−0.19). Considering that $D_N^{\text{ringwoodite/wadsleyite}}$ = 0.49 ± 0.29, the transition zone minerals clearly have a higher capacity for storing nitrogen than bridgmanite or Ca-silicate perovskite in the lower mantle.

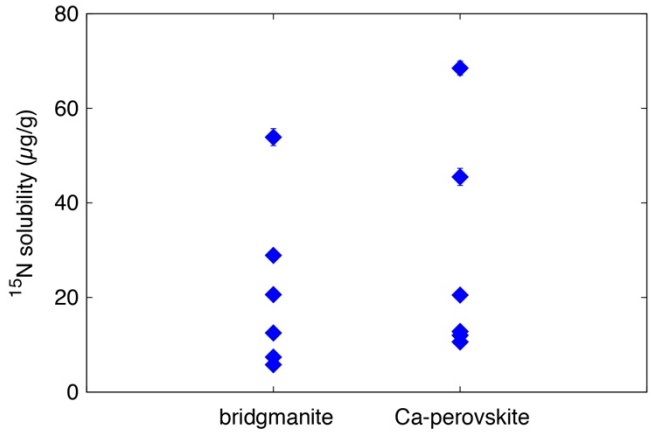


*Fig. 6.19. Nitrogen solubility in the lower mantle minerals bridgmanite and Ca-silicate perovskite. Every point refers to one single measurement on one spot of the sample; uncertainties shown are one standard deviation, but usually they are smaller than the size of the symbol.*

**Nitrogen in iron metal**

Nitrogen solubility in iron-rich metal, which coexisted with the silicate minerals, was measured by electron microprobe (Supplementary Table 6.S3). The highest nitrogen content detected was 1.04 wt.% at 23 GPa and 1400 °C. The iron-rich metal phase in some of our samples, however, contained significant amounts of platinum. This might influence nitrogen solubility in the metal phase. Therefore, we included the alloy composition in a numerical model of the data. A regression fit of all the data on nitrogen solubility in iron-rich solid metal yielded

$$\ln c_N = - 13.0 + 1.22 \cdot 10^4 T^{-1} + 0.188 P + 0.871 x_{Fe} \; (R^2 = 0.82)$$

where $c_N$ is nitrogen solubility in wt. % of $^{15}N$, T is temperature in Kelvin, P is pressure in GPa, and $x_{Fe}$ is the molar fraction of iron Fe/(Fe+Pt) in the Fe-Pt alloy. The regression fit suggests that nitrogen solubility in metal increases with pressure and $x_{Fe}$, but decreases with temperature.

## *6.3.5. Discussion*

**Comparison with previous studies**

This study reports the first data on nitrogen solubility in transition zone and lower mantle minerals. However, the data on nitrogen solubility in olivine (run Z1405) and on nitrogen solubility in iron metal may be compared to previous studies. Li et al. (2013) observed that nitrogen solubility in forsterite increased with decreasing oxygen fugacity and with increasing temperature and pressure. The highest concentrations (7.0 ± 1.6 µg/g of $^{15}N$) were observed at 3.5 GPa, 1300 °C and Fe–FeO buffer conditions. The solubility near the Fe–FeO buffer at 16 GPa and 1500 °C of 36.9 ±12.3 µg/g $^{15}N$ found in the present study is generally consistent with the trends of increasing solubility with pressure and towards more reducing conditions, as identified by Li et al. (2013).

Several studies have reported nitrogen concentrations in quenched liquid iron alloy (e.g. Roskosz et al., 2013; Kadik et al., 2013; Li et al., 2016). However, only in the study of Roskosz et al. (2013) were the samples in equilibrium with an excess nitrogen-rich gas phase and therefore only the data from this study represent true nitrogen solubilities. The data of Roskosz et al. (2013) were obtained in a laser-heated diamond cell at 1.8 to 17.7 GPa and 2500 to 2850 K, yielding nitrogen concentrations in the metal between 4.7 and 12.4 wt.%. These numbers are one order of magnitude higher than the solubilities in solid iron observed in the present study and they therefore suggest that upon crystallization of iron, nitrogen partitions preferentially into the residual liquid.

**The nitrogen storage capacity in Earth's mantle**

Li et al. (2013) estimated the nitrogen storage capacity of the upper mantle from measurements of nitrogen solubility in olivine, pyroxenes, and garnet. A similar exercise can now be done with the data from the present study for the transition zone and lower mantle. Fig. 6.20 shows nitrogen solubility in olivine, wadsleyite, ringwoodite, and lower mantle minerals along an oceanic geotherm. For the transition zone and the lower mantle a constant oxygen fugacity close to the iron wüstite buffer is assumed, while the upper mantle becomes more reducing with depth, following the model of Frost and McCammon (2008). Nitrogen solubility in olivine was recalibrated by combining the experimental data from Li et al. (2013) at 1.5 to 3.5 GPa with the single data point from run Z1405 at 16 GPa. This yields the following regression equation:

$$\ln c_N = 2.53 - 1.04 \cdot 10^4 T^{-1} + 0.246 P - 0.953 \Delta NiNiO \quad (R^2 = 0.88)$$

where $c_N$ is nitrogen solubility in µg/g of $^{15}N$, T is temperature in Kelvin, P is pressure in GPa, and ΔNiNiO is the difference in the logarithm of the oxygen fugacity to the value of the Ni-NiO buffer.

This equation gives nitrogen solubilities at the base of the upper mantle that are about an order of magnitude lower than those predicted from the model used by Li et al. (2013), which was only constrained by low-pressure data. However, as noted by these authors, throughout most of the upper mantle, pyroxenes are likely the most important host of

nitrogen. Considering this together with our new data on olivine, we will assume in the further discussion that the upper mantle may store up to 20 times the present atmospheric mass of nitrogen, which is at the lower end of the estimate given by Li et al. (2013). Most of this nitrogen would have to reside in the pyroxenes and additional experimental work would be necessary to better constrain the storage capacity of the pyroxenes in the deep part of the upper mantle. The nitrogen ($^{14}N$) solubility in olivine alone as shown in Fig. 6.20 corresponds to only 0.77 present atmospheric masses ($3.0 \cdot 10^{18}$ kg).

Nitrogen solubility in the transition zone minerals wadsleyite and ringwoodite is well constrained by the data from the present study. If one assumes the modal abundance of both minerals in their respective stability fields to be about 60%, one obtains a $^{14}N$ storage capacity for the wadsleyite and ringwoodite layer of $1.8 \cdot 10^{19}$ kg and $1.3 \cdot 10^{19}$ kg, corresponding to 4.6 and 3.4 times the present atmospheric mass, respectively. In other words, the transition zone alone may store a minimum of 8.0 atmospheric masses of nitrogen, while not even considering any possible contribution from majorite garnet. The high nitrogen solubility in wadsleyite and ringwoodite may explain why ultradeep

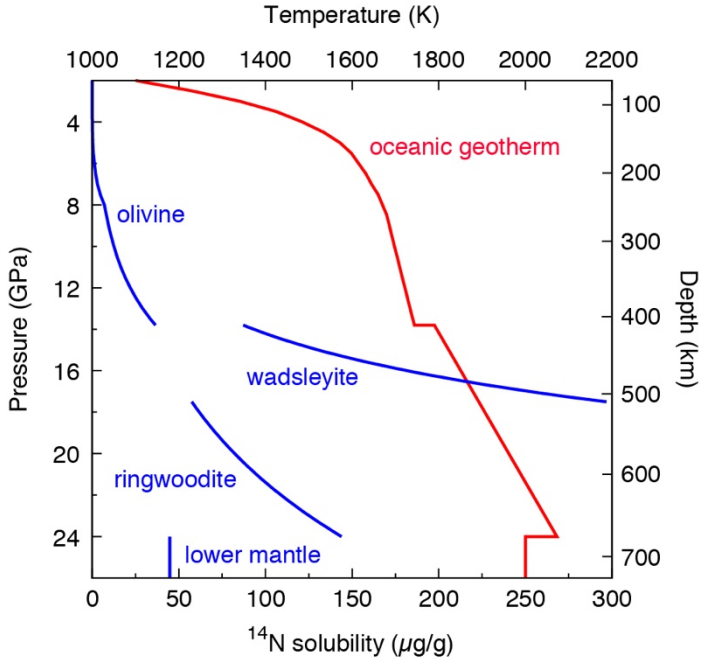


*Fig. 6.20. Nitrogen solubility in major mantle minerals as a function of pressure along an oceanic geotherm. The geotherm is from Turcotte and Schubert (2002); oxygen fugacity in the upper mantle is assumed to decrease with depth according to the model of Frost and McCammon (2008), while it is assumed to be close to the iron wüstite buffer in the transition zone and lower mantle. "Lower mantle" is the estimated bulk nitrogen solubility of the lower mantle, including bridgmanite, Ca- perovskite and iron metal.*

diamonds originating from the transition zone usually contain little nitrogen (e.g. Palot et al., 2012). The nitrogen storage capacity of the lower mantle is only constrained for the uppermost layer of this reservoir. Nitrogen solubility in bridgmanite and Ca-silicate perovskite was directly measured at 24 GPa and 1600 °C. Nitrogen solubility in metallic iron at 24 GPa and 2000 K (the temperature expected from a oceanic geotherm) is 2110 µg/g of $^{15}N$ according to the regression equation given above. For a lower mantle consisting of 70% bridgmanite, 10% Ca-silicate perovskite and 1 wt.% metal, this yields a bulk nitrogen storage capacity of $9.6 \cdot 10^{19}$ kg or 25 atmospheric masses. This number should be considered as a lower limit, since it ignores any possible contribution from ferropericlase and the possible increase of nitrogen solubility in bridgmanite and Ca-silicate perovskite with pressure and temperature, as observed for other phases. An interesting observation is that this model implies a nitrogen partition coefficient between solid metal and bridgmanite of $D_N^{metal/bridgmanite} = 98$, which means that for a lower mantle containing 1% metal, about half of the nitrogen is still retained in the silicate phases.

**The initial nitrogen budget of the Earth**

The initial budget of volatiles in the solid Earth was likely affected by processes occurring during the crystallization of a magma ocean (e.g. Elkins-Tanton, 2008). The data on nitrogen solubility in minerals obtained in the present study may be combined with experimental data on nitrogen solubility in silicate melts in order to constrain the partitioning behavior of nitrogen during magma ocean crystallization. While several studies have been looking at nitrogen solubility in melts at low to moderate pressures (e.g. Libourel et al., 2003; Kadik et al., 2013), only Roskosz et al. (2013) provide data for a pressure range overlapping with the present study. They observed that for 5 to 17.7 GPa and temperatures of 2350 to 2850 °C, nitrogen solubility in a peridotitic liquid in equilibrium with Fe metal is nearly constant at 0.6–0.8 wt.%. This behavior is consistent with the observations by Schmidt and Keppler (2002) and Niwa et al. (2013) that the solubility of argon and xenon in silicate melts reaches a plateau above 5 GPa. The reason behind this phenomenon is that gases are initially more compressible than silicate melts, such that the partial molar volume of a gas decreases with pressure until it becomes equal

the partial molar volume of the gas in the silicate liquid. Beyond this point, gas solubility in the melt cannot increase further.

Combining the nitrogen solubility data for a peridotite melt (Roskosz et al., 2013) with the data for nitrogen solubility in wadsleyite at 16 GPa and 1500 °C (189 μg/g of $^{15}N$, experiment Z1405) yields a wadsleyite/melt partition coefficient of $D_N^{\text{wadsleyite/melt}} = 0.025$ (after accounting for the mass difference between $^{15}N$ and nitrogen of average isotopic composition). Similarly, the ringwoodite data at 21 GPa and 1600 °C (104 μg/g $^{15}N$, experiment H4327) yield $D_N^{\text{ringwoodite/melt}} = 0.014$. These data should be considered as minimum values, since nitrogen solubility in both wadsleyite and ringwoodite increases with temperature. Therefore, if the data were extrapolated to the same temperature as for the nitrogen solubility in peridotite melt (Roskosz et al., 2013), higher partition coefficients would result. In any case these data indicate that nitrogen is only moderately incompatible in transition zone minerals close to Fe–FeO buffer conditions. In the following discussion, we will use a bulk mineral/melt partition coefficient for the transition zone of $D_N^{\text{transition zone/melt}} = 0.020$.

For the lower mantle, the data on nitrogen solubility in bridgmanite and Ca-silicate perovskite in Supplementary Table 6.S3 combined with the melt solubility data of Roskosz et al. (2013) yield $D_N^{\text{bridgmanite/melt}} = 0.0029$ and $D_N^{\text{Ca-perovskite/melt}} = 0.038$. For further discussion, we assume a bulk mineral/melt partition coefficient for the lower mantle of $D_N^{\text{lower mantle/melt}} = 0.0030$, consistent with a modal abundance of 10% Ca-silicate perovskite. For the upper mantle, Li et al. (2013) estimated mineral/melt partition coefficients for olivine and pyroxenes. Assuming a simplified modal composition of 60% olivine and 40% pyroxenes, the data of Li et al. (2013) yield a bulk mineral/melt partition coefficient of nitrogen for the upper mantle of $D_N^{\text{upper mantle/melt}} = 0.0073$ at Fe–FeO buffer conditions.

The initial nitrogen concentration in the magma ocean was defined by the equilibrium with the primordial atmosphere. Libourel et al. (2003) measured the solubility of nitrogen in a basaltic melt at low pressure. Close to the Fe–FeO buffer, they observed a solubility of $N_2$ in the melt equivalent to 0.062 μg/g of N/bar (0.62 μg/g /MPa), which they attributed to the physical dissolution of $N_2$ molecules in the melt. The main problem with these data is that they were obtained in a hydrogen-free system, such that NH could not have formed. The experiments by Li et al. (2015) in a haplogranitic system showed that the solubility of nitrogen in the melt under conditions where $NH_3$ may form is about

one order of magnitude higher than for pure $N_2$. Assuming that a similar effect also occurs in more depolymerized melts, a nitrogen solubility in a (hydrous) peridotite melt near the Fe–FeO buffer of $s_{N,melt}$ = 6 µg/g N/MPa is plausible.

In a rapidly convecting magma ocean, the volatile concentrations in the liquid are likely buffered by the equilibrium with the atmosphere. Minerals therefore initially crystallize from a melt of approximately constant nitrogen content and nitrogen is sequestered into minerals according to their mineral/melt partition coefficient. With such a model, one may estimate the mass of nitrogen stored in the mantle upon crystallization as

$$m_{N,\,mantle} = s_{N,melt}\, p_N \left(D_N^{\text{upper mantle/melt}}\, m_{\text{upper mantle}} + D_N^{\text{transition zone/melt}}\, m_{\text{transition zone}} + D_N^{\text{lower mantle/melt}}\, m_{\text{lower mantle}}\right)$$

With the data on nitrogen solubility in silicate melt and the bulk partition coefficients discussed above, one obtains

$$m_{N,\,mantle} = 3.45 \cdot 10^{-2}\ \text{PAN}/\text{MPa} \cdot p_N$$

where PAN is the present atmospheric mass of nitrogen ($3.87 \cdot 10^{18}$ kg) and $p_N$ is the nitrogen partial pressure, which is the sum of the partial pressures of all nitrogen species (including $N_2$ and $NH_3$) in equilibrium with the magma ocean.

However, this simple model is unlikely to be realistic during the entire duration of magma ocean solidification. Above a threshold between 40–80% crystallization, the system may become too viscous for rapid convection (Costa et al., 2009; Elkins-Tanton, 2012). In this regime, individual compartments of the mantle will behave as essentially closed systems and dissolved nitrogen will be incorporated into solid minerals until the saturation level for nitrogen in these minerals is reached. Fig. 6.21 shows the amount of nitrogen that may be stored in the silicate mantle during magma ocean crystallization as a function of the nitrogen partial pressure of the coexisting atmosphere for a case where convection essentially stops at 50% crystallization and the mantle subsequently behaves as a closed system. Here, the nitrogen content sequestered into the minerals in the convecting regime is small compared to the nitrogen that is still contained in the melt at 50% crystallization, when the system essentially become closed. Therefore, ultimately 50% of the nitrogen concentration dissolved in the silicate melt in equilibrium with the atmosphere will end up in the mantle, until the storage capacity of the minerals is

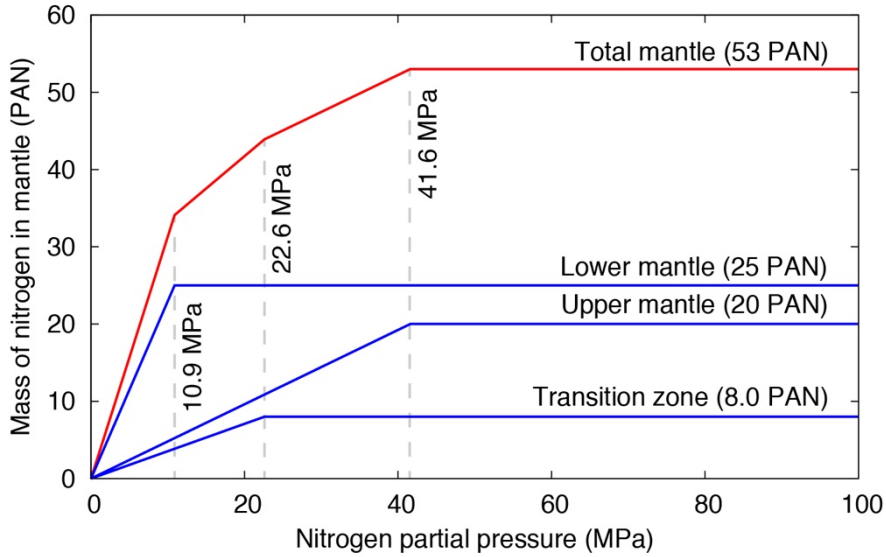


*Fig. 6.21. Mass of nitrogen stored in the mantle as function of the nitrogen partial pressure of a primordial atmosphere coexisting with the crystallizing magma ocean. The model assumes that after 50% solidification, rapid convection stops and the various domains of the mantle behave as closed systems, until the nitrogen storage capacity of the solid minerals is exceeded. PAN = Mass of present atmospheric nitrogen.*

exceeded. Above this limit, a free gas phase has to form after full crystallization and it is expected that this gas phase would be rapidly lost to the surface.

The calculations shown in Fig. 6.21 demonstrate that moderate partial pressures of nitrogen already lead to several present atmospheric masses of nitrogen being incorporated into the solidifying mantle. Constraints on plausible nitrogen partial pressures in a primordial atmosphere above a magma ocean come mostly from the nitrogen contents of chondrites that likely were the main source of terrestrial volatiles (e.g. Marty, 2012). Carbonaceous chondrites contain rather variable amounts of nitrogen (1235 ± 440 µg/g, Johnson and Goldblatt, 2015), while the nitrogen contents of enstatite chondrites fall into a much more narrow range close to 605 µg/g (Johnson and Goldblatt, 2015). There is good isotopic evidence that enstatite chondrites were the main source of nitrogen on Earth (e.g. Li et al., 2016 and references therein). If the primordial Earth contained 605 µg/g of nitrogen analogous to enstatite chondrites and if all this nitrogen had been released to the atmosphere of a planet with the same size and mass as the present Earth, the resulting nitrogen partial pressure would be 69.4 MPa. This value is simply obtained by multiplying the total mass of nitrogen in the Earth with the gravitational acceleration and dividing by the surface area of the Earth. However, a large

fraction of volatiles may have been lost already during accretion by impact degassing (e.g. Ahrens et al., 2004). The present abundances of C, H, $^{36}$Ar, and $^{84}$Kr on Earth have been estimated to be between 1.5 to 5% of the initial chondritic value (Marty, 2012). If one assumed that most of this depletion resulted from impact-induced losses and if nitrogen was similarly affected by this process, then the initial nitrogen partial pressure in the primordial atmosphere would have been in the range of 1.0–3.5 MPa. According to Fig. 6.21, this corresponds to 3.1–10.9 present atmospheric masses of nitrogen (PAN) being initially sequestered into the mantle. Obviously, this implies that most of the nitrogen may still reside in a deep, poorly sampled mantle reservoir and that nitrogen is not anomalously depleted relative to other volatiles on Earth. Note that this calculation makes the rather extreme assumptions that (i) the entire depletion of volatiles such as carbon or water is due to early impact degassing during accretion (Ahrens et al., 2004) and (ii) all this depletion took place before equilibrium between the primitive atmosphere and the magma ocean was reached. If other factors (such as carbon partitioning into the core) contributed to the depletion of volatiles, or if some depletion occurred after solidification of the magma ocean, then such estimates of the initial nitrogen partial pressure in the primordial atmosphere and the resulting mass of nitrogen stored in the mantle would increase. It therefore appears unavoidable that the solid Earth initially contained several times the present atmospheric masses of nitrogen.

**A comparison between carbon, hydrogen, and nitrogen in the deep Earth**

Both nitrogen and hydrogen may be sequestered in mantle minerals during magma ocean crystallization and for both elements, a particularly strong enrichment is expected in the transition zone (e.g. Kawamoto et al., 1996; Kohlstedt et al., 1996). For water, the existence of a deep reservoir appears to be firmly established, including direct sampling by inclusions in diamonds (e.g. Pearson et al., 2014). For nitrogen, the evidence is less compelling and estimates of bulk mantle abundances are usually based on the $N_2/^{40}$Ar ratios. For the MORB source, this ratio is near $10^2$ (Marty, 1995, 2012). However, as pointed out by Johnson and Goldblatt (2015), there is a distinct population of “high-N” mantle samples with $N_2/^{40}$Ar ratios ranging up to $10^4$ . Estimates of bulk mantle nitrogen abundances therefore critically depend on the size of the reservoirs assigned to the

MORB-like and "high-N" mantle. For a "high-N" mantle representing just 3% of the bulk mantle, Johnson and Goldblatt (2015) obtained an average nitrogen abundance in the mantle of 6 ± 4 μg/g, equivalent to 6 ± 4 PAN. This number falls within the range of primordial mantle nitrogen contents derived here, although the nitrogen budget of the mantle may have evolved over time. Compared to nitrogen and hydrogen, the behavior of carbon is fundamentally different, because (1) carbon solubility in mantle minerals is vanishingly small (Keppler et al., 2003), but (2) the metal/silicate partition coefficient of carbon is orders of magnitude higher than for N or H (Dasgupta et al., 2013; Hirschmann, 2016; Dalou et al., 2017). This means that sequestration of carbon into the silicate mantle during magma ocean crystallization is likely negligible, whereas the core may be a very important carbon reservoir. Therefore, the behavior of carbon during Earth's accretion may be modeled by considering segregation into the core and atmospheric losses alone (e.g. Hirschmann, 2016), while such a model is inappropriate for nitrogen and hydrogen. Incorporating the effect of magma ocean crystallization into models of nitrogen partitioning in the early Earth shows that the mantle may be the most important reservoir of N on the planet, implying the bulk C/N ratio of the Earth is lower than assumed in previous models and there is no need to invoke volatile delivery by objects with unusually high C/N ratios (Bergin et al., 2015; Hirschmann, 2016).

### *6.3.6. Conclusions*

The nitrogen solubility data from this study show that Earth's mantle may store at least 53 times more nitrogen than presently resides in the atmosphere. Moreover, several atmospheric masses of nitrogen must have been sequestered in the mantle during magma ocean crystallization. The existence of such a deep nitrogen reservoir implies that it is quite likely that atmospheric pressure may have fluctuated significantly over Earth's history due to an imbalance between nitrogen degassing by volcanoes and nitrogen recycling in subduction zones. Compared to other volatiles, nitrogen may not be anomalously depleted in the bulk Earth, but may simply reside in a reservoir in the deep Earth that is poorly sampled.

### *6.3.7. Acknowledgements*

This study was supported by German Research Foundation (DFG; project Ke 501/13-1). Technical support by Frédéric Couffignal (SIMS), Takaaki Kawazoe (multi-anvil experiments), Tiziana Boffa-Ballaran (X-ray diffraction), Detlef Krauße (electron microprobe), Hubert Schulze and Raphael Njul (sample preparation) is greatly appreciated. Constructive reviews by Ralf Halama and by an anonymous referee helped to improve the manuscript.

### *6.3.8. References*

Ahrens, T.J., Shen, A.H., Ni, S., 2004. Giant impact induced atmospheric blow-off. AIP Conf. Proc. 706, 1419.

Bebout, G.E., Fogel, M.L., 1992. Nitrogen-isotope compositions of metasedimentary rocks in the Catalina schist, California – implications for metamorphic devolatilization history. Geochim. Cosmochim. Acta 56, 2839–2849.

Bergin, E.A., Blake, G.A., Ciesla, F., Hirschmann, M.M., Li, J., 2015. Tracing the ingredients for a habitable Earth from interstellar space through planet formation. Proc. Natl. Acad. Sci. USA 112, 8965–8970.

Busigny, V., Cartigny, P., Philippot, P., Ader, M., Javoy, M., 2003. Massive recycling of nitrogen and other fluid–mobile elements (K, Rb, Cs, H) in a cold slab environment: evidence from HP to UHP oceanic metasediments of the Schistes Lustres nappe (western Alps, Europe). Earth Planet. Sci. Lett. 215, 27–42.

Busigny, V., Cartigny, P., Philippot, P., 2011. Nitrogen isotopes in ophiolitic metagabbros: a re-evaluation of modern nitrogen fluxes in subduction zones and implication for the early Earth atmosphere. Geochim. Cosmochim. Acta 75, 7502–7521.

Cartigny, P., Harris, J.W., Javoy, M., 2001. Diamond genesis, mantle fractionations and mantle nitrogen content: a study of δ13C–N concentrations in diamonds. Earth Planet. Sci. Lett. 185, 85–98.

Costa, A., Caricchi, L., Bagdassarov, N., 2009. A model for the rheology of particle- bearing suspensions and partially molten rocks. Geochem. Geophys. Geosyst. 10, Q03010.

Dalou, C., Hirschmann, M.M., von der Handt, A., Mosenfelder, J., Armstrong, L.S., 2017. Nitrogen and carbon fractionation during core–mantle differentiation at shallow depth. Earth Planet. Sci. Lett. 458, 141–151.

Dasgupta, R., Chi, H., Shimizu, N., Buono, A.S., Walker, D., 2013. Carbon solution and partitioning between metallic and silicate melts in a shallow magma ocean: implications for the origin and distribution of terrestrial carbon. Geochim. Cosmochim. Acta 102, 191–212.

Elkins, L.J., Fischer, T.P., Hilton, D.R., Sharp, Z.D., McKnight, S., Walker, J., 2006. Tracing nitrogen in volcanic and geothermal volatiles from the Nicaraguan volcanic front. Geochim. Cosmochim. Acta 70, 5215–5235.

Elkins-Tanton, L.T., 2008. Linked magma ocean solidification and atmospheric growth for Earth and Mars. Earth Planet. Sci. Lett. 271, 181–191.

Elkins-Tanton, L.T., 2012. Magma oceans in the inner solar system. Annu. Rev. Earth Planet. Sci. 40, 113–139.

Frost, D., McCammon, C., 2008. The redox state of Earth's mantle. Annu. Rev. Earth Planet. Sci. 36, 389–420.

Goldblatt, C., Claire, M.W., Lenton, T.M., Matthews, A.J., Watson, A.J., Zahnle, K.J., 2009. Nitrogen-enhanced greenhouse warming on early Earth. Nat. Geosci. 2, 891–896.

Halama, R., Bebout, G.E., John, T., Schenk, V., 2010. Nitrogen recycling in subducted oceanic lithosphere: the record in high- and ultrahigh-pressure metabasaltic rocks. Geochim. Cosmochim. Acta 74, 1636–1652.

Halama, R., Bebout, G.E., John, T., Scambelluri, M., 2014. Nitrogen recycling in subducted mantle rocks and implications for the global nitrogen cycle. Int. J. Earth Sci. 103, 2081–2099.

Hall, A., 1999. Nitrogen. In: Marshall, C.P., Fairbridge, R.W. (Eds.), Encyclopedia of Geochemistry. Kluwer, Dordrecht, pp. 426–428.

Hirschmann, M.M., 2016. Constraints on the early delivery and fractionation of Earth's major volatiles from C/H, C/N, and C/S ratios. Am. Mineral. 101, 540–553.

Honma, H., Itihara, Y., 1981. Distribution of ammonium in minerals of metamorphic and granitic-rocks. Geochim. Cosmochim. Acta 45, 983–988.

Jacobsen, S.D., Demouchy, S., Frost, D.J., Boffa Ballaran, T., Kung, J., 2005. A systematic study of OH in hydrous wadsleyite from polarized FTIR spectroscopy and single-crystal X-ray diffraction: oxygen sites for hydrogen storage in Earth's interior. Am. Mineral. 90, 61–70.

Johnson, B., Goldblatt, C., 2015. The nitrogen budget of Earth. Earth-Sci. Rev. 148, 150–173.

Kadik, A., Litvin, Y., Koltashev, V., Kryukova, E., Plotnichenko, V., Tsekhonya, T., Kononkova, N., 2013. Solution behavior of reduced N–H–O volatiles in FeO–$Na_2O$–$SiO_2$–$Al_2O_3$ melt equilibrated with molten Fe alloy at high pressure and temperature. Phys. Earth Planet. Inter. 214, 14–24.

Karl, D., Letelier, R., Tupas, L., Dore, J., Christian, J., Hebel, D., 1997. The role of nitrogen fixation in biogeochemical cycling in the subtropical North Pacific Ocean. Nature 388, 533–538.

Kawamoto, T., Hervig, R.L., Holloway, J.R., 1996. Experimental evidence for a hydrous transition zone in the early Earth's mantle. Earth Planet. Sci. Lett. 142, 587–592.

Keppler, H., Frost, D.J., 2005. Introduction to minerals under extreme conditions. In: Miletich, R. (Ed.), Mineral Behaviour at Extreme Conditions. In: European Mineralogical Union Lecture Notes in Mineralogy, vol. 7, pp. 1–30.

Keppler, H., Wiedenbeck, M., Shcheka, S.S., 2003. Carbon solubility in olivine and the mode of carbon storage in the Earth's mantle. Nature 424, 414–416.

Kohlstedt, D.L., Keppler, H., Rubie, D.C., 1996. Solubility of water in the α, β and γ phases of $(Mg, Fe)_2SiO_4$. Contrib. Mineral. Petrol. 123, 345–357.

Kubo, A., Suzuki, T., Akaogi, M., 1997. High pressure phase equilibria in the system $CaTiO_3$–$CaSiO_3$: stability of perovskite solid solutions. Phys. Chem. Miner. 24, 494.

Lautié, A., Froment, F., Novak, A., 1976. Relationship between NH stretching frequencies and N...O distances of crystals containing NH...O hydrogen bonds. Spectrosc. Lett. 9, 289–299.

Li, Y., Keppler, H., 2014. Nitrogen speciation in mantle and crustal fluids. Geochim. Cosmochim. Acta 129, 13–32.

Li, Y., Wiedenbeck, M., Shcheka, S., Keppler, H., 2013. Nitrogen solubility in upper mantle minerals. Earth Planet. Sci. Lett. 377, 311–323.

Li, Y., Huang, R., Wiedenbeck, M., Keppler, H., 2015. Nitrogen distribution between aqueous fluids and silicate melts. Earth Planet. Sci. Lett. 411, 218–228.

Li, Y., Marty, B., Shcheka, S., Zimmermann, L., Keppler, H., 2016. Nitrogen isotope fractionation during terrestrial core–mantle separation. Geochem. Perspect. Lett. 2, 138–147.

Libourel, G., Marty, B., Humbert, F., 2003. Nitrogen solubility in basaltic melt, part I: effect of oxygen fugacity. Geochim. Cosmochim. Acta 67, 4123–4135.

Mallik, A., Li, Y., Wiedenbeck, M., 2018. Nitrogen evolution within the Earth's atmosphere–mantle system assessed by recycling in subduction zones. Earth Planet. Sci. Lett. 482, 556–566.

Marty, B., 1995. Nitrogen content of the mantle inferred from $N_2$–Ar correlation in oceanic basalts. Nature 377, 326–329.

Marty, B., 2012. The origins and concentrations of water, carbon, nitrogen and noble gases on Earth. Earth Planet. Sci. Lett. 313, 56–66.

Marty, B., Dauphas, N., 2003. The nitrogen record of crust–mantle interaction and mantle convection from Archean to present. Earth Planet. Sci. Lett. 206, 397–410.

Marty, B., Zimmermann, L., Pujol, M., Burgess, R., Philippot, P., 2013. Nitrogen isotopic composition and density of the Archean atmosphere. Science 342, 101–104.

Mikhail, S., Barry, P.H., Sverjensky, D.A., 2017. The relationship between mantle pH and the deep nitrogen cycle. Geochim. Cosmochim. Acta 209, 149–160.

Niwa, K., Miyakawa, C., Yagi, T., Matsuda, J., 2013. Argon solubility in $SiO_2$ melt under high pressures: a new experimental result using laser-heated diamond anvil cell. Earth Planet. Sci. Lett. 363, 1–8.

Palot, M., Cartigny, P., Harris, J.W., Kaminsky, F.V., Stachel, T., 2012. Evidence for deep mantle convection and primordial heterogeneity from nitrogen and carbon stable isotopes in diamond. Earth Planet. Sci. Lett. 357–358, 179–193.

Pearson, D.G., Brenker, F.E., Nestola, F., McNeill, J., Nasdala, L., Hutchison, M.T., Matveev, S.S., Mather, K., Silversmit, G., Schmitz, S., Vekemans, B., Vincze, L., 2014. Hydrous mantle transition zone indicated by ringwoodite included within diamond. Nature 507, 221–224.

Roskosz, M., Bouhifd, M., Jephcoat, A., Marty, B., Mysen, B., 2013. Nitrogen solubility in molten metal and silicate at high pressure and temperature. Geochim. Cosmochim. Acta 121, 15–28.

Rubie, D.C., Jacobson, S.A., Morbidelli, A., O'Brien, D.P., Young, E.D., de Vries, J., Nimmo, F., Palme, H., Frost, D.J., 2015. Accretion and differentiation of the terrestrial planets with implications for the compositions of early-formed Solar System bodies and accretion of water. Icarus 248, 89–108.

Schmidt, B.C., Keppler, H., 2002. Experimental evidence for high noble gas solubilities in silicate melts under mantle pressures. Earth Planet. Sci. Lett. 195, 277–290.

Som, S.M., Buick, R., Hagadorn, J.W., Blake, T.S., Perreault, J.M., Harnmeijer, J.P., Catlin, D.C., 2016. Earth's air pressure 2.7 billion years ago constrained to less than half of modern levels. Nat. Geosci. 9, 448–452.

Turcotte, D.L., Schubert, G., 2002. Geodynamics. Cambridge University Press, NewYork.

Watenphul, A., Wunder, B., Heinrich, W., 2009. High-pressure ammonium-bearing silicates: implications for nitrogen and hydrogen storage in the Earth's mantle. Am. Mineral. 94, 283–292.

Watenphul, A., Wunder, B., Wirth, R., Heinrich, W., 2010. Ammonium-bearing clinopyroxene: a potential nitrogen reservoir in the Earth's mantle. Chem. Geol. 270, 240–248.

Article history:
Received 14 December 2017

Received in revised form 14 February 2018 Accepted 19 February 2018
Available online 28 February 2018
Editor: F. Moynier

## *6.3.9. Supplementary information*

*Supplementary Table 6.S3. Summary of high-pressure experiments*

| Run | P (GPa) | T (°C) | Duration (h) | Mineral | Spot No. | $^{15}$N in mineral (μmol/mol) | $^{15}$N in mineral (μg/g) | $^{15}$N (μg/g) in Fe metal | Mg# of mineral | Mg# of FeO | Fe/(Fe+Pt) (mol%) of Fe metal | Other phases |
|---|---|---|---|---|---|---|---|---|---|---|---|---|
| Z1405 | 16 | 1500 | 1 | olivine | 1 | 63.4 (22) | 44.9 (16) | n.m. | 90 | n.m. | 100 | wadsleyite, FeO |
| | | | | | 2 | 35.7 (17) | 25.2 (12) | | | | | Fe metal |
| | | | | | 3 | 51.3 (22) | 36.5 (15) | | | | | |
| | | | | | 4 | 25.5 (9) | 18.6 (6) | | | | | |
| | | | | | 5 | 25.7 (8) | 18.7 (6) | | | | | |
| | | | | | 6 | 62.8 (22) | 44.4 (16) | | | | | |
| | | | | | 7 | 57.9 (17) | 41.0 (12) | | | | | |
| | | | | | 13 | 80.2 (30) | 56.9 (21) | | | | | |
| | | | | | 14 | 69.8 (23) | 49.4 (16) | | | | | |
| | | | | | 16 | 52.3 (25) | 38.0 (18) | | | | | |
| | | | | | 17 | 45.2 (16) | 32.7 (11) | | | | | |
| S6348 | 14 | 1100 | 1 | wadsleyite | 1 | 11.3 (5) | 8.2 (4) | n.m. | 91 | 0 | 100 | FeO, Fe metal |
| | | | | | 2 | 14.1 (5) | 10.2 (4) | | | | | |
| | | | | | 3 | 14.5 (6) | 10.4 (4) | | | | | |
| S6361 | 14 | 1300 | 1 | wadsleyite | 1 | 21.7 (7) | 15.5 (5) | n.m. | 91 | 0 | 89 | FeO, Fe metal |
| | | | | | 2 | 16.7 (7) | 11.9 (5) | | | | | |
| | | | | | 3 | 18.6 (6) | 13.4 (4) | | | | | |
| | | | | | 4 | 16.5 (6) | 11.8 (5) | | | | | |
| | | | | | 5 | 19.5 (7) | 14.0 (5) | | | | | |
| | | | | | 6 | 21.4 (6) | 15.3 (5) | | | | | |
| S6350 | 14 | 1400 | 1 | wadsleyite | 1 | 65.0 (14) | 45.3 (10) | 1334 (1485) | 85 | 0 | 100 | olivine, ringwoodite |
| | | | | | 2 | 39.0 (9) | 26.8 (6) | | | | | Mg-rich silicate[*1], FeO |
| | | | | | 3 | 74.0 (15) | 52.0 (10) | | | | | Fe metal |
| | | | | | 4 | 44.0 (10) | 30.7 (7) | | | | | |
| | | | | | 5 | 49.9 (13) | 35.1 (9) | | | | | |
| S6332 | 15 | 1400 | 1 | wadsleyite | 1 | 129.1 (28) | 89.1 (19) | n.m. | 82 | 36 | 92 | Mg-rich silicate[*1] |
| | | | | | 2 | 66.4 (15) | 45.3 (10) | | | | | FeO, Fe metal |
| | | | | | 3 | 95.4 (19) | 64.8 (13) | | | | | |
| | | | | | 4 | 91.7 (18) | 63.8 (13) | | | | | |
| | | | | | 5 | 194.0 (37) | 133.7 (26) | | | | | |
| | | | | | 6 | 134.8 (33) | 95.3 (23) | | | | | |

| Run | P (GPa) | T (°C) | Duration (h) | Mineral | Spot No. | $^{15}$N in mineral (μmol/mol) | $^{15}$N in mineral (μg/g) | $^{15}$N (μg/g) in Fe metal | Mg# of mineral | Mg# of FeO | Fe/(Fe+Pt) (mol%) of Fe metal | Other phases |
|---|---|---|---|---|---|---|---|---|---|---|---|---|
| Z1383 | 16 | 1200 | 1 | wadsleyite | 1 | 15.2 (6) | 11.0 (5) | n.m. | 91 | n.m. | 100 | FeO, Fe metal |
| | | | | | 2 | 11.0 (5) | 8.0 (4) | | | | | |
| | | | | | 3 | 22.6 (8) | 16.3 (6) | | | | | |
| | | | | | 4 | 22.4 (8) | 16.0 (6) | | | | | |
| | | | | | 5 | 18.0 (8) | 12.9 (6) | | | | | |
| | | | | | 6 | 22.8 (9) | 16.3 (6) | | | | | |
| | | | | | 7 | 20.6 (7) | 15.0 (5) | | | | | |
| | | | | | 8 | 18.6 (7) | 13.2 (5) | | | | | |
| | | | | | 9 | 16.6 (7) | 11.7 (5) | | | | | |
| Z1405 | 16 | 1500 | 1 | wadsleyite | 8 | 299.2 (59) | 204.9 (40) | n.m. | 80 | n.m. | 100 | olivine, FeO, |
| | | | | | 9 | 291.3 (51) | 199.5 (35) | | | | | Fe metal |
| | | | | | 10 | 256.9 (51) | 176.0 (35) | | | | | |
| | | | | | 11 | 255.2 (52) | 174.8 (35) | | | | | |
| S6519 | 17 | 1400 | 1 | wadsleyite | 1 | 258.8 (63) | 179.9 (44) | 1272 (799) | 82 | 41 | 51 | FeO, Fe metal |
| | | | | | 2 | 326.9 (62) | 227.3 (43) | | | | | |
| | | | | | 3 | 278.5 (87) | 193.7 (61) | | | | | |
| | | | | | 4 | 318.9 (37) | 216.3 (25) | | | | | |
| | | | | | 5 | 148.3 (26) | 103.1 (18) | | | | | |
| | | | | | 6 | 102.6 (37) | 71.3 (26) | | | | | |
| | | | | | 7 | 53.1 (12) | 36.6 (9) | | | | | |
| | | | | | 9 | 304.1 (77) | 209.6 (53) | | | | | |
| S6521 | 19 | 1400 | 1 | wadsleyite | 1 | 17.3 (5) | 12.5 (4) | 1670 (510) | 87 | 8-59 | 88 | ringwoodite |
| | | | | | 2 | 82.2 (17) | 58.0 (12) | | | | | FeO, Fe metal |
| | | | | | 3 | 116.8 (28) | 82.8 (20) | | | | | |
| | | | | | 4 | 134.9 (20) | 94.4 (14) | | | | | |
| | | | | | 5 | 191.7 (35) | 134.1 (24) | | | | | |
| | | | | | 6 | 91.8 (43) | 64.6 (30) | | | | | |
| | | | | | 7 | 171.8 (31) | 120.2 (22) | | | | | |
| | | | | | 8 | 131.3 (20) | 92.0 (14) | | | | | |
| | | | | | 14 | 184.9 (30) | 129.4 (21) | | | | | |
| | | | | | 15 | 181.8 (30) | 127.3 (21) | | | | | |
| S6329 | 14 | 1100 | 1 | ringwoodite | 5 | 20.2 (10) | 13.1 (6) | n.m. | 68 | 23-35 | 100 | Mg-rich silicate[*1] |
| | | | | | 6 | 19.4 (9) | 12.7 (6) | | | | | FeO, Fe metal |
| S6521 | 19 | 1400 | 1 | ringwoodite | 9 | 73.5 (16) | 50.0 (11) | 1670 (510) | 73 | 8-59 | 88 | wadsleyite |
| | | | | | 10 | 74.9 (13) | 51.0 (9) | | | | | FeO, Fe metal |
| | | | | | 11 | 54.8 (14) | 36.1 (9) | | | | | |
| | | | | | 12 | 64.2 (19) | 41.1 (12) | | | | | |

| Run | P (GPa) | T (°C) | Duration (h) | Mineral | Spot No. | $^{15}$N in mineral (μmol/mol) | $^{15}$N in mineral (μg/g) | $^{15}$N (μg/g) in Fe metal | Mg# of mineral | Mg# of FeO | Fe/(Fe+Pt) (mol%) of Fe metal | Other phases |
|---|---|---|---|---|---|---|---|---|---|---|---|---|
| S6579 | 21 | 1200 | 1 | ringwoodite | 1 | 76.6 (23) | 51.4 (16) | 6635 (698) | 77 | 1-41 | 100 | FeO, Fe metal |
| | | | | | 2 | 87.7 (27) | 58.9 (18) | | | | | |
| | | | | | 3 | 46.5 (17) | 32.1 (12) | | | | | |
| | | | | | 5 | 71.8 (25) | 48.6 (17) | | | | | |
| | | | | | 6 | 77.3 (26) | 52.0 (17) | | | | | |
| | | | | | 7 | 69.6 (24) | 46.8 (16) | | | | | |
| | | | | | 8 | 82.8 (40) | 56.5 (27) | | | | | |
| H4326 | 21 | 1400 | 1 | ringwoodite | 2 | 132.8 (44) | 89.8 (30) | 3230 (779) | 76 | 11-43 | 66 | FeO, Fe metal |
| | | | | | 5 | 133.8 (20) | 90.2 (13) | | | | | |
| | | | | | 6 | 102.1 (22) | 68.9 (15) | | | | | |
| | | | | | 7 | 194.8 (37) | 131.0 (25) | | | | | |
| H4327 | 21 | 1600 | 1 | ringwoodite | 1 | 202.1 (33) | 134.0 (22) | 1046 (987) | 76 | 5-31 | 38 | FeO, Fe metal |
| | | | | | 2 | 133.8 (24) | 91.8 (17) | | | | | |
| | | | | | 3 | 165.4 (24) | 110.9 (16) | | | | | |
| | | | | | 4 | 130.4 (19) | 87.4 (13) | | | | | |
| | | | | | 5 | 190.9 (33) | 126.3 (22) | | | | | |
| | | | | | 6 | 121.7 (22) | 84.3 (15) | | | | | |
| | | | | | 8 | 141.3 (24) | 96.5 (16) | | | | | |
| S6571 | 23 | 1400 | 1 | ringwoodite | 1 | 80.1 (22) | 54.6 (15) | 10350 (651) | 78 | 21-33 | 73 | FeO, Fe metal |
| | | | | | 2 | 131.6 (25) | 89.7 (17) | | | | | |
| | | | | | 3 | 103.7 (21) | 73.0 (15) | | | | | |
| | | | | | 4 | 79.4 (21) | 53.2 (14) | | | | | |
| | | | | | 5 | 80.7 (26) | 53.9 (17) | | | | | |
| | | | | | 6 | 62.5 (17) | 43.1 (12) | | | | | |
| | | | | | 7 | 94.5 (23) | 62.8 (15) | | | | | |
| | | | | | 8 | 74.0 (20) | 49.7 (14) | | | | | |
| | | | | | 9 | 55.8 (20) | 38.4 (14) | | | | | |
| S6523 | 23 | 1800 | 1/3 | ringwoodite | 2 | 403.5 (54) | 283.0 (38) | 564 (557) | 79 | 40 | 32 | FeO, Fe metal |
| | | | | | 3 | 125.3 (33) | 87.4 (23) | | | | | |
| | | | | | 5 | 17.9 (9) | 12.0 (6) | | | | | |
| | | | | | 6 | 39.0 (13) | 26.1 (9) | | | | | |
| | | | | | 8 | 213.0 (38) | 143.6 (26) | | | | | |
| S6543 | 24 | 1600 | 1 | ringwoodite | 1 | 172.5 (38) | 118.4 (26) | n.m. | 82 | 21-36 | 42 | bridgmanite |
| | | | | | 3 | 76.6 (24) | 52.8 (17) | | | | | $MgSiO_3$ ilmenite |
| | | | | | 4 | 175.6 (35) | 120.2 (24) | | | | | Na-rich silicate |
| | | | | | 5 | 159.1 (31) | 108.7 (21) | | | | | FeO, Fe metal |
| | | | | | 7 | 48.3 (16) | 33.8 (11) | | | | | |
| | | | | | 8 | 158.5 (32) | 110.8 (22) | | | | | |

| Run | P (GPa) | T (°C) | Duration (h) | Mineral | Spot No. | $^{15}$N in mineral (μmol/mol) | $^{15}$N in mineral (μg/g) | $^{15}$N (μg/g) in Fe metal | Mg# of mineral | Mg# of FeO | Fe/(Fe+Pt) (mol%) of Fe metal | Other phases |
|---|---|---|---|---|---|---|---|---|---|---|---|---|
| S6543 | 24 | 1600 | 1 | bridgmanite | En-5 | 27.9 (8) | 20.6 (6) | n.m. | 97 | 21-36 | 42 | ringwoodite |
| | | | | | En-5n | 39.0 (11) | 28.9 (8) | | | | | $MgSiO_3$ ilmenite |
| | | | | | En-6 | 73.0 (24) | 53.9 (18) | | | | | Na-rich silicate |
| | | | | | En-7 | 7.8 (4) | 5.8 (3) | | | | | FeO, Fe metal |
| | | | | | En-8 | 10.0 (5) | 7.4 (4) | | | | | |
| | | | | | En-9 | 16.8 (6) | 12.5 (4) | | | | | |
| S6550 | 24 | 1600 | 1 | Ca-perovskite | En-2 | 20.7 (10) | 12.8 (6) | -[*2] | - | - | -[*2] | FeO[*2] |
| | | | | | En-4 | 17.3 (9) | 10.6 (5) | | | | | |
| | | | | | En-7 | 19.4 (8) | 12.0 (5) | | | | | |
| S6564 | 24 | 1600 | 1 | Ca-perovskite | En-1 | 110.4 (23) | 68.5 (15) | n.m. | - | - | 77 | FeO, Fe metal |
| | | | | | En-2 | 32.9 (11) | 20.5 (7) | | | | | |
| | | | | | En-10 | 73.4 (28) | 45.6 (18) | | | | | |

*n.m.: not measured*

*Mg # is the Mg number, i.e. the molar ratio of Mg/(Mg+Fe) in the main mineral phase or the FeO phase of the experiment. $^{15}$N concentrations are measured in μmol/mol, which is defined as the number of nitrogen atoms per one million atoms in the sample. In order to convert the μmol/mol $^{15}$N into ppm by weight of $^{15}$N, the numbers have to be multiplied with the mass of $^{15}$N and divided by the average mass of all atoms in the sample. Numbers in brackets give the errors (1σ) in the last digits of the measured nitrogen concentrations. n.m. = not measured.*

*[1]Unknown phase containing Mg, Fe, Si, and O; the Mg/Si molar ratio is close to 3.*

*[2]Fe metal phase was possibly lost during recovery of capsule.*

*Supplementary Table 6.S4. Major element composition (in wt.%) of the synthetic minerals, as derived from electron microprobe analyses*

| Run | Mineral | | $Na_2O$ | MgO | $Al_2O_3$ | $SiO_2$ | CaO | $TiO_2$ | FeO | Total | Mg# | Si/(Si+Ti) (mol%) |
|---|---|---|---|---|---|---|---|---|---|---|---|---|
| Z1405 | olivine | average | 0.12 | 49.58 | 0.05 | 41.11 | n.m. | n.m. | 10.14 | 101.00 | 89.71 | - |
| | | s.d. | 0.02 | 1.63 | 0.01 | 0.41 | | | 2.32 | 0.33 | 2.40 | - |
| S6348 | wadsleyite | average | 0.21 | 49.60 | 0.14 | 41.11 | n.m. | n.m. | 8.23 | 99.30 | 91.48 | - |
| | | s.d. | 0.02 | 0.65 | 0.02 | 0.44 | | | 0.21 | 1.04 | 0.22 | - |
| S6361 | wadsleyite | average | 0.22 | 49.60 | 0.14 | 41.34 | n.m. | n.m. | 9.42 | 100.72 | 90.37 | - |
| | | s.d. | 0.03 | 0.37 | 0.01 | 0.08 | | | 0.39 | 0.28 | 0.41 | - |
| S6350 | wadsleyite | average | 0.27 | 44.23 | 0.16 | 39.76 | n.m. | n.m. | 16.80 | 101.21 | 82.44 | - |
| | | s.d. | 0.04 | 2.28 | 0.02 | 0.56 | | | 3.08 | 0.36 | 3.44 | - |
| S6332 | wadsleyite | average | 0.26 | 44.47 | 0.17 | 39.12 | 0.01 | n.m. | 16.92 | 100.95 | 82.41 | - |
| | | s.d. | 0.04 | 3.54 | 0.02 | 1.84 | 0.01 | | 2.61 | 0.28 | 3.14 | - |
| Z1383 | wadsleyite | average | 0.22 | 49.42 | 0.15 | 41.47 | n.m. | n.m. | 9.82 | 101.09 | 89.97 | - |
| | | s.d. | 0.03 | 1.52 | 0.01 | 0.40 | | | 2.02 | 0.32 | 2.12 | - |
| Z1405 | wadsleyite | average | 0.46 | 41.98 | 0.20 | 39.56 | n.m. | n.m. | 18.92 | 101.12 | 79.82 | - |
| | | s.d. | 0.02 | 0.12 | 0.02 | 0.19 | | | 0.08 | 0.19 | 0.06 | - |
| S6519 | wadsleyite | average | 0.48 | 43.36 | 0.13 | 39.80 | 0.01 | n.m. | 18.47 | 102.24 | 80.70 | - |
| | | s.d. | 0.05 | 1.41 | 0.03 | 0.46 | 0.01 | | 2.03 | 0.40 | 2.21 | - |
| S6521 | wadsleyite | average | 0.44 | 47.95 | 0.19 | 40.75 | 0.00 | n.m. | 12.43 | 101.75 | 87.28 | - |
| | | s.d. | 0.07 | 2.05 | 0.03 | 0.61 | 0.00 | | 2.69 | 0.37 | 2.84 | - |
| S6329 | ringwoodite | average | 0.04 | 34.07 | 0.02 | 37.43 | n.m. | n.m. | 30.31 | 101.87 | 66.70 | - |
| | | s.d. | 0.02 | 1.02 | 0.01 | 0.33 | | | 1.30 | 0.61 | 1.57 | - |
| S6521 | ringwoodtite | average | 0.12 | 37.07 | 0.06 | 38.54 | 0.01 | n.m. | 27.14 | 102.94 | 70.77 | - |
| | | s.d. | 0.04 | 4.79 | 0.01 | 1.20 | 0.01 | | 6.49 | 0.52 | 7.61 | - |

| Run | Mineral | | $Na_2O$ | MgO | $Al_2O_3$ | $SiO_2$ | CaO | $TiO_2$ | FeO | Total | Mg# | Si/(Si+Ti) (mol%) |
|---|---|---|---|---|---|---|---|---|---|---|---|---|
| S6579 | ringwoodite | average | 0.13 | 41.44 | 0.05 | 39.48 | 0.01 | n.m. | 21.73 | 102.84 | 77.26 | - |
| | | s.d. | 0.06 | 1.50 | 0.02 | 0.48 | 0.01 | | 1.94 | 0.34 | 2.18 | - |
| H4326 | ringwoodite | average | 0.20 | 40.82 | 0.05 | 39.35 | 0.00 | n.m. | 22.16 | 102.58 | 76.64 | - |
| | | s.d. | 0.08 | 1.67 | 0.01 | 0.37 | 0.01 | | 2.17 | 0.33 | 2.46 | - |
| H4327 | ringwoodite | average | 0.19 | 41.29 | 0.06 | 39.73 | 0.00 | n.m. | 21.25 | 102.53 | 77.52 | - |
| | | s.d. | 0.04 | 3.23 | 0.02 | 0.61 | 0.01 | | 4.16 | 0.42 | 4.76 | - |
| S6523 | ringwoodite | average | 0.27 | 43.66 | 0.01 | 39.76 | 0.00 | n.m. | 18.85 | 102.55 | 80.50 | - |
| | | s.d. | 0.04 | 4.30 | 0.01 | 0.84 | 0.01 | | 5.43 | 0.50 | 6.06 | - |
| S6571 | ringwoodite | average | 0.22 | 41.09 | 0.07 | 39.84 | 0.01 | n.m. | 21.05 | 102.28 | 77.61 | - |
| | | s.d. | 0.02 | 2.95 | 0.02 | 0.57 | 0.01 | | 3.82 | 0.48 | 4.35 | - |
| S6543 | ringwoodite | average | 0.29 | 44.44 | 0.00 | 40.30 | 0.01 | n.m. | 17.33 | 102.37 | 82.04 | - |
| | | s.d. | 0.05 | 1.58 | 0.00 | 0.46 | 0.01 | | 2.20 | 0.54 | 2.38 | - |
| S6543 | bridgmanite | average | 0.56 | 38.40 | 0.00 | 60.81 | 0.01 | n.m. | 2.59 | 102.37 | 96.36 | - |
| | | s.d. | 0.13 | 0.69 | 0.00 | 0.87 | 0.01 | | 1.04 | 0.63 | 1.46 | - |
| S6550 | Ca-perovskite | average | 0.01 | 0.17 | 0.00 | 36.06 | 44.73 | 15.37 | 1.48 | 97.82 | - | 75.71 |
| | | s.d. | 0.01 | 0.06 | 0.00 | 0.74 | 0.28 | 0.66 | 0.08 | 0.45 | - | 1.16 |
| S6564 | Ca-perovskite | average | 0.03 | 0.05 | 0.00 | 37.66 | 44.62 | 13.60 | 0.91 | 96.86 | - | 78.62 |
| | | s.d. | 0.02 | 0.01 | 0.00 | 1.48 | 1.41 | 0.83 | 0.69 | 2.72 | - | 1.21 |

*Mg# is the Mg number, i.e. the molar ratio of Mg/(Mg+Fe); s.d. represents the one standard deviation. n.m. = not measured*

*Supplementary Table 6.S5. Calculation of nitrogen concentration in minerals from SIMS data.*

| Run No. Meas. No. | Phase | P (GPa) | T (C°) | time (h) | $^{28}Si$ (cps, meas.) | $^{14}N$ (cps, meas.) | $^{15}N$ (cps, meas.) | $^{15}N/^{14}N$ (cps/cps, bud.) | $^{15}N^{+}/^{28}Si^{++}$ corrected (cps/cps, meas.) | s.d. (%) | $^{15}N^{+}/^{28}Si^{++}$ corrected (cps/cps, std. avr.) | $^{15}N$ std. (μmol/mol) | Si std. (atom%) | Si sample (atom%) | $^{15}N$ (μmol/mol) | s.d. (μmol/mol) | $^{15}N$ (μg/g) | s.d. (μg/g) |
|---|---|---|---|---|---|---|---|---|---|---|---|---|---|---|---|---|---|---|
| Z1405_1 | Olivine | 16 | 1500 | 1 | 2.25E+05 | 3.10E+02 | 1.25E+01 | 3.40E-03 | 5.08E-05 | 3.5 | 4.06E-05 | 51.0 | 14.3 | 14.2 | 63.4 | 2.2 | 44.9 | 1.6 |
| Z1405_2 | Olivine | 16 | 1500 | 1 | 2.26E+05 | 2.11E+01 | 6.52E+00 | 3.40E-03 | 2.85E-05 | 4.9 | 4.06E-05 | 51.0 | 14.3 | 14.2 | 35.7 | 1.7 | 25.2 | 1.2 |
| Z1405_3 | Olivine | 16 | 1500 | 1 | 2.14E+05 | 2.29E+01 | 8.83E+00 | 3.40E-03 | 4.09E-05 | 4.2 | 4.06E-05 | 51.0 | 14.3 | 14.3 | 51.3 | 2.2 | 36.5 | 1.5 |
| Z1405_4 | Olivine | 16 | 1500 | 1 | 2.26E+05 | 1.98E+01 | 4.65E+00 | 3.40E-03 | 2.03E-05 | 3.4 | 4.06E-05 | 51.0 | 14.3 | 14.3 | 25.5 | 0.9 | 18.6 | 0.6 |
| Z1405_5 | Olivine | 16 | 1500 | 1 | 2.18E+05 | 1.97E+01 | 4.54E+00 | 3.40E-03 | 2.05E-05 | 3.1 | 4.06E-05 | 51.0 | 14.3 | 14.3 | 25.7 | 0.8 | 18.7 | 0.6 |
| Z1405_6 | Olivine | 16 | 1500 | 1 | 2.31E+05 | 1.79E+01 | 1.16E+01 | 3.40E-03 | 5.00E-05 | 3.6 | 4.06E-05 | 51.0 | 14.3 | 14.3 | 62.8 | 2.2 | 44.4 | 1.6 |
| Z1405_7 | Olivine | 16 | 1500 | 1 | 2.30E+05 | 1.50E+01 | 1.07E+01 | 3.40E-03 | 4.63E-05 | 2.9 | 4.06E-05 | 51.0 | 14.3 | 14.2 | 57.9 | 1.7 | 41.0 | 1.2 |
| Z1405_8 | Wadsleyite | 16 | 1500 | 1 | 2.08E+05 | 1.61E+01 | 4.98E+01 | 3.40E-03 | 2.39E-04 | 2.0 | 4.06E-05 | 51.0 | 14.3 | 14.2 | 299.2 | 5.9 | 204.9 | 4.0 |
| Z1405_9 | Wadsleyite | 16 | 1500 | 1 | 2.08E+05 | 1.46E+01 | 4.86E+01 | 3.40E-03 | 2.33E-04 | 1.7 | 4.06E-05 | 51.0 | 14.3 | 14.2 | 291.3 | 5.1 | 199.5 | 3.5 |
| Z1405_10 | Wadsleyite | 16 | 1500 | 1 | 2.21E+05 | 1.12E+01 | 4.58E+01 | 3.40E-03 | 2.07E-04 | 2.0 | 4.12E-05 | 51.0 | 14.3 | 14.3 | 256.9 | 5.1 | 176.0 | 3.5 |
| Z1405_11 | Wadsleyite | 16 | 1500 | 1 | 2.09E+05 | 7.38E+00 | 4.31E+01 | 3.40E-03 | 2.06E-04 | 2.0 | 4.12E-05 | 51.0 | 14.3 | 14.3 | 255.2 | 5.2 | 174.8 | 3.5 |
| Z1405_13 | Olivine | 16 | 1500 | 1 | 2.31E+05 | 8.27E+00 | 1.51E+01 | 3.40E-03 | 6.51E-05 | 3.7 | 4.12E-05 | 51.0 | 14.3 | 14.2 | 80.2 | 3.0 | 56.9 | 2.1 |
| Z1405_14 | Olivine | 16 | 1500 | 1 | 2.32E+05 | 8.51E+00 | 1.31E+01 | 3.40E-03 | 5.65E-05 | 3.3 | 4.12E-05 | 51.0 | 14.3 | 14.2 | 69.7 | 2.3 | 49.4 | 1.6 |
| Z1405_16 | Olivine | 16 | 1500 | 1 | 2.21E+05 | 1.29E+03 | 1.37E+01 | 3.40E-03 | 4.22E-05 | 4.7 | 4.12E-05 | 51.0 | 14.3 | 14.3 | 52.3 | 2.5 | 38.0 | 1.8 |
| Z1405_17 | Olivine | 16 | 1500 | 1 | 2.23E+05 | 8.56E+00 | 8.12E+00 | 3.40E-03 | 3.63E-05 | 3.5 | 4.12E-05 | 51.0 | 14.3 | 14.4 | 45.2 | 1.6 | 32.7 | 1.1 |
| Z1383@1 | Wadsleyite | 16 | 1200 | 1 | 1.87E+05 | 6.04E+00 | 2.64E+00 | 3.43E-03 | 1.40E-05 | 4.1 | 4.71E-05 | 51.0 | 14.3 | 14.4 | 15.2 | 0.6 | 11.0 | 0.5 |
| Z1383@2 | Wadsleyite | 16 | 1200 | 1 | 1.98E+05 | 5.18E+00 | 2.02E+00 | 3.43E-03 | 1.01E-05 | 4.7 | 4.71E-05 | 51.0 | 14.3 | 14.4 | 11.0 | 0.5 | 8.0 | 0.4 |
| Z1383@3 | Wadsleyite | 16 | 1200 | 1 | 2.03E+05 | 6.57E+00 | 4.22E+00 | 3.43E-03 | 2.07E-05 | 3.4 | 4.71E-05 | 51.0 | 14.3 | 14.4 | 22.6 | 0.8 | 16.3 | 0.6 |
| Z1383@4 | Wadsleyite | 16 | 1200 | 1 | 2.06E+05 | 6.78E+00 | 4.27E+00 | 3.43E-03 | 2.06E-05 | 3.7 | 4.71E-05 | 51.0 | 14.3 | 14.3 | 22.4 | 0.8 | 16.0 | 0.6 |
| Z1383@5 | Wadsleyite | 16 | 1200 | 1 | 2.04E+05 | 7.31E+00 | 3.41E+00 | 3.43E-03 | 1.66E-05 | 4.3 | 4.71E-05 | 51.0 | 14.3 | 14.3 | 18.0 | 0.8 | 12.9 | 0.6 |
| Z1383@6 | Wadsleyite | 16 | 1200 | 1 | 2.01E+05 | 6.24E+00 | 4.25E+00 | 3.43E-03 | 2.10E-05 | 3.8 | 4.71E-05 | 51.0 | 14.3 | 14.3 | 22.8 | 0.9 | 16.3 | 0.6 |
| Z1383@7 | Wadsleyite | 16 | 1200 | 1 | 1.98E+05 | 5.54E+00 | 3.75E+00 | 3.43E-03 | 1.88E-05 | 3.4 | 4.71E-05 | 51.0 | 14.3 | 14.4 | 20.6 | 0.7 | 15.0 | 0.5 |
| Z1383@8 | Wadsleyite | 16 | 1200 | 1 | 2.03E+05 | 5.69E+00 | 3.50E+00 | 3.43E-03 | 1.72E-05 | 3.5 | 4.71E-05 | 51.0 | 14.3 | 14.3 | 18.6 | 0.7 | 13.2 | 0.5 |
| Z1383@9 | Wadsleyite | 16 | 1200 | 1 | 1.94E+05 | 5.54E+00 | 3.01E+00 | 3.43E-03 | 1.54E-05 | 4.5 | 4.71E-05 | 51.0 | 14.3 | 14.3 | 16.6 | 0.7 | 11.7 | 0.5 |
| H4326@2 | Ringwoodite | 21 | 1400 | 1 | 1.82E+05 | 3.97E+01 | 2.25E+01 | 3.43E-03 | 1.23E-04 | 3.3 | 4.73E-05 | 51.0 | 14.3 | 14.3 | 132.8 | 4.4 | 89.8 | 3.0 |
| H4326@5 | Ringwoodite | 21 | 1400 | 1 | 1.75E+05 | 3.87E+01 | 2.19E+01 | 3.43E-03 | 1.25E-04 | 1.5 | 4.73E-05 | 51.0 | 14.3 | 14.2 | 133.8 | 2.0 | 90.2 | 1.3 |
| H4326@6 | Ringwoodite | 21 | 1400 | 1 | 1.82E+05 | 3.69E+01 | 1.74E+01 | 3.43E-03 | 9.51E-05 | 2.2 | 4.73E-05 | 51.0 | 14.3 | 14.2 | 102.1 | 2.2 | 68.9 | 1.5 |
| H4326@7 | Ringwoodite | 21 | 1400 | 1 | 1.64E+05 | 3.41E+01 | 2.99E+01 | 3.43E-03 | 1.82E-04 | 1.9 | 4.73E-05 | 51.0 | 14.3 | 14.2 | 194.8 | 3.7 | 131.0 | 2.5 |
| H4327@1 | Ringwoodite | 21 | 1600 | 1 | 1.35E+05 | 1.61E+01 | 2.53E+01 | 3.43E-03 | 1.87E-04 | 1.6 | 4.73E-05 | 51.0 | 14.3 | 14.3 | 202.1 | 3.3 | 134.0 | 2.2 |
| H4327@2 | Ringwoodite | 21 | 1600 | 1 | 1.74E+05 | 2.57E+01 | 2.18E+01 | 3.43E-03 | 1.25E-04 | 1.8 | 4.73E-05 | 51.0 | 14.3 | 14.3 | 133.8 | 2.4 | 91.8 | 1.7 |
| H4327@3 | Ringwoodite | 21 | 1600 | 1 | 1.36E+05 | 1.37E+01 | 2.09E+01 | 3.43E-03 | 1.54E-04 | 1.4 | 4.73E-05 | 51.0 | 14.3 | 14.2 | 165.4 | 2.4 | 110.9 | 1.6 |
| H4327@4 | Ringwoodite | 21 | 1600 | 1 | 1.71E+05 | 2.31E+01 | 2.09E+01 | 3.43E-03 | 1.21E-04 | 1.5 | 4.73E-05 | 51.0 | 14.3 | 14.2 | 130.4 | 1.9 | 87.4 | 1.3 |
| H4327@5 | Ringwoodite | 21 | 1600 | 1 | 1.12E+05 | 1.41E+01 | 1.98E+01 | 3.43E-03 | 1.76E-04 | 1.7 | 4.73E-05 | 51.0 | 14.3 | 14.4 | 190.9 | 3.3 | 126.3 | 2.2 |

| Run No. Meas. No. | Phase | P (GPa) | T (C°) | time (h) | $^{28}Si$ (cps, meas.) | $^{14}N$ (cps, meas.) | $^{15}N$ (cps, meas.) | $^{15}N/^{14}N$ (cps/cps, bud.) | $^{15}N^{+}/^{28}Si^{++}$ corrected (cps/cps, meas.) | s.d. (%) | $^{15}N^{+}/^{28}Si^{++}$ corrected (cps/cps, std. avr.) | $^{15}N$ std. (μmol/mol) | Si std. (atom%) | Si sample (atom%) | $^{15}N$ (μmol/mol) | s.d. (μmol/mol) | $^{15}N$ (μg/g) | s.d. (μg/g) |
|---|---|---|---|---|---|---|---|---|---|---|---|---|---|---|---|---|---|---|
| H4327@6 | Ringwoodite | 21 | 1600 | 1 | 1.58E+05 | 1.19E+01 | 1.78E+01 | 3.43E-03 | 1.13E-04 | 1.8 | 4.73E-05 | 51.0 | 14.3 | 14.3 | 121.7 | 2.2 | 84.3 | 1.5 |
| H4327@8 | Ringwoodite | 21 | 1600 | 1 | 1.40E+05 | 1.19E+01 | 1.83E+01 | 3.43E-03 | 1.31E-04 | 1.7 | 4.73E-05 | 51.0 | 14.3 | 14.3 | 141.3 | 2.4 | 96.5 | 1.6 |
| S6571@1 | Ringwoodite | 23 | 1400 | 1 | 1.02E+05 | 9.73E+00 | 7.60E+00 | 3.43E-03 | 7.40E-05 | 2.7 | 4.73E-05 | 51.0 | 14.3 | 14.4 | 80.1 | 2.2 | 54.6 | 1.5 |
| S6571@2 | Ringwoodite | 23 | 1400 | 1 | 1.10E+05 | 9.45E+00 | 1.34E+01 | 3.43E-03 | 1.22E-04 | 1.9 | 4.73E-05 | 51.0 | 14.3 | 14.4 | 131.6 | 2.5 | 89.7 | 1.7 |
| S6571@3 | Ringwoodite | 23 | 1400 | 1 | 1.15E+05 | 9.05E+00 | 1.11E+01 | 3.43E-03 | 9.62E-05 | 2.0 | 4.73E-05 | 51.0 | 14.3 | 14.3 | 103.7 | 2.1 | 73.0 | 1.5 |
| S6571@4 | Ringwoodite | 23 | 1400 | 1 | 8.02E+04 | 8.80E+00 | 5.92E+00 | 3.43E-03 | 7.34E-05 | 2.7 | 4.73E-05 | 51.0 | 14.3 | 14.3 | 79.4 | 2.1 | 53.2 | 1.4 |
| S6571@5 | Ringwoodite | 23 | 1400 | 1 | 7.51E+04 | 7.41E+00 | 5.63E+00 | 3.43E-03 | 7.46E-05 | 3.2 | 4.73E-05 | 51.0 | 14.3 | 14.3 | 80.7 | 2.6 | 53.9 | 1.7 |
| S6571@6 | Ringwoodite | 23 | 1400 | 1 | 9.89E+04 | 8.22E+00 | 5.73E+00 | 3.43E-03 | 5.76E-05 | 2.8 | 4.73E-05 | 51.0 | 14.3 | 14.4 | 62.5 | 1.7 | 43.1 | 1.2 |
| S6571@7 | Ringwoodite | 23 | 1400 | 1 | 8.72E+04 | 8.76E+00 | 7.66E+00 | 3.43E-03 | 8.75E-05 | 2.4 | 4.73E-05 | 51.0 | 14.3 | 14.3 | 94.5 | 2.3 | 62.8 | 1.5 |
| S6571@8 | Ringwoodite | 23 | 1400 | 1 | 8.60E+04 | 9.42E+00 | 5.92E+00 | 3.43E-03 | 6.84E-05 | 2.7 | 4.73E-05 | 51.0 | 14.3 | 14.3 | 74.0 | 2.0 | 49.7 | 1.4 |
| S6571@9 | Ringwoodite | 23 | 1400 | 1 | 9.62E+04 | 8.00E+00 | 4.98E+00 | 3.43E-03 | 5.15E-05 | 3.5 | 4.73E-05 | 51.0 | 14.3 | 14.4 | 55.8 | 2.0 | 38.4 | 1.4 |
| S6579@1 | Ringwoodite | 21 | 1200 | 1 | 8.04E+04 | 1.16E+01 | 5.75E+00 | 3.43E-03 | 7.11E-05 | 3.0 | 4.73E-05 | 51.0 | 14.3 | 14.3 | 76.6 | 2.3 | 51.4 | 1.6 |
| S6579@2 | Ringwoodite | 21 | 1200 | 1 | 6.22E+04 | 8.32E+00 | 5.21E+00 | 3.43E-03 | 8.32E-05 | 3.1 | 4.73E-05 | 51.0 | 14.3 | 14.0 | 87.7 | 2.7 | 58.9 | 1.8 |
| S6579@3 | Ringwoodite | 21 | 1200 | 1 | 7.57E+04 | 8.77E+00 | 3.32E+00 | 3.43E-03 | 4.35E-05 | 3.6 | 4.73E-05 | 51.0 | 14.3 | 14.2 | 46.5 | 1.7 | 32.1 | 1.2 |
| S6579@5 | Ringwoodite | 21 | 1200 | 1 | 5.50E+04 | 7.70E+00 | 3.67E+00 | 3.43E-03 | 6.62E-05 | 3.5 | 4.73E-05 | 51.0 | 14.3 | 14.4 | 71.8 | 2.5 | 48.6 | 1.7 |
| S6579@6 | Ringwoodite | 21 | 1200 | 1 | 5.41E+04 | 8.60E+00 | 3.93E+00 | 3.43E-03 | 7.20E-05 | 3.3 | 4.73E-05 | 51.0 | 14.3 | 14.3 | 77.3 | 2.6 | 52.0 | 1.7 |
| S6579@7 | Ringwoodite | 21 | 1200 | 1 | 5.75E+04 | 7.27E+00 | 3.75E+00 | 3.43E-03 | 6.47E-05 | 3.4 | 4.73E-05 | 51.0 | 14.3 | 14.3 | 69.6 | 2.4 | 46.8 | 1.6 |
| S6579@8 | Ringwoodite | 21 | 1200 | 1 | 6.47E+04 | 8.47E+00 | 5.04E+00 | 3.43E-03 | 7.73E-05 | 4.9 | 4.73E-05 | 51.0 | 14.3 | 14.2 | 82.8 | 4.0 | 56.5 | 2.7 |
| S6350@1 | Wadsleyite | 14 | 1400 | 1 | 2.41E+05 | 2.99E+01 | 1.46E+01 | 3.43E-03 | 6.00E-05 | 2.1 | 4.66E-05 | 51.0 | 14.3 | 14.1 | 65.0 | 1.4 | 45.3 | 1.0 |
| S6350@2 | Wadsleyite | 14 | 1400 | 1 | 2.54E+05 | 2.99E+01 | 9.27E+00 | 3.43E-03 | 3.60E-05 | 2.4 | 4.66E-05 | 51.0 | 14.3 | 14.1 | 39.0 | 0.9 | 26.8 | 0.6 |
| S6350@3 | Wadsleyite | 14 | 1400 | 1 | 2.68E+05 | 2.76E+01 | 1.83E+01 | 3.43E-03 | 6.79E-05 | 2.0 | 4.66E-05 | 51.0 | 14.3 | 14.2 | 74.0 | 1.5 | 52.0 | 1.0 |
| S6350@4 | Wadsleyite | 14 | 1400 | 1 | 2.60E+05 | 2.46E+01 | 1.06E+01 | 3.43E-03 | 4.04E-05 | 2.2 | 4.66E-05 | 51.0 | 14.3 | 14.2 | 44.0 | 1.0 | 30.7 | 0.7 |
| S6350@5 | Wadsleyite | 14 | 1400 | 1 | 2.62E+05 | 2.41E+01 | 1.20E+01 | 3.43E-03 | 4.57E-05 | 2.5 | 4.66E-05 | 51.0 | 14.3 | 14.2 | 49.9 | 1.3 | 35.1 | 0.9 |
| S6348@1 | Wadsleyite | 14 | 1100 | 1 | 2.05E+05 | 1.52E+01 | 2.18E+00 | 3.43E-03 | 1.04E-05 | 4.5 | 4.66E-05 | 51.0 | 14.3 | 14.3 | 11.3 | 0.5 | 8.2 | 0.4 |
| S6348@2 | Wadsleyite | 14 | 1100 | 1 | 2.21E+05 | 1.51E+01 | 2.90E+00 | 3.43E-03 | 1.29E-05 | 3.9 | 4.66E-05 | 51.0 | 14.3 | 14.3 | 14.1 | 0.5 | 10.2 | 0.4 |
| S6348@3 | Wadsleyite | 14 | 1100 | 1 | 2.22E+05 | 1.47E+01 | 2.99E+00 | 3.43E-03 | 1.32E-05 | 3.8 | 4.66E-05 | 51.0 | 14.3 | 14.3 | 14.5 | 0.6 | 10.4 | 0.4 |
| S6521@1 | Wadsleyite | 19 | 1400 | 1 | 2.70E+05 | 2.54E+01 | 4.30E+00 | 3.43E-03 | 1.56E-05 | 3.2 | 4.61E-05 | 51.0 | 14.3 | 14.3 | 17.3 | 0.5 | 12.5 | 0.4 |
| S6521@02 | Wadsleyite | 19 | 1400 | 1 | 2.78E+05 | 2.54E+01 | 2.09E+01 | 3.43E-03 | 7.51E-05 | 2.0 | 4.61E-05 | 51.0 | 14.3 | 14.1 | 82.2 | 1.7 | 58.0 | 1.2 |
| S6521@03 | Wadsleyite | 19 | 1400 | 1 | 2.69E+05 | 2.12E+02 | 2.94E+01 | 3.43E-03 | 1.07E-04 | 2.4 | 4.61E-05 | 51.0 | 14.3 | 14.2 | 116.8 | 2.8 | 82.8 | 2.0 |
| S6521@04 | Wadsleyite | 19 | 1400 | 1 | 2.75E+05 | 2.17E+01 | 3.38E+01 | 3.43E-03 | 1.23E-04 | 1.5 | 4.61E-05 | 51.0 | 14.3 | 14.2 | 134.9 | 2.0 | 94.4 | 1.4 |
| S6521@05 | Wadsleyite | 19 | 1400 | 1 | 2.66E+05 | 1.71E+01 | 4.65E+01 | 3.43E-03 | 1.75E-04 | 1.8 | 4.61E-05 | 51.0 | 14.3 | 14.2 | 191.7 | 3.5 | 134.1 | 2.4 |
| S6521@06 | Wadsleyite | 19 | 1400 | 1 | 2.76E+05 | 3.08E+02 | 2.40E+01 | 3.43E-03 | 8.30E-05 | 4.6 | 4.61E-05 | 51.0 | 14.3 | 14.3 | 91.8 | 4.3 | 64.6 | 3.0 |
| S6521@07 | Wadsleyite | 19 | 1400 | 1 | 2.73E+05 | 1.60E+01 | 4.29E+01 | 3.43E-03 | 1.57E-04 | 1.8 | 4.61E-05 | 51.0 | 14.3 | 14.2 | 171.8 | 3.1 | 120.2 | 2.2 |
| S6521@08 | Wadsleyite | 19 | 1400 | 1 | 2.69E+05 | 1.40E+01 | 3.25E+01 | 3.43E-03 | 1.21E-04 | 1.6 | 4.61E-05 | 51.0 | 14.3 | 14.0 | 131.3 | 2.0 | 92.0 | 1.4 |

| Run No. Meas. No. | Phase | P (GPa) | T (C°) | time (h) | $^{28}Si$ (cps, meas.) | $^{14}N$ (cps, meas.) | $^{15}N$ (cps, meas.) | $^{15}N/^{14}N$ (cps/cps, bud.) | $^{15}N^{+}/^{28}Si^{++}$ corrected (cps/cps, meas.) | s.d. (%) | $^{15}N^{+}/^{28}Si^{++}$ corrected (cps/cps, std. avr.) | $^{15}N$ std. (μmol/mol) | Si std. (atom%) | Si sample (atom%) | $^{15}N$ (μmol/mol) | s.d. (μmol/mol) | $^{15}N$ (μg/g) | s.d. (μg/g) |
|---|---|---|---|---|---|---|---|---|---|---|---|---|---|---|---|---|---|---|
| S6521@09 | Ringwoodite | 19 | 1400 | 1 | 2.20E+05 | 1.32E+01 | 1.47E+01 | 3.43E-03 | 6.66E-05 | 2.2 | 4.61E-05 | 51.0 | 14.3 | 14.3 | 73.5 | 1.6 | 50.0 | 1.1 |
| S6521@10 | Ringwoodite | 19 | 1400 | 1 | 2.21E+05 | 1.21E+01 | 1.50E+01 | 3.43E-03 | 6.79E-05 | 1.7 | 4.61E-05 | 51.0 | 14.3 | 14.3 | 74.9 | 1.3 | 51.0 | 0.9 |
| S6521@11 | Ringwoodite | 19 | 1400 | 1 | 1.49E+05 | 1.19E+02 | 7.87E+00 | 3.43E-03 | 5.01E-05 | 2.5 | 4.61E-05 | 51.0 | 14.3 | 14.1 | 54.8 | 1.4 | 36.1 | 0.9 |
| S6521@12 | Ringwoodite | 19 | 1400 | 1 | 1.19E+05 | 1.00E+01 | 7.05E+00 | 3.43E-03 | 5.88E-05 | 3.0 | 4.61E-05 | 51.0 | 14.3 | 14.1 | 64.2 | 1.9 | 41.1 | 1.2 |
| S6521@14 | Wadsleyite | 19 | 1400 | 1 | 2.52E+05 | 1.17E+01 | 4.23E+01 | 3.43E-03 | 1.68E-04 | 1.6 | 4.61E-05 | 51.0 | 14.3 | 14.2 | 184.9 | 3.0 | 129.4 | 2.1 |
| S6521@15 | Wadsleyite | 19 | 1400 | 1 | 2.43E+05 | 1.13E+01 | 4.00E+01 | 3.43E-03 | 1.65E-04 | 1.7 | 4.61E-05 | 51.0 | 14.3 | 14.3 | 181.8 | 3.0 | 127.3 | 2.1 |
| S6519@1 | Wadsleyite | 17 | 1400 | 1 | 1.89E+05 | 1.80E+01 | 4.47E+01 | 3.43E-03 | 2.36E-04 | 2.4 | 4.61E-05 | 51.0 | 14.3 | 14.2 | 258.8 | 6.3 | 179.9 | 4.4 |
| S6519@2 | Wadsleyite | 17 | 1400 | 1 | 2.51E+05 | 1.15E+01 | 7.49E+01 | 3.43E-03 | 2.98E-04 | 1.9 | 4.61E-05 | 51.0 | 14.3 | 14.2 | 326.9 | 6.2 | 227.3 | 4.3 |
| S6519@3 | Wadsleyite | 17 | 1400 | 1 | 2.46E+05 | 5.40E+01 | 6.27E+01 | 3.43E-03 | 2.54E-04 | 3.1 | 4.61E-05 | 51.0 | 14.3 | 14.2 | 278.5 | 8.7 | 193.7 | 6.1 |
| S6519@4 | Wadsleyite | 17 | 1400 | 1 | 2.10E+05 | 1.75E+01 | 6.11E+01 | 3.43E-03 | 2.91E-04 | 1.2 | 4.61E-05 | 51.0 | 14.3 | 14.2 | 318.9 | 3.7 | 216.3 | 2.5 |
| S6519@5 | Wadsleyite | 17 | 1400 | 1 | 2.22E+05 | 1.97E+01 | 3.01E+01 | 3.43E-03 | 1.35E-04 | 1.8 | 4.61E-05 | 51.0 | 14.3 | 14.2 | 148.3 | 2.6 | 103.1 | 1.8 |
| S6519@6 | Wadsleyite | 17 | 1400 | 1 | 2.10E+05 | 2.52E+01 | 1.97E+01 | 3.43E-03 | 9.36E-05 | 3.6 | 4.61E-05 | 51.0 | 14.3 | 14.2 | 102.6 | 3.7 | 71.3 | 2.6 |
| S6519@7 | Wadsleyite | 17 | 1400 | 1 | 2.09E+05 | 8.26E+00 | 1.01E+01 | 3.43E-03 | 4.83E-05 | 2.3 | 4.61E-05 | 51.0 | 14.3 | 14.2 | 53.1 | 1.2 | 36.6 | 0.9 |
| S6519@9 | Wadsleyite | 17 | 1400 | 1 | 1.71E+05 | 2.72E+01 | 4.72E+01 | 3.43E-03 | 2.76E-04 | 2.5 | 4.61E-05 | 51.0 | 14.3 | 14.2 | 304.1 | 7.7 | 209.6 | 5.3 |
| S6523@02 | Ringwoodite | 23 | 1800 | 1/3 | 2.87E+05 | 2.04E+01 | 1.06E+02 | 3.43E-03 | 3.67E-04 | 1.3 | 4.61E-05 | 51.0 | 14.3 | 14.2 | 403.5 | 5.4 | 283.0 | 3.8 |
| S6523@03 | Ringwoodite | 23 | 1800 | 1/3 | 1.29E+05 | 8.36E+00 | 1.49E+01 | 3.43E-03 | 1.16E-04 | 2.6 | 4.61E-05 | 51.0 | 14.3 | 14.0 | 125.3 | 3.3 | 87.4 | 2.3 |
| S6523@05 | Ringwoodite | 23 | 1800 | 1/3 | 1.18E+05 | 7.03E+00 | 1.95E+00 | 3.43E-03 | 1.63E-05 | 4.7 | 4.61E-05 | 51.0 | 14.3 | 14.2 | 17.9 | 0.9 | 12.0 | 0.6 |
| S6523@06 | Ringwoodite | 23 | 1800 | 1/3 | 1.73E+05 | 1.52E+01 | 6.20E+00 | 3.43E-03 | 3.55E-05 | 3.3 | 4.61E-05 | 51.0 | 14.3 | 14.2 | 39.0 | 1.3 | 26.1 | 0.9 |
| S6523@08 | Ringwoodite | 23 | 1800 | 1/3 | 1.22E+05 | 7.36E+01 | 2.39E+01 | 3.43E-03 | 1.94E-04 | 1.8 | 4.61E-05 | 51.0 | 14.3 | 14.2 | 213.0 | 3.8 | 143.6 | 2.6 |
| S6361@1 | Wadsleyite | 14 | 1300 | 1 | 2.45E+05 | 1.47E+01 | 4.78E+00 | 3.43E-03 | 1.93E-05 | 3.0 | 4.56E-05 | 51.0 | 14.3 | 14.3 | 21.7 | 0.7 | 15.5 | 0.5 |
| S6361@2 | Wadsleyite | 14 | 1300 | 1 | 2.57E+05 | 1.64E+01 | 3.88E+00 | 3.43E-03 | 1.49E-05 | 4.1 | 4.56E-05 | 51.0 | 14.3 | 14.3 | 16.7 | 0.7 | 11.9 | 0.5 |
| S6361@3 | Wadsleyite | 14 | 1300 | 1 | 2.42E+05 | 1.32E+01 | 4.06E+00 | 3.43E-03 | 1.66E-05 | 3.3 | 4.56E-05 | 51.0 | 14.3 | 14.4 | 18.6 | 0.6 | 13.4 | 0.4 |
| S6361@4 | Wadsleyite | 14 | 1300 | 1 | 2.52E+05 | 1.61E+01 | 3.75E+00 | 3.43E-03 | 1.47E-05 | 3.9 | 4.56E-05 | 51.0 | 14.3 | 14.3 | 16.5 | 0.6 | 11.8 | 0.5 |
| S6361@5 | Wadsleyite | 14 | 1300 | 1 | 2.20E+05 | 1.10E+01 | 3.86E+00 | 3.43E-03 | 1.73E-05 | 3.5 | 4.56E-05 | 51.0 | 14.3 | 14.4 | 19.5 | 0.7 | 14.0 | 0.5 |
| S6361@6 | Wadsleyite | 14 | 1300 | 1 | 2.48E+05 | 1.44E+01 | 4.80E+00 | 3.43E-03 | 1.91E-05 | 3.0 | 4.56E-05 | 51.0 | 14.3 | 14.3 | 21.4 | 0.6 | 15.3 | 0.5 |
| S6543@1 | Ringwoodite | 24 | 1600 | 1 | 1.25E+05 | 1.58E+02 | 2.28E+01 | 3.43E-03 | 1.78E-04 | 2.2 | 5.29E-05 | 51.0 | 14.3 | 14.4 | 172.5 | 3.8 | 118.4 | 2.6 |
| S6543@3 | Ringwoodite | 24 | 1600 | 1 | 1.24E+05 | 7.20E+00 | 9.88E+00 | 3.43E-03 | 7.97E-05 | 3.1 | 5.29E-05 | 51.0 | 14.3 | 14.2 | 76.6 | 2.4 | 52.8 | 1.7 |
| S6543@4 | Ringwoodite | 24 | 1600 | 1 | 1.16E+05 | 1.20E+01 | 2.14E+01 | 3.43E-03 | 1.83E-04 | 2.0 | 5.29E-05 | 51.0 | 14.3 | 14.2 | 175.6 | 3.5 | 120.2 | 2.4 |
| S6543@5 | Ringwoodite | 24 | 1600 | 1 | 1.15E+05 | 1.04E+01 | 1.92E+01 | 3.43E-03 | 1.66E-04 | 1.9 | 5.29E-05 | 51.0 | 14.3 | 14.2 | 159.1 | 3.1 | 108.7 | 2.1 |
| S6543@7 | Ringwoodite | 24 | 1600 | 1 | 1.43E+05 | 9.51E+00 | 7.23E+00 | 3.43E-03 | 5.05E-05 | 3.2 | 5.29E-05 | 51.0 | 14.3 | 14.2 | 48.3 | 1.6 | 33.8 | 1.1 |
| S6543@8 | Ringwoodite | 24 | 1600 | 1 | 1.30E+05 | 9.25E+00 | 2.13E+01 | 3.43E-03 | 1.64E-04 | 2.0 | 5.29E-05 | 51.0 | 14.3 | 14.3 | 158.5 | 3.2 | 110.8 | 2.2 |
| S6329@5 | Ringwoodite | 14 | 1100 | 1 | 9.14E+04 | 1.27E+01 | 1.98E+00 | 3.43E-03 | 2.12E-05 | 4.7 | 5.29E-05 | 51.0 | 14.3 | 14.2 | 20.2 | 1.0 | 13.1 | 0.6 |
| S6329@6 | Ringwoodite | 14 | 1100 | 1 | 9.58E+04 | 1.10E+01 | 1.97E+00 | 3.43E-03 | 2.02E-05 | 4.7 | 5.29E-05 | 51.0 | 14.3 | 14.2 | 19.4 | 0.9 | 12.7 | 0.6 |
| S6332@1 | Wadsleyite | 15 | 1400 | 1 | 1.29E+05 | 2.04E+01 | 1.74E+01 | 3.43E-03 | 1.35E-04 | 2.2 | 5.29E-05 | 51.0 | 14.3 | 14.2 | 129.1 | 2.8 | 89.1 | 1.9 |

| Run No. Meas. No. | Phase | P (GPa) | T (C°) | time (h) | $^{28}Si$ (cps, meas.) | $^{14}N$ (cps, meas.) | $^{15}N$ (cps, meas.) | $^{15}N/^{14}N$ (cps/cps, bud.) | $^{15}N^{+}/^{28}Si^{++}$ corrected (cps/cps, meas.) | s.d. (%) | $^{15}N^{+}/^{28}Si^{++}$ corrected (cps/cps, std. avr.) | $^{15}N$ std. (μmol/mol) | Si std. (atom%) | Si sample (atom%) | $^{15}N$ (μmol/mol) | s.d. (μmol/mol) | $^{15}N$ (μg/g) | s.d. (μg/g) |
|---|---|---|---|---|---|---|---|---|---|---|---|---|---|---|---|---|---|---|
| S6332@2 | Wadsleyite | 15 | 1400 | 1 | 1.21E+05 | 1.86E+01 | 8.45E+00 | 3.43E-03 | 6.91E-05 | 2.3 | 5.29E-05 | 51.0 | 14.3 | 14.2 | 66.4 | 1.5 | 45.3 | 1.0 |
| S6332@3 | Wadsleyite | 15 | 1400 | 1 | 1.12E+05 | 1.53E+01 | 1.12E+01 | 3.43E-03 | 9.95E-05 | 2.0 | 5.29E-05 | 51.0 | 14.3 | 14.2 | 95.4 | 1.9 | 64.8 | 1.3 |
| S6332@4 | Wadsleyite | 15 | 1400 | 1 | 1.30E+05 | 1.75E+01 | 1.25E+01 | 3.43E-03 | 9.55E-05 | 2.0 | 5.29E-05 | 51.0 | 14.3 | 14.2 | 91.7 | 1.8 | 63.8 | 1.3 |
| S6332@5 | Wadsleyite | 15 | 1400 | 1 | 1.25E+05 | 1.72E+01 | 2.55E+01 | 3.43E-03 | 2.03E-04 | 1.9 | 5.29E-05 | 51.0 | 14.3 | 14.1 | 194.0 | 3.7 | 133.7 | 2.6 |
| S6332@6 | Wadsleyite | 15 | 1400 | 1 | 1.34E+05 | 1.53E+01 | 1.88E+01 | 3.43E-03 | 1.40E-04 | 2.5 | 5.29E-05 | 51.0 | 14.3 | 14.3 | 134.8 | 3.3 | 95.3 | 2.3 |
| En S6543@5 | Bridgmanite | 24 | 1600 | 1 | 2.28E+05 | 2.78E+01 | 6.60E+00 | 3.43E-03 | 2.85E-05 | 3.0 | 5.12E-04 | 501.3 | 20.0 | 20.0 | 27.9 | 0.8 | 20.6 | 0.6 |
| En S6543@new5 | Bridgmanite | 24 | 1600 | 1 | 2.47E+05 | 1.08E+01 | 9.86E+00 | 3.43E-03 | 3.99E-05 | 2.9 | 5.12E-04 | 501.3 | 20.0 | 20.0 | 39.0 | 1.1 | 28.9 | 0.8 |
| En S6543@6 | Bridgmanite | 24 | 1600 | 1 | 2.34E+05 | 1.65E+01 | 1.75E+01 | 3.43E-03 | 7.45E-05 | 3.3 | 5.12E-04 | 501.3 | 20.0 | 20.0 | 73.0 | 2.4 | 53.9 | 1.8 |
| En S6543@7 | Bridgmanite | 24 | 1600 | 1 | 2.31E+05 | 1.05E+01 | 1.88E+00 | 3.43E-03 | 7.98E-06 | 4.8 | 5.12E-04 | 501.3 | 20.0 | 20.0 | 7.8 | 0.4 | 5.8 | 0.3 |
| En S6543i@8 | Bridgmanite | 24 | 1600 | 1 | 2.31E+05 | 8.18E+00 | 2.39E+00 | 3.43E-03 | 1.03E-05 | 4.8 | 5.12E-04 | 501.3 | 20.0 | 20.0 | 10.0 | 0.5 | 7.4 | 0.4 |
| En S6543@9 | Bridgmanite | 24 | 1600 | 1 | 2.28E+05 | 9.29E+00 | 3.96E+00 | 3.43E-03 | 1.72E-05 | 3.4 | 5.12E-04 | 501.3 | 20.0 | 20.0 | 16.8 | 0.6 | 12.5 | 0.4 |
| En S6543@7 | Ca-pv | 24 | 1600 | 1 | 5.97E+04 | 5.00E+01 | 1.84E+00 | 3.43E-03 | 2.80E-05 | 4.8 | 5.12E-04 | 501.3 | 20.0 | 15.1 | 20.7 | 1.0 | 12.8 | 0.6 |
| En S6543@4 | Ca-pv | 24 | 1600 | 1 | 5.91E+04 | 1.38E+02 | 1.87E+00 | 3.43E-03 | 2.37E-05 | 5.0 | 5.12E-04 | 501.3 | 20.0 | 14.9 | 17.3 | 0.9 | 10.6 | 0.5 |
| En S6543@2 | Ca-pv | 24 | 1600 | 1 | 6.06E+04 | 2.56E+02 | 2.46E+00 | 3.43E-03 | 2.61E-05 | 4.2 | 5.12E-04 | 501.3 | 20.0 | 15.2 | 19.4 | 0.8 | 12.0 | 0.5 |
| S6564 En@1 | Ca-pv | 24 | 1600 | 1 | 6.14E+04 | 2.34E+02 | 9.71E+00 | 3.43E-03 | 1.45E-04 | 2.1 | 5.12E-04 | 501.3 | 20.0 | 15.5 | 110.4 | 2.3 | 68.5 | 1.5 |
| S6564 En@2 | Ca-pv | 24 | 1600 | 1 | 5.97E+04 | 5.45E+02 | 4.43E+00 | 3.43E-03 | 4.29E-05 | 3.2 | 5.12E-04 | 501.3 | 20.0 | 15.7 | 32.9 | 1.1 | 20.5 | 0.7 |
| S6564 En@10 | Ca-pv | 24 | 1600 | 1 | 5.13E+04 | 7.38E+02 | 7.46E+00 | 3.43E-03 | 9.60E-05 | 3.9 | 5.12E-04 | 501.3 | 20.0 | 15.6 | 73.4 | 2.8 | 45.6 | 1.8 |

*Abbreviations: meas. = measurement, measured. cps = count per seconds. bud. = buddingtonite. s.d. = one standard deviation. std. = standard. avr. = average. Ca-pv = Ca-silicate perovsilite.*

# Acknowledgments

First of all I would like to express my primary gratitude to my supervisor, Professor Hans Keppler, who gave me a lot of support to complete my PhD thesis. He always gave me clear view on my PhD studies when I talk with him. He also taught me how to deal with a problem, to organize series of experiments/analysis and how important it is to make everything efficiently.

I am very thankful to Professor Dan Frost, who cared me and my study as my vice-supervisor. He also gave me an opportunity to participate in the Volatile Workshop in Tohoku University and to carry out my study as a part of the IRTG project.
Upon the experiments and measurements, I am grateful for help by Svyatoslav Shcheka, who kindly spared his time to teach and assist high-pressure experiments and microprobe analyses. It was great fun and relief for me to talk with him about fishing and fish in the Sea of Japan.
I also thank scientists and technicians in BGI, Catherine McCammon, Tiziana Boffa-Ballaran, Detlef Klaußе, Ulrike Tenz, Dorothea Wiesner, Anke Potzel, Sven Lindhardt, Kurt Klasinski, Heinz Fischer and Stefan Übelhack, who kindly helped experiments and analyses. Sample preparations by Hubert Schulze, Njul Raphael and Alexander Rother were always in great quality and produced good result on sample analyses.
I appreciate support in work at BGI by Stefan Keyssner, Florian Heidelbach, Lydia Kison-Herzig, Petra Buchrrt, Nicole Fischer, Romina Scharfenberg and Janina Potzel.
I was glad to share the office with Stella Chariton, Nicki Siersch, Greta Rustioni, Ja Chang, Taku Yutani, Julia Immoor, Daohan Zhang, Thomas Chust, Valerio Cerantola, Ana Cernok, Lanlan Shi and Natalia Solopova. I thank all my colleagues in BGI, including Lin Wang and Kirsten Schulze who were working in the next room.

I am really thankful to the Japanese scientists in BGI, Professor Tomoo Katsura, Nobuyoshi Miyajima, Takaaki Kawazoe, Takayuki Ishii, Ryosuke Shinmyo and Taku Yutani, who kindly cared both for my private life and for science in Bayreuth.

Finally I would like to express my gratitude to scientists outside BGI, Michael Wiedenbeck in GFZ Potsdam, Professor Tomoki Nakamura, Daisuke Nakashima, Masakuni Yamanobe in Tohoku University for their contribution to my PhD study.

**(Eidesstattliche) Versicherungen und Erklärungen**

(§9 Satz 2 Nr. 3 PromO BayNAT)
*Hiermit versichere ich eidesstattlich, dass ich die Arbeit selbständig verfasst und keine anderen als die von mir angegebenen Quellen und Hilfsmittel benutzt habe (vgl. Art. 64 Abs. 1 Satz 6 BayHSchG).*

(§9 Satz 2 Nr. 3 PromO BayNAT)
*Hiermit erkläre ich, dass ich die Dissertation nicht bereits zur Erlangung eines akademischen Grades eingereicht habe und dass ich nicht bereits diese oder eine gleichartige Doktorprüfung endgültig nicht bestanden habe.*

(§9 Satz 2 Nr. 4 PromO BayNAT)
*Hiermit erkläre ich, dass ich Hilfe von gewerblichen Promotionsberatern bzw. -vermittlern oder ähnlichen Dienstleistern weder bisher in Anspruch genommen habe noch künftig in Anspruch nehmen werde.*

(§9 Satz 2 Nr. 7 PromO BayNAT)
*Hiermit erkläre ich mein Einverständnis, dass die elektronische Fassung meiner Dissertation unter Wahrung meiner Urheberrechte und des Datenschutzes einer gesonderten Überprüfung unterzogen werden kann.*

(§9 Satz 2 Nr. 8 PromO BayNAT)
*Hiermit erkläre ich mein Einverständnis, dass bei Verdacht wissenschaftlichen Fehlverhaltens Ermittlungen durch universitätsinterne Organe der wissenschaftlichen Selbstkontrolle stattfinden können.*

_____

Ort, Datum, Unterschrift